Two-Phase Flow in Microchannels with Application to PEM Fuel Cells

by

Te-Chun Wu
B.Sc., Chung Yuan Christian University, 1993
M.Sc., National Cheng Kung University, 1995
Ph.D., National Cheng Kung University, 2000

A Dissertation Submitted in Partial Fulfillment of the
Requirements for the Degree of

DOCTOR OF PHILOSOPHY

in the Department of Mechanical Engineering

Two-Phase Flow in Microchannels with Application to PEM Fuel Cells

by

Te-Chun Wu
B.Sc., Chung Yuan Christian University, 1993
M.Sc., National Cheng Kung University, 1995
Ph.D., National Cheng Kung University, 2000

Supervisory Committee

Dr. Ned Djilali, Supervisor
(Department of Mechanical Engineering, University of Victoria)

Dr. Rustom Bhiladvala, Departmental Member
(Department of Mechanical Engineering, University of Victoria)

Dr. Alexandra Branzan Albu, Outside Member
(Department of Electrical and Computer Engineering, University of Victoria)

Supervisory Committee

Dr. Ned Djilali, Supervisor
(Department of Mechanical Engineering, University of Victoria)

Dr. Rustom Bhiladvala, Departmental Member
(Department of Mechanical Engineering, University of Victoria)

Dr. Alexandra Branzan Albu, Outside Member
(Department of Electrical and Computer Engineering, University of Victoria)

ABSTRACT

The performance of PEM fuel cells (PEMFC) relies on the proper control and management of the liquid water that forms as a result of the electrochemical process, especially at high current densities. The liquid water transport and removal process in the gas flow channel is highly dynamic and many of its fundamental features are not well understood. This thesis presents an experimental and theoretical investigation of the emergence of water droplets from a single pore into a microchannel. The experiments are performed in a 250 μm × 250 μm air channel geometry with a single 50 μm pore that replicates a PEMFC cathode gas channel. A droplet manipulation platform is constructed using a microfluidics soft lithographic process to allow observation of the dynamic nature of the water droplets. Flow conditions that correspond to typical operating conditions in a PEMFC are selected. A test matrix of experiments comprised of different water injection velocities and air velocities in the gas microchannel is studied. Emergence, detachment and subsequent dynamic evolution of water droplets are analyzed, both qualitatively and quantitatively. Quantitative image analysis tools are implemented and applied to the time-resolved images to document the time evolution of the shape and location of the droplets,

characteristic frequencies, dynamic contact angles, flow regime and stability maps. Three different flow regimes are identified, slug, droplet, and film flow. The effects of the air flow rate and droplet size on the critical detachment conditions are also investigated.

Numerical simulations using Volume-of-Fluid method are presented to investigate the water dynamics in the droplet flow. The focus of the modeling is on methods that account for the dynamic nature of the contact line evolution. Results of different approaches of dynamic contact angle formulations derived empirically and by using the theoretically based Hoffmann function are compared with the static contact angle models used to date. The importance of the dynamic formulation as well as the necessity for high numerical resolution is highlighted. The Hoffmann function implementation is found to better capture the salient droplet motion dynamics in terms of advancing and receding contact angle and periodicity of the emergence process.

To explore the possibility of using the pressure drop signal as a diagnostic tool in operational fuel cells that are not optically accessible, a flow diagnostic tool was developed based on pressure drop measurements in a custom designed two-phase flow fixture with commercial flow channel designs. Water accumulation at the channel outlet was found to be the primary cause of a low-frequency periodic oscillation of pressure drop signal. It is shown that the flow regimes can be characterized using the power spectrum density of the normalized pressure drop signal. This is used to construct a flow map correlating pressure drop signals to the flow regimes, and opens the possibility for practical flow diagnostics in operating fuel cells.

Table of Contents

List of Tables

List of Figures

Acknowledgments

I would express my thankfulness to my supervisor, Dr. Ned Djilali, who supported me through these years and offered invaluable guidance in many aspects not only as an advisor but also as a friend.

My special thanks go to Dr. Jay Sui who spent countless time with me in the Energy Systems and Transport Phenomena (ESTP) lab and his office for the supporting discussions and friendly encouragement during my research work.

I would like to thank the group members in ESTP and Institute for Integrated Energy Systems (IESVic). I am fortunate to work with such many talented students, researchers and staff.

I would also like to thank my family in Taiwan, including my parents and parents-in-law, for their everlasting encouragement and inspiration through my adventures.

Last but not least, this milestone wouldn't complete without the deepest love from my wife - Anita Fang, my children - Vicky and Brian. Your overflowing support and understanding builds up every tiny step in our life to fulfill a huge dream for the future.

Dedication

To Anita, Vicky and Brian

It's simply not possible to continue without your inspiration.

Chapter 1

1 Introduction

1.1. Background and Motivation

PEM fuel cells (PEMFCs) have been the focus of intense research in the last decade because of their potential to produce clean electricity efficiently for vehicles and stationary applications as well as their central role in the hydrogen economy. Successful deployment of PEMFCs into automobile and residential applications will depend on successfully addressing a number of issues, including water management, more specifically, the liquid water transport and removal process. Water is generated from the electrochemical reaction between hydrogen and oxygen and is the major by-product of the reaction in PEMFCs. It is usually found at the cathode side, although it is also present in the anode. It is important to remove liquid water from the PEMFC to prevent flooding of the electrodes and the blocking of pores in the gas diffusion layer (GDL). Conversely, a sufficient amount of water/hydration is necessary to maintain high protonic conductivity in the membrane.

However, the presence of some liquid water is unavoidable in most PEMFCs, particularly at higher current densities, where gas-liquid two-phase flow occurs in the porous electrodes and flow channels. The occurrence of two-phase flow leads to different flow regimes and flow patterns, and is accompanied by a substantial pressure drop. The two-phase flow regimes increase the complexity of water management. Liquid water must be transported out of the catalyst layer, through the GDL, and into the flow

channels, before being removed by the gas flow. Although practical experience and empirically based design tools have allowed progress in water management techniques, the processes are not well understood. Not much detailed information has been obtained on the flow dynamics and associated flow regimes due to the difficulty of measuring and directly observing water removal processes in a PEMFC.

The mechanisms of liquid water transport in the flow channel of a PEMFC include the initial emergence of droplets in the GDL, their subsequent growth and detachment from the GDL, and finally the interaction with the walls. These mechanisms lead to complex two-phase flow throughout the channel. Figure 1.1 presents a schematic of a water droplet emerging from the GDL and entering the cathode gas flow channel.

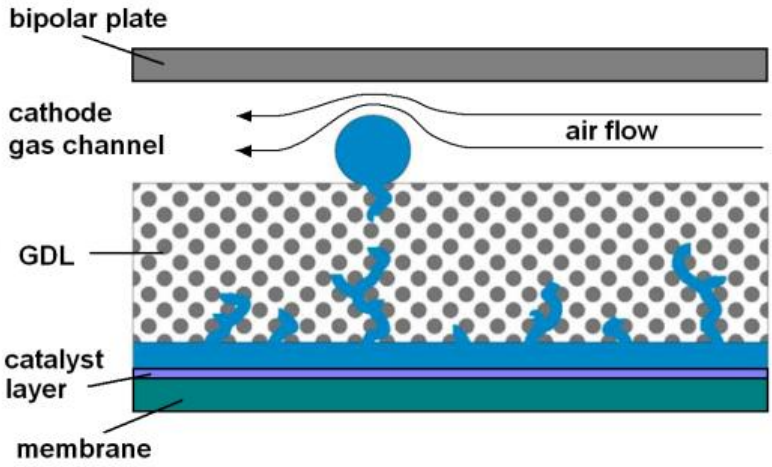

Figure 1.1. An emerged water droplet from the GDL entering the cathode gas flow channel (reproduced from [89] with permission of Journal of Power Sources).

In classical two-phase flows in channels [1] it is often the case that both the liquid and gas are introduced together into a flow channel or the gas phase is produced on the channel wall due to boiling in a flow dominated by the liquid phase. Two-phase flows in PEMFC flow channels are fundamentally different in several respects:

1. The gas phase is dominant (i.e. low saturation or high void fraction).
2. Water emerges from a porous layer (GDL) that interacts with the gas flow in the channel.

3. The channel walls have mixed surface wetting properties; three of the walls comprised of the bipolar plate are typically hydrophilic, while the fourth wall corresponding to the GDL is porous, rough and hydrophobic.
4. The length, time and flow scales and corresponding characteristic non-dimensional numbers (Reynolds number, Capillary and Webber number) differ significantly from those of "classical" two-phase flows.

These characteristics and the larger role of surface forces make the complexity of two-phase flow in PEMFC flow channels challenging to analyze and predict. A further complication is introduced by the variety of mechanisms by which water is transported and produced in the fuel cell, including electro-osmotic drag, back diffusion, water production from electrochemical reactions, etc. [2]. Finally, significant temperature gradients can be present in a fuel cell and strongly impact the relative humidity and saturation pressure, which affect the rate of phase change.

The size of the flow channel plays an important role in two-phase flow. It can radically affect the flow regime and, hence, the fuel cell performance. A typical range for hydraulic diameters of flow channels in PEMFCs is from 200 μm to 3 mm [3]. The flow is laminar but unsteady; the liquid phase is dominated by surface forces instead of volume forces and is strongly affected by the hydrophilic or hydrophobic properties of the surface. The design of the cathode flow channel is the most important consideration for water management [3]. Hence, improved understanding and prediction of two-phase flow in the cathode flow microchannel of PEMFCs could pave the way for new or better concepts in channel design as well as water management.

1.2. Scope and Organization of the Thesis

The objective of the work described in this thesis is to quantify the liquid water droplet dynamics as well as the two-phase flow phenomena relevant to PEM fuels cells. The approach combines experimental observations with numerical modelling. Chapter 2 presents a literature review synthesizing experimental and theoretical work, and open research question. In Chapter 3 we present flow visualization experiments in laboratory flow channels relevant to fuel cells to observe and quantify the dynamics of

liquid water droplets. Chapter 4 presents computational modelling of the two-phase flow with a focus on the physical representation of the dynamic process. The correlation between pressure signals and the two-phase flow regimes is investigated experimentally in Chapter 5 as a preliminary step to diagnostics for operating fuel cells. Chapter 6 summarizes the contributions and outlines recommendations for future research.

Chapter 2

2 Literature Review

In this section, reviews of salient features of two-phase flow in PEMFC microchannels are addressed. These include the dynamic behavior of liquid water, the different flow regimes, the pressure drop along the channel, the effects of channel geometry and surface properties of the boundaries.

2.1. Dynamic Behavior of Liquid Water

Water management affects performance and durability of PEM fuel cells (PEMFCs), and remains a pacing item in the development of commercial stacks. In spite of a number of experimental and theoretical studies, the underlying liquid water transport, including water droplet generation, growth, detachment and removal processes, are not well understood. This stems from the modelling challenges associated with the complex dynamics of the two-phase flow, and from the optically inaccessible and electrochemically active nature of a fuel cell that make *in-situ* measurements difficult. The experimental challenges and a review of the techniques used to date to visualize liquid water transport are discussed by Bazylak [4]. One of the most widely used approaches is optical visualization/photography in custom-designed transparent PEMFCs. This approach is exemplified by the work of Tüber et al. [5] who, based on their observations, concluded that hydrophilic diffusion layers resulted in increased current densities and better fuel cell performance as a result of more uniform membrane hydration. Yang et al. [6] visualized water droplet emergence from the GDL surface and its subsequent behavior in the gas channel. They found that droplets appear only at

certain preferential locations, and can grow to a size comparable to the channel dimensions. A variety of phenomena in the gas channel were reported, including the intermittent emergence of droplets, film formation and channel clogging. Chen et al. [7] proposed a simplified force balance model based on droplet geometry approximations for predicting the onset of water droplet instability on GDL surfaces, and supported the model through their experimental observations. They found that droplet removal can be enhanced by increasing the flow channel length or mean gas flow velocity, by decreasing the channel height or contact angle hysteresis (the difference between the advancing and receding contact angles), or by making the GDL more hydrophobic. Two different modes of liquid water removal were identified by Zhang et al. [8], and based on a further analysis using the force balance model, they proposed a relationship between the droplet detachment diameter and air velocity. Independently of Chen et al. [7], Kumbur et al. [9] conducted a similar theoretical and experimental study of the influence of controllable engineering parameters, including surface PTFE coverage, channel geometry, droplet chord dimensions, and operational air flow rate. The proposed water droplet instability criterion was formulated in terms of the Reynolds number and droplet aspect ratio. Theodorakakos et al. [10] constructed a platform consisting of a high aspect ratio channel (2.7 mm × 7.0 mm) for visualizing the behavior of a single droplet placed on the surface of different GDLs. They obtained side-view droplet detachment images and measured the dynamic contact angles for input into their in-house volume-of-fluid (VOF) computer simulations, and were able to correlate the critical droplet diameter at detachment with the air velocity. The channel dimensions in these studies [9,10] were significantly larger than PEMFC gas flow channels, which have hydraulic diameters ranging from 200 μm to 3 mm [3], and though valuable, the insights from these studies are expected to have limited relevance to PEMFCs because of the important impact of reduced dimensions on the two-phase flow. Whereas previous experimental studies [5–10] investigated water droplets or films initially resting on a GDL, the actual water transport process in a PEMFC channel also involves the initial emergence of droplets into the GDL, their subsequent growth and detachment from the GDL and, finally, their interaction with the walls leading to a complex two-phase flow regime throughout the channel. The resulting flow regimes may vary between surface tension dominated slug flow and inertia

dominated annular flow (i.e. film flow as shown in Figure 2.1) depending on the load [3]. The annular or dispersed droplet flow regime is desirable in fuel cell operation since this provides a path for reactant flow in the presence of water. However, due to the operational load of fuel cell stacks, the flow regime is at times likely to shift to slug flow because at low power the shear force in the cathode channels is usually insufficient to overcome the surface tension forces that hold water within the flow field channels and GDLs.

2.2. Flow Regime

While microchannel two-phase flows have been the focus of many experimental and theoretical studies targeted at PEMFCs (see review by Anderson et al. [11]), such flows are also of relevance in applications ranging from heat sinks for electronic devices to microreactors and microfluidic devices. Most of the work in these latter applications is concerned with acqueous-acqueous systems, but a few studies have recently investigated gas-liquid systems using flow visualization and particle image velocimetry. Günther et al [12] investigated different gas–liquid rectangular microfluidic channels and networks pertinent to chemical reactions and mapped bubbly, slug and annular flow patterns as a function of the gas and liquid superficial velocities. A flow pattern map based on dimensional analysis and visualization was also presented by Waelchli et al. [13] for conditions related to microreactors. Based on a critical review of available observations, it was noted that basing the similarity analysis on cross-sectional channel shape rather than hydraulic diameters is key for reliable prediction of flow regime based on experimental flow maps. This is consistent with the recent study of Kim et al. [14] who identified three fundamentally different two-phase flow regimes (capillary bubbly, segmented, annular) together with two transitory ones. They reported that the transition boundaries depend on the geometry of the test microchannels and of the injection port. They also noted differences in pressure drop for the capillary bubbly and segmented flow regimes when using different microchannel materials. Note that these microfluidic studies were all performed using hydrophilic surfaces as opposed to the hydrophobic surfaces of the flow channel in PEM fuel cells. The flow regimes identified in these studies, such as bubbly (or capillary bubbly), slug (or segmented), annular (or film) have

different characteristics and are not all relevant to fuel cell channels. For instance, the bubbly flow is unlikely occurs in PEM fuel cells since it is only present under very high liquid velocity conditions (i.e. liquid phase dominated) with minimal gas flow.

As in the case of microfluidic applications, two-phase flow regimes relevant to PEMFC cathodes can be broadly classified as slug, droplet and film flows, but the detailed characteristics and transition boundaries differ significantly due to the properties of the GDL, and particularly hydrophobicity and roughness. Each of the three regimes can occur solely in a channel, or two or more might occur simultaneously at different locations of the flow channel [11]. Hussaini and Wang [15] presented an in-situ study of cathode flooding using a transparent PEMFC. Gas relative humidities of 26%, 42% and 66%, current densities of 0.2, 0.5 and 0.8 A cm^{-2} and flow stoichiometries ranging from 2 to 4 were used to represent typical operating conditions for automotive applications. Based on observed flow patterns and the superficial phase velocities, a flow map as show in Figure 2.1 was developed and utilized to determine operating conditions that prevent channel flooding.

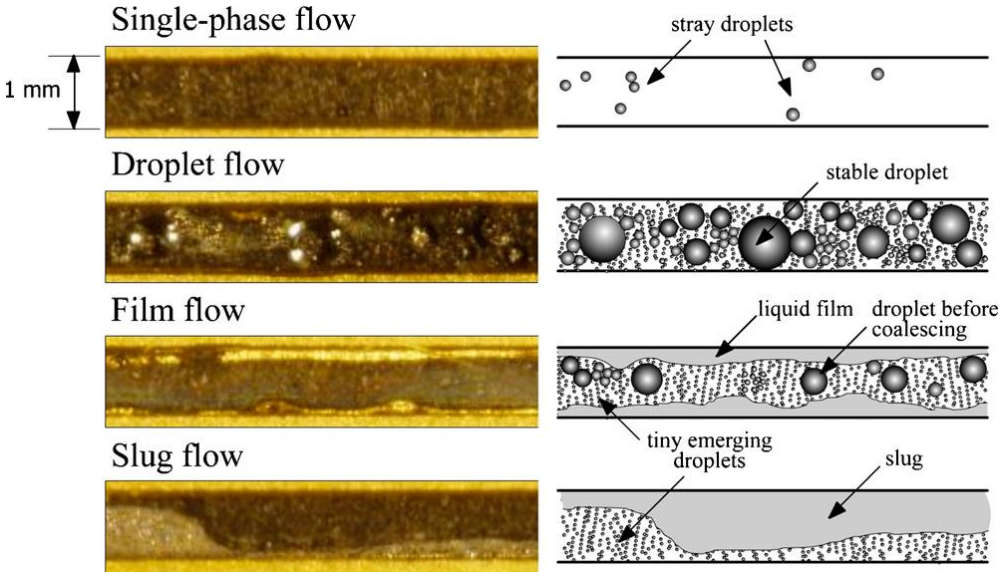

Figure 2.1. Typical flow patterns in gas channel of PEMFC (reproduced from [15] with permission of Journal of Power Sources).

However, there are inconsistencies in the observed flow patterns from various studies. Direct ex-situ visualization of droplet evolution using laboratory models of fuel cell microchannels has allowed some detailed analysis not possible in-situ. Hidrovo et al.

[16] investigated water slug detachment in two-phase hydrophobic microchannel flows. Due to the aspect ratio and geometry of the microchannel, water was observed to form pancake-like slugs rather than a spherical cap droplet. More recently, Lu et al. [17][18] presented flow visualization and pressure drop measurements over a broad range of flow regimes, flow parameters, channel surface wettability, geometry and orientation. Colosqui et al. [19] used an experimental set-up conceptually similar to the present one but with larger channel cross-sections in which gravity and surface tension forces are of the same order. Results showed that flow channel geometry and interfacial forces are the dominant factors in determining the size of slugs and the required pressure drop for their removal, those residual water droplets can alter the wetting properties and act as nucleating agents that impact the dynamics of slug formation and detachment. The interaction between the air and water flows that occur at the gas–liquid interface of a droplet was examined by Minor et al. [20]. Using micro-digital-particle-image-velocimetry (micro-DPIV) and examining seeded droplets first placed on a GDL, they analyzed the relationship between air velocity in the channel, secondary rotational flow inside a droplet, droplet deformation and contact angle hysteresis.

2.3. Pressure Drop

In operating PEM fuel cells, a low pressure difference across the flow field is generally desirable to lower auxiliary power demand. On the other hand, a larger pressure drop is desirable and often necessary to remove water from the flow field channels. Differential pressure signals have been widely adopted as one of the quickest approaches for identifying two-phase flow regimes. The pressure drop signal correlates closely with the two-phase flow regime especially when slug flow occurs. The presence of liquid water in fuel cell channels hinders the gas flow, thus creating a higher gas pressure gradient compared with single phase flow. In fuel cell operating conditions, a greater pressure drop will increase the risk of instability, cost, and lower performance. It is evident that the flow maldistribution suffers primarily from the increase in the pressure drop due to uneven water distribution from channel to channel and thus is detrimental to fuel cell performance and durability. Yousfi-Steiner at al. [21] reviewed the voltage degradation issues associated with the water flow factors and characterization of water management.

In PEMFCs, significant pressure drop is caused by the frictions of the cell, especially the gas flow field inside the porous structure of the electrode and the GDL. The other major contribution to pressure drop in PEMFCs is due to the hydrodynamics of two-phase flow inside the channel. The pressure drop usually can be measured between inlet and outlet channels of the gas manifold as well as at the anode or cathode. Quantifying the contribution due to channel flooding is a key factor and is still a challenge. In the case of two-phase flow in the channels, Rodatz et al. [22] showed that the existence of liquid water can reduce the cross sectional area available for gas diffusion which in turn reduces the gas permeability, leading to an increase of the pressure drop according to Darcy's law. Therefore, the pressure drop in the flow fields varies as a function of the flooding level, and can indicate the presence of liquid water. It is evident that due to the higher amount of liquid water production and accumulation in the cathode channel, the pressure drop observed at the cathode side is higher than at the anode side. He et al. [23] monitored the pressure drop at the cathode and showed a strong correlation between the flooding level and the amplitude of losses due to mass transfer limitations associated with cell flooding. The fluctuation in the pressure drop at the cathode along with the cell voltage of an operating fuel cell was documented by Trabold [3] and is shown in Figure 2.2.

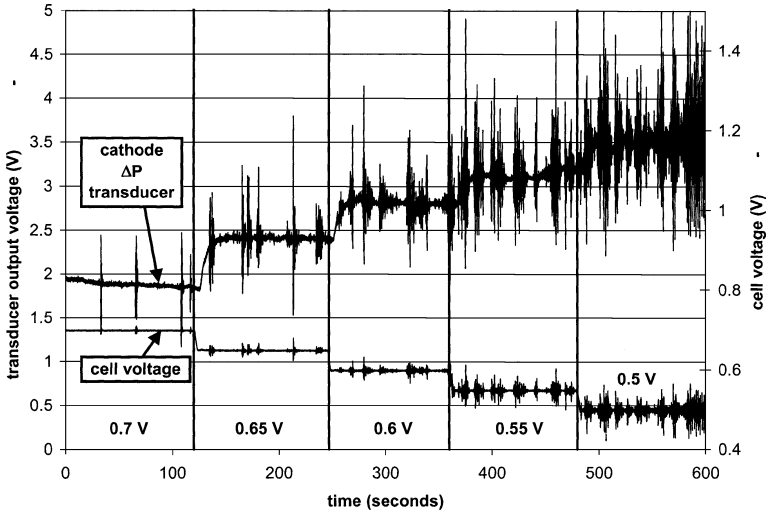

Figure 2.2. Correlation between fluctuations in cathode ΔP signal and cell voltage (reproduced from [3] with permission of Heat Transfer Engineering).

It clearly demonstrates that the mean cathode pressure drop increases as the cell voltage decreases. This happens because more water accumulates at low voltages, resulting in a significant variation in the pressure drop signal. The pressure drop signal can be further examined to deduce a ratio known as the two-phase friction multiplier [24], Φ_g^2, defined as the ratio of two-phase flow pressure drop to the single gas phase pressure drop:

$$\Phi_g^2 = \frac{\Delta P_{2\phi}}{\Delta P_g} \tag{2.1}$$

where $\Delta P_{2\phi}$ and ΔP_g are the pressure drops with two-phase flow and with single-phase flow in the channel, respectively. Wang et al. [25] have demonstrated that this ratio can be used as a simple indicator for the liquid buildup in a PEMFC channel. Lu et al. [18] conducted an ex situ investigation of flow maldistribution and the pressure drop effect. This ratio was presented in the form of superficial air velocities relative to superficial water velocities as shown in Figure 2.3.

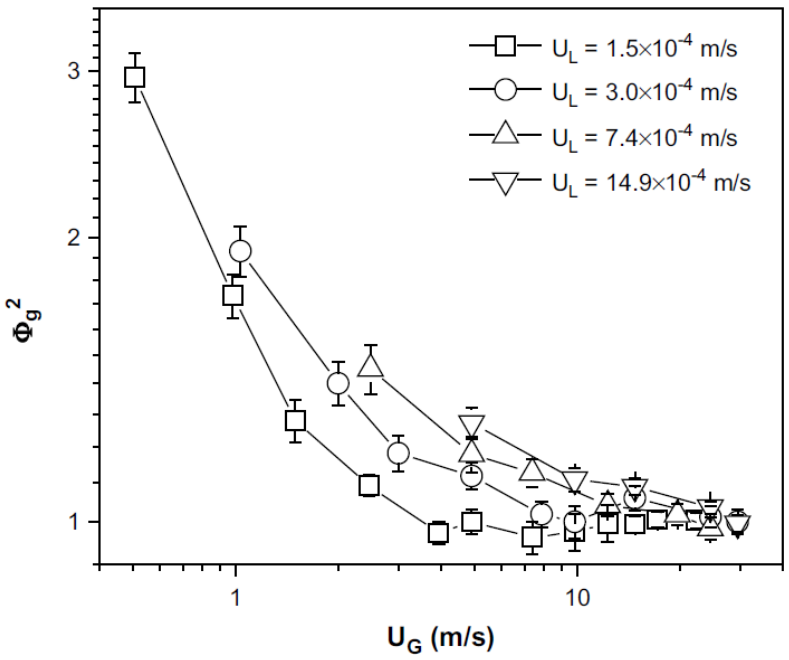

Figure 2.3. Two-phase friction multiplier versus the superficial air velocity under different superficial water velocities (reproduced from [24] with permission of Chemical Engineering Progress).

At low air velocities, the two-phase flow friction multiplier is greater than unity due to liquid water buildup. Thus, the highest Φ_g^2, indicating high water buildup result in slug flow. When the air velocity is increased, Φ_g^2 will decrease and approach unity. The relationships between pressure drop and flow regimes are highly correlated. As reported by Lu et al. [18], two-phase flow at low superficial air velocities is dominated by slugs or semi-slugs and lead to large fluctuations in the pressure drop and severe flow maldistribution. At higher air velocities, a water film flow regime produced smaller but more frequent fluctuations in the pressure drop, resulting from the water buildup at the channel-exit manifold interface. A further increase in the air velocity shifted the flow regime into mist flow where there is very little water buildup and the pressure drop is very small.

2.4. Effect of Channel Geometry and Surface Properties

A typical flow field of a PEM fuel cell consists of a series of channels and ribs with a cross-sectional area of the channels of the order of a square millimeter. The channel geometry has a prominent influence on the performance of the fuel cell due to its impact on flow and water management. The main geometric parameters of the flow field include length, depth, width and the rib width of the channel. Further geometric characteristics depend on the production process such as the rib-wall radii, the channel-bottom-wall radii and the wall angle. A cross sectional view of a typical flow channel is shown in Figure 2.4 [26].

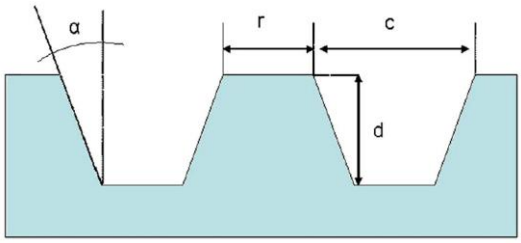

Figure 2.4. Cross sectional view of typical flow channel. r, rib width; c, channel width; d, channel depth; α, wall angle (reproduced from [26] with permission of International Journal of Hydrogen Energy).

Scholta et al. [27] investigated fuel cell performance in several different channel geometries. They found that channel and rib widths in the range of 0.5 to 1.0 mm are advantageous for fuel cell performance. In addition, it was determined that narrow channel dimensions are preferred for high current densities, whereas wider dimensions are better for low current densities. Shimpalee and Van Zee [28] numerically investigated the influence of rib and channel dimensions for a fixed depth of 0.55 mm and concluded that for a fuel cell with 200 cm^2 active area a wider channel (1.0 mm vs. 0.7 mm) with a smaller land width (0.7 mm vs. 1.0 mm) improves performance and flow distribution uniformity. However, for a fuel cell with 100 cm^2 active area, the performance effects of these two parameters depend on the operating conditions.

Aktar et al. [26] studied the effects of channel shape and aspect ratio on pressure drop. They considered four different rectangular geometries with different aspect ratios and a triangular geometry. The optimum geometry was found to be a rectangular channel 1 mm wide and 0.5 mm deep. This particular geometry exhibited the best water removal capability at a reasonable pressure drop. Similar findings were also reported by Kumber et al. [9]. The triangular flow channel geometry did not improve the water removal characteristics or influence the pressure drop enough to move the droplet. Zhu et al. [29] numerically investigated the effects of different channel geometries on water droplet dynamics in a single channel. Simulations for microchannels with different cross-sectional shapes, including rectangles with aspect ratios from 0.1 to 2, a trapezoid, an upside-down trapezoid, a triangle, a rectangle with a curved bottom wall, and a semicircle were compared. For the cases of rectangular channel geometries, the longest detachment time and the largest detachment diameter was seen in the geometry with an aspect ratio (depth/width) of 0.5. The longest removal time was seen in the geometry with an aspect ratio of 0.25. However, the pressure drop for the geometry with an aspect ratio of 0.1 was the highest. They concluded that there is no optimum design in channel geometry in terms of finding a low pressure drop and efficient water removal.

Considering the effect of capillary forces, Metz et al. [30] presented a secondary channel design on top of a triangular cathode gas microchannel for passive water removal as shown in Figure 2.5. It was concluded that cathode walls with low contact angles as well as opening angles larger than 20° are best suited to facilitate water removal in

realistic situations. Their flow field design stabilized the cell at 95% of its initial performance compared to 60% when using the standard design without a secondary channel.

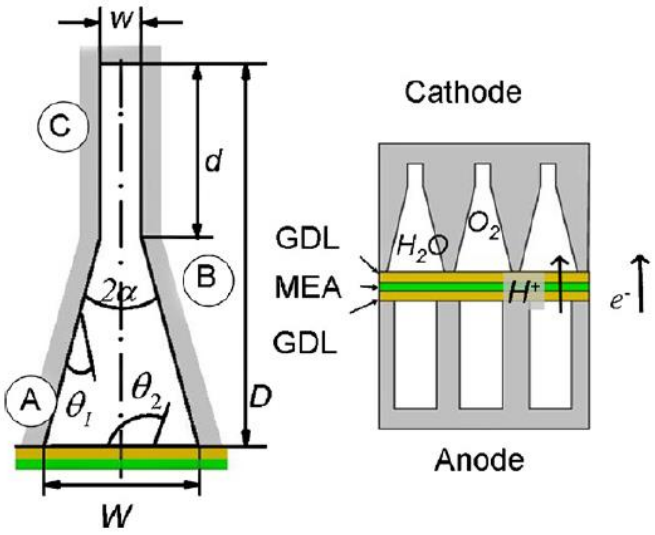

Figure 2.5. Schematic of channel design (left) and integration into PEMFC (right) (reproduced from [30] with permission of Sensors and Actuators A).

Owejan et al. [31] used neutron imaging to compare the water accumulation in different GDLs and microchannels. They reported that hydrophobic coating flow field channels retain more water. However, these channels also contain a greater number of smaller slugs in the channel area, improving the fuel cell performance at high current densities. They also found that the triangular channel geometry retained less water than rectangular channels of the same cross-sectional area, and the water is mostly trapped in the two corners adjacent to the diffusion media.

More recently, an experimental investigation on the effect of channel geometry and orientation as well as the wettability was analyzed by Cheah et al. [32]. It was shown that larger water slugs formed in a hydrophilic channel in spite of reducing surface energy for water removal but will hinder the mass transfer for the reactant gas to get underneath the slug and diffuse into catalyst layer. The hydrophobic channel, on the contrary, produces smaller water slugs and requires more energy for removal but the reactant transport is better improved. They suggested considering all these factors in order to obtain an optimal gas channel design.

It is still not clear as to whether the flow channel wall should be more hydrophobic or more hydrophilic in order to facilitate water removal. Whether or not the water exhibits a wetting or a non-wetting behavior inside the channels is unlikely due to the single parameter of hydrophobicity. Rather, the wetting characteristics of water inside the channel will also depend on the surface material properties, the surface roughness and the geometry of the microchannel.

2.5. Status of Prediction Method

Water transport is a predominant concern in the design of PEMFC flow microchannels. The flow regimes differ from classical two-phase flows because of the confined geometry, non-wetting and rough surfaces, and the dominant effect of surface tension and surface forces [33,34]. Visualization has been employed extensively to study these flows [35], but quantitative measurements remain scarce. The potential of Volume-of-Fluid (VOF) based CFD simulations, Lattice Boltzmann methods (LBM) and Level set methods (LSM) for fuel cell flows has been demonstrated [36–41], but these remain limited by the inability to resolve the roughness of the GDL surface and by fundamental issues regarding the physics of moving wetting lines [42,43].

As described in Section 1.1, the water transport mechanisms in PEMFCs include electro-osmotic drag, capillary force, back diffusion, and multi-component two-phase flow. The water droplets passing through the GDL and appearing in the gas flow channels had been observed and shown to be the source of water. Therefore, accounting for the corresponding droplet dynamics on the channel surface is a central issue in the description and modelling of the two-phase flow phenomena involved in gas channel. The following section will summarize different prediction methods focused on the droplet dynamic issue.

2.5.1. Force balance method on droplet detachment

Liquid water removal from GDL has been studied thoroughly [7,9,44] and the corresponding water droplet detachment models were reviewed by Schillberg and Kandlikar [45]. To better describe the problem, several definitions were introduced to describe droplet dynamics. The droplet height and static contact angle are schematically

shown in Figure 2.6a. The contact line is the boundary where the three phases meet at the interface of air, water and the GDL. When a droplet has no transverse forces acting on it, the contact angle is constant around the entire contact length which is the so-called static contact angle. When the droplet is experiencing shearing forces in the fuel cell channel, the droplet generally tilts toward the direction of flow and the contact angle varies along the line of contact as illustrated in Figure 2.6b.

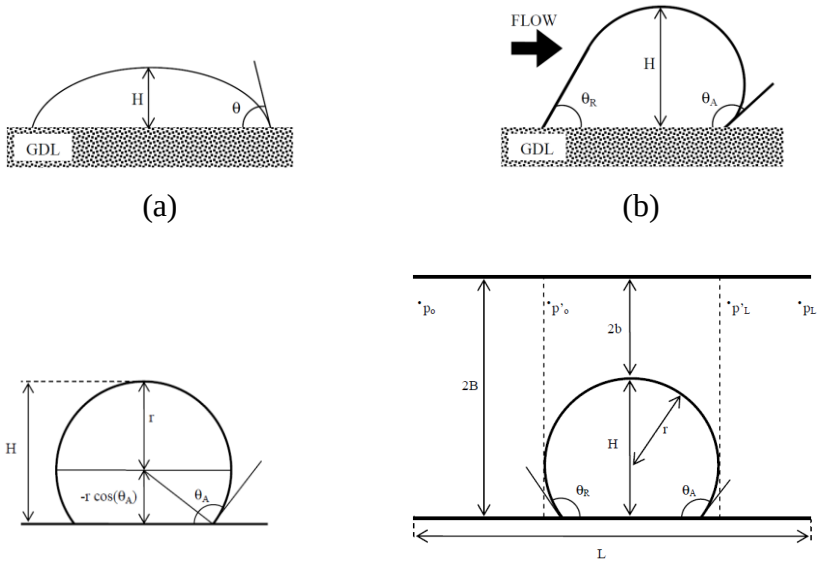

Figure 2.6. Schematic of (a) droplet height and contact angle, (b) droplet subjected to a shear flow with resulting deformation and dynamic contact angles (c) spherical droplet geometry (d) control volume (reproduced from [45] with permission of ASME Conference Proceedings).

The advancing (θ_A) and receding (θ_R) contact angles represent contact angles in the downstream and upstream directions, respectively. These angles are the so-called dynamic contact angles and represent the effect of two forces: a drag force and a surface adhesion force, which balance on the droplet surface and contact line. This variability in the contact angle around the droplet is a way to measure its deformation and stability. The drag force tends to move the droplet away from its location and is a sum of the shear stress force and the pressure force, whereas the surface adhesion force comes from surface tension which acts to hold the droplet in place, pushing against the flow. The droplets depart from the surface as long as the drag force exceeds the surface adhesion

force. The subject of displacing liquid droplets from solid surface is a fundamental problem and has attracted considerable interests by many researchers [46–50]. However, the large range of conditions experienced by the droplets makes their dynamics quite complex.

A simplified model that is based on the force balances and droplet-geometry approximations was presented by Chen et al. [7] to predict the onset of instability leading to the removal of water droplets at the GDL and gas flow channel interface. A spherical droplet under a control volume is schematically described in Figure 2.6c-d. The overall pressure drop is then related to find the drag force and after balancing this force with the surface tension force, the droplet detachment can be described by Eq. (18) in [7]. They concluded that the droplet removal can be enhanced by (a) increasing flow channel length or mean gas flow velocity, (b) decreasing channel height or contact angle hysteresis (the difference between the advancing and receding contact angles) or (c) making the GDL more hydrophobic. The effect of mean air flow velocity on the droplet was represented in terms of an instability window by analyzing the contact angle hysteresis of different shape of droplet, channel length and flow velocity in Chen et al. [7]. A larger unstable area in the stability window is desirable for enhanced water removal, as this indicates a higher probability of droplet detachment.

In comparing the experimental and numerical results, the force balance model provides a reasonable agreement in describing the droplet dynamics. Based on the data Chen et al. [7] obtained the following criterion for prevention of clogging of the channel by water droplets:

$$\left(\frac{L}{2B}\right)\left(\frac{\mu_{gas}U}{\sigma}\right) > \frac{\pi}{12} \tag{2.2}$$

where L is the length of the flow channel, μ_{gas} is the viscosity of flowing gas, U is the average velocity along the flow direction, σ is the surface tension and 2B is the channel height. The left hand side of Eq. (2.2) represents the product of the channel length-to-height aspect ratio with the capillary number, and can be treated as an initial estimate of the flow regime in a gas channel.

Similar to Chen et al. [7], Kumbur et al. [9] conducted a combined theoretical and experimental study of the influence of controllable engineering parameters on liquid droplet deformation at the interface of the GDL and the gas flow channel. They proposed additional parameters including Reynolds number and droplet aspect ratio which affect the water droplet instability. They used an ex-situ approach consisting of a rectangular 5 mm × 4 mm flow channel. Although the channel dimensions were substantially larger than those of a typical PEMFC channel, the proposed analysis and results provide a good representation of salient droplet behavior in the gas channel and indirectly support the approach leading to Eq. (2.2). The overall trend is that decreasing the channel height makes droplet detachment more likely; however the predicted onset of instability/detachment is delayed. Recently an improved analysis that yields improved agreement with experiments was proposed by Miller [51] based on the same concept as Chen et al. [7] and Kumbur et al. [9] but with a more rigorous application of the force balance.

In summary, the most common results in droplet dynamics are [45]:

(1) Increasing hydrophobicity of the GDL tends to decrease the droplet height at detachment and reduces interaction with channel walls.
(2) Decreasing the channel height or increasing the channel length makes droplet detachment more likely.
(3) Increasing the gas channel mean velocity will result in a decrease in the droplet height at departure.
(4) Taller droplets tend to have larger contact angle hysteresis.

2.5.2. Volume-of-Fluid (VOF) method

The VOF method is a computationally intensive method developed in the early 1980s [52]. With the availability of increasing more powerful computing resources, the method has gained increasing acceptance to simulate time dependent flows in immiscible multi-phase systems. In VOF methods, the location of the interfaces is determined by applying a surface tracking technique to a fixed Eulerian mesh; the method can thus be readily implemented into established CFD frameworks. A volume fraction indicator is used in conjunction with a reconstruction technique to determine the location and shape of the

interface. A key feature of the VOF method is the ability to capture the effects of surface tension using a continuum surface force approach. Surface tension is an important and often dominant force in microchannel flows.

Quan et al. [53] studied a serpentine single channel using the VOF method. The inlet air flow velocity was fixed at 10 m/s together with an initial water distribution. This initial water distribution was by starting the simulations in the presence of a single droplet or a series of droplets freely suspended at the inlet or attached on the channel wall. The simulations show that the bend/switchback area plays an important role in determining water behavior inside a U-shaped microchannel due to the combined effects of shear stress, wall adhesion, gravitational force, and surface tension. The results reported in this study though providing some interesting qualitative insights, should be treated with a good deal of caution because, a) the grid resolution was very coarse and inadequate, and b) in an actual fuel cell water is transported through the GDL and emerges into the cathode gas channel as opposed to being freely suspended initially attached to the wall. Cai et al. [54] studied the mobility of water droplets and films inside a straight channel and investigated the effects of hydrophilic and hydrophobic properties of microchannels using the VOF method. Again, initial conditions were prescribed with water film covering the wall. Results showed that the material properties of the channel side-wall play an important role in water transport, with faster water removal on a hydrophobic surface. A hydrophobic membrane electrode assembly (MEA) surface and hydrophilic channel side walls could prevent water accumulation on the MEA surface.

Zhu et al. [55] introduced an improved, though still idealized, representation of the process in a PEMFC, by modelling the emergence of water form a pore into the cathode microchannel. The first sets of exploratory VOF simulations presented by the group were two dimensional and were later extended to three dimensional [29,36,56]. It was found that accounting for the initial connection of a droplet to a pore could yield significantly different dynamics; additionally, the critical air velocity for droplet detachment are also significantly higher for cases when a droplet is assumed initially stagnant and sitting on the surface. Simulations were also presented using water emergence from several pores illustrating the even more complex dynamics arising from droplet to droplet interactions, and merging. Another recent contribution using VOF is due to Chen [57] who conducted

parametric simulation for different dimensions of a gas and water channel using the commercial package Flow-3D. He derived an analytical solution using a simplified explicit model, which is based on a simple force balance between pressure drag and surface tension. The results showed that by making the GDL surface more hydrophobic, decreasing contact-angle hysteresis, and decreasing channel height one can reduce the critical air-flow velocity.

To study the two-phase flow patterns in PEMFCs gas flow channel, Ding et al. [58] employed a numerical modeling using VOF method. The GDL surface structure was simplified by opening 320 pores on the surface with the same diameter of 400 μm considering a typical 50% porosity of open area on GDL surface [59]. Their results show that the flow pattern evolves from corner droplet flow, film flow, annular flow and finally slug flow.

2.5.3. Level set method (LSM)

Level set methods treat the location of a propagating interface as the zero value of a higher order continuous level set function. Given the initial value of the speed of the propagation of each point on the interface, the interface location can be formulated as an initial value problem. Level set methods are advantageous in that they do not require any adaptive meshing of the interface as it propagates, and they handle sharp corners and merging fronts rather well. In addition, there is no need for reconstruction of the interface as is done with VOF methods, and level set methods are easily extended to multiple dimensions [60]. Some of the first work on using level set methods for two phase flow simulations was done by defining the level set function to be the distance of a given point from the air/water interface. In air, the distance is defined to be negative, while in water the distance is defined to be positive. A projection operator is used to reduce the Navier-Stokes equation, and an equation for the level set function is computed instead of solving equations for density and viscosity. By solving an equation for the smooth level set function, level set methods avoid the numerical difficulty of solving equations for density and viscosity at the air/water interface where there are discontinuities. Instead, the density, viscosity, and curvature (to compute the surface tension) are computed from the

level set function [61]. To obtain higher resolution of water droplets, adaptive meshing techniques were later applied to the level set method [62].

Several studies have been done using level set methods to simulate two-phase flow in PEM fuel cells. Mukherjee and Kandlikar [40] analyzed the growing water droplet inside a model cathode channel using a level set method applied in two dimensions. The channel had a cross sectional area of 1 mm^2 and a length of 2 mm. They analyzed the growth and departure of a water droplet inside a channel with air flowing through it. The droplet departure phenomenon was found to be hindered by excessive water flow rates and the increase in surface wettability. They also found that the droplet departure diameter decreased as the contact angle at the channel wall was increased. More recently, Choi and Son [41] presented the droplet dynamic in a model cathode channel with multiple poles using a level set method applied in two dimensions. They found that as the air speed in the microchannel increases, the detachment diameters of water droplets decrease, the surface area coverage of water decreases, and the time it takes for water to leave the microchannel decreases. This indicates that the air speed is critical in the removal of water from the microchannel. Numerical simulations of two pores in the microchannel indicate that the merger of two water droplets is more likely to occur when the distance between the pores is decreased or when the pores are oriented in the same direction as the airflow. Merging water droplets covered more surface area and took longer to leave the microchannel, indicating that these effects inhibit the removal of water from the microchannel. Finally, it was observed that droplets formed which touch the sidewall and bottom wall take longer to leave the microchannel, and are in general larger than droplets that only touch the bottom wall.

2.5.4. Lattice Boltzmann method (LBM)

LBM is a relatively new technique which has its roots in lattice gas cellular automata and particle methods. The technique has gained increasing adoption for simulating a wide range of flows, due in part to the relatively fast and simple numerical algorithms. Unlike classical CFD methods, which solve the conservation equations (mass, momentum, and energy) for macroscopic quantities; LBM models the fluid as consisting of particles which propagate and collide over a discrete lattice mesh. Due to its particulate nature and

local dynamics, LBM has several advantages over other conventional CFD methods, especially in dealing with complex boundaries (such as porous media), accounting for microscopic interactions and non-continuum effects (i.e. larger Knudsen number flows), and parallelization of the algorithm [63]. Intrinsic features enable the LBM to model phase segregation and interfacial dynamics of multi-phase flow, which are difficult to handle in Navier-Stokes based CFD methods. More recently, the LBM has been extended to the simulation of multi-phase fluid flows [64], though issues remain to be addressed to make the technique fully functional in such flows. A few applications of LBM to study transport phenomena in PEMFCs have been reported. Fei and Hong [65] simulated the two-phase flow of methanol/CO_2 in a microchannel in a direct methanol fuel cell, and investigated CO_2 bubbly flow phenomena in the microchannel under different operation conditions. Park and Li [66] presented a 2D two-phase LBM simulation of liquid water flowing through a model of the fibrous structure of carbon paper (GDL). The LBM study of water droplet dynamics on a hydrophobic surface of a gas flow channel in PEMFC was published by Hao and Cheng [67]. They used the LBM multiphase free energy model to simulate the formation of a water droplet emerging through a micro-pore on the hydrophobic GDL surface and its subsequent movement under the action of shear flow. The computational model and domain were similar to those used in Zhu et al [56]; the domain considered consisted of a 1200 μm long microchannel with a cross section of 600 μm × 300 μm a water pore of 90 μm to simulate the water transport from the GDL. The water and air velocity were fixed at 0.075 m/s and 3.86 m/s, respectively. One benefit when using mesoscopic level simulations with LBM is the improved description of the dynamic change of contact angle. As discussed later in Section 2.5.5, this is a key requirement for physically realistic simulations. Similar results to the VOF results of Zhu et al. [56] were reported, consistent with well-established trends, i.e. water droplet removal was found to be facilitated by a high gas flow velocity on a more hydrophobic GDL surface, and a highly hydrophobic surface induced lifting of water droplet from the GDL surface. An analytical model based on force balance was also presented to predict the droplet detachment size. However, characteristic roughness of an actual GDL surface was not considered in this work.

Several approaches have been proposed to simulate two-phase flow using LBM. For example, Gunstensen et al. [68] developed a multi-component LBM on the basis of two-component lattice gas model; Shan and Chen [64] presented a LBM model with mean-field interactions for multi-phase and multi-component fluid flows; Swift et al. [69] proposed a LBM model for multi-phase and multi-component flows using the concept of free energy; He et al. [70] developed a model using an index function to track the interface of multi-phase flow. Although the LBM methodology is a promising method for multi-component/phase flows, one key issue is that all the schemes listed above are limited to small density ratio (typically less than 20), and become numerically unstable for higher density ratios [71]. This is a serious limitation since in most liquid-gas systems of interest the density ratio is usually larger than 100, and in the specific case of PEMFCs the density ratio (water to air) is of order 1000. To overcome this limitation, Inamuro et al. [72] proposed a LBM for incompressible two-phase flows with large density differences by using the projection method. In this method, two particle velocity distribution functions are used. One is used for calculating the order parameter to track the interface between two different fluids; the other is for calculating the predicted velocity field without pressure gradient. The corrected velocity satisfying the continuity equation can be obtained by solving a Poisson equation.

On the other hand, liquid droplet dynamics in a PEMFC gas channel is the result of shear and drag forces due to the gas flow and the capillary forces associated with the liquid-gas-solid interface. A finite steady-state equilibrium or static contact angle, also known as partial wetting, can be reached due to the balance of surface tension forces. Based on these considerations, Briant et al. [73] developed an approach based on the free-energy LBM model introduced by Swift et al. [69] to simulate partial wetting and contact line motion in single or two-component, two-phase fluids. Unfortunately, this method has inherently the disadvantage of the original free energy LBM model of Swift et al. and can only be used to simulate two-phase problems with a small density ratio. The maximum density ratio in the simulations of droplets on partial wetting surfaces was reported to be just around 2. In order to simulate a flow of two-phase fluids with a large density ratio on a partial wetting wall, a new LBM scheme of the LBM is required, for example the approach proposed by Yan and Zu [71]. The multiple-relaxation time LBM method has

also been proposed to overcome to density ratio limitation, but to date has not been demonstrated for high density channel flows, but the results for air-water flow in gas diffusion layers are promising [74].

2.5.5. Modeling of the dynamic contact angle

Volume of fluid (VOF) CFD simulations performed to date by our group and others to investigate the dynamics of liquid water droplets in hydrophobic micro-channels do not rigorously account for the moving contact line mechanisms, which in any case are not fully understood. Noting that surface tension is dominant (Capillary number *Ca <<1*) in the flows of interest, the contact line singularity and the dynamic contact angle will be handled by a suitable semi-empirical formulation in conjunction with a generalization to 3D of a recent dynamic contact angle algorithm [75].

Given the prominent role of surface tension in determining the force balance on water droplets, a resolution of the dynamic effects on the contact line is critical to achieving physically representative CFD simulations. The three-phase contact line presents challenging theoretical and numerical problem in the context of continuum simulations in which a no slip condition is usually applied at solid boundaries and walls. This gives rise to a singularity (infinite tangential stress) when considering the moving contact line. Another issue is the modeling/tracking of the behavior of the dynamic contact angle, which is dependent on the flow conditions around the droplet as well as the contact line motion.

One approach of dealing with the singularity is to impose a slip condition at the boundary. Some of the earlier models proposed in this context are summarized in Table 2.1 based on the assessment of provided in Shikhmurzaev [76]. The main weakness in most of the models is in dealing with the stress singularity. Blake and Shikhmurzaev [77] presented a theoretical approach based on non-equilibrium thermodynamics to deal with this issue and derived the following model for the dynamic contact angle:

$$\cos\theta_S - \cos\theta_D = \frac{2V(\rho_{2e}^{s*} + \rho_{1e}^{s*}u_o)}{(1-\rho_{1e}^{s*})[(\rho_{2e}^{s*} + V^2)^{1/2} + V]} \tag{2.3}$$

where V is the dimensionless contact line velocity, and the non-dimensionalized local densities $\rho_{ie}^{s*} = (\rho_{ie}^{s} / \rho_0^{s})$ are defined for each phase in reference to their equilibrium

values, with indices 1 and 2 referring to the free surface and the liquid-solid interface respectively.

Table 2.1. Slip models examined by Shikhmurzaev [76]

Author(s)	Model Basis	Drawbacks
Huh & Mason [78]	Physical model of the liquid-gas interface motion	Does not display rolling motion. Leads to integrable singularity at the solid boundary.
Durbin [79]	Slip prescribed by bounding maximum shear stress density	Fair but not exact agreement with experiments
Baiocci & Pukhnachev [80]	Problems with one-sided constraints for Navier-Stokes equations and the dynamic contact angle	Fair but not exact agreement with experiments

The dimensionless contact line velocity is given by [77]:

$$V = U\sqrt{\frac{\tau\beta}{\rho_0^s\gamma(1+4\alpha\beta)}} \tag{2.4}$$

and the parameter u_0 is defined as:

$$u_0 = \frac{\sin\theta_d - \theta_d\cos\theta_d}{\sin\theta_d\cos\theta_d - \theta_d} \tag{2.5}$$

The other parameters used found in the model are phenomenological coefficients,

α = Effect of surface tension gradient on the velocity distribution $\left(\alpha \propto \frac{h}{\mu}\right)$

β = Effect of shear stress on the velocity distribution $\left(\beta \propto \frac{\mu}{h}\right)$

τ = Surface tension relaxation time $\left(\tau = \frac{5Sc^2h\mu}{\sigma_{1e}(1-\rho_{1e}^{s*})}\right)$

To date no documented attempt has been made in implementing this model in CFD codes, probably because lack of numerical robustness. Empirical or semi-empirical models appear for now to be more practical. A good overview of more recent semi-empirical models used to account for the dynamic contact angle is provided by Sikalo et al. [81]. Most of the models assume Young's equation is valid throughout the dynamic process and the solid-liquid and solid-vapor surface tensions vary with flow field dynamics, i.e.

$$\sigma \cos\theta_{equilibrium} = \sigma_{solid-liquid} - \sigma_{solid-vapour} \tag{2.6}$$

A key aspect in the definition of the Capillary number (Ca) used in the models is the use of the contact line velocity as the velocity scale, i.e. $Ca = (Vel)\mu/\sigma$. Thus the formulation proposed by Cox [82] reads:

$$Ca = \left(\ln\left(\varepsilon^{-1}\right) - \frac{Q_1}{f(\theta_D)} + \frac{Q_2}{f(\theta_e)} \right)^{-1} \left[g(\theta_D) - g(\theta_e) \right] + O\left(\frac{1}{\ln\left(\varepsilon^{-1}\right)} \right)^3 \tag{2.7}$$

Where ε is a dimensionless parameter based on the static contact angle mechanics. Q_1 and Q_2 are parameters based on the outer flow field and the slip conditions on the wall respectively and the functions f and g depend on the dynamic and equilibrium contact angles.

Another popular contact angle formula, which again uses a capillary number based on the contact line velocity, is the Hoffman-Voinov-Tanner law [81]:

$$\theta_D^{\,3} - \theta_e^{\,3} = C_t Ca \text{ with } C_t \approx 72 \tag{2.8}$$

This formula also involves a capillary number based on the contact line velocity:

$$Ca = \frac{(Vel)\,\mu}{\sigma} \tag{2.9}$$

More recently, a formulation with potentially broader applicability was proposed based on the Hoffman functions [81]:

$$\theta_D = f_{Hoff}[Ca + f_{Hoff}^{-1}(\theta_e)] \tag{2.10}$$

$$f_{Hoff}(x) = \arccos\left\{1 - 2\tanh\left[5.16\left(\frac{x}{1+1.31x^{0.99}}\right)^{0.706}\right]\right\} \tag{2.11}$$

This formulation provides a good fit with experimental data and was implemented recently with some success in both LBM [83] and VOF [51] simulations.

It is particularly important to understand the surface tension force in predicting two-phase flow in a PEMFC microchannel. The main difference between level set methods and the VOF method is that the VOF method uses a discontinuous function (zero in one phase and one in the other) while level set methods represent the interface by a certain contour of a smooth function. Each of these methods has one main advantage and disadvantage. Due to the discontinuity at the air/water interface, the VOF method can suffer from poor accuracy in determining the position of the interface and the calculation of the mean curvature, which in turn determines the surface tension force. The main advantage of the VOF method is that the mass of each fluid is exactly conserved. Level set methods, on the other hand, use a smooth function, allowing higher accuracy in resolving the interface. However, one major drawback of the originally proposed level set method is that mass is not conserved, and significant mass losses may occur. A hybrid numerical method with a high order of accuracy, and good mass conservation properties would be ideal. In this aspect, Sussman and Ohta [84] successfully developed LSM in conjunction with VOF for treating surface tension in incompressible two-phase flow.

It should be emphasized that VOF simulations conducted to date for geometries relevant to PEMFC channels, do not incorporate the physics of the dynamic contact line which is expected to alter significantly the detachment and subsequent evolution of water droplets. The robustness of the VOF methodology is due in some measure to the relative simplicity of the piecewise linear interface calculation (PLIC) procedure used to reconstruct the liquid-gas interface topology. The quality of the approximation impacts

the computation of the surface curvature and hence surface tension forces. In this respect, the contact angle is a critical parameter in evaluating the surface adhesive force. VOF simulations conducted to date for geometries relevant to PEMFC channels, do not incorporate the physics of the dynamic contact line which is expected to alter significantly the detachment and subsequent evolution of water droplets, but rather prescribe a static contact angle based on Young's equation. Dynamic contact angle models using the semi-empirical relations discussed in Section 2.5.5 do improve the physics significantly as shown in recent work by Fang et al. [34] for two-phase slug flows, and recent results obtained by Miller [51] for a model cathode flow, which highlights the large impact the contact line prescription has on droplet dynamics. Dynamic implementation, whether theoretical or empirical (through a series of static angle corrections at each time step in the simulation) impacts the numerical convergence, in order to ensure practical simulation times, this will probably necessitate the implementation of alternative algorithms.

Chapter 3

3 Experimental Investigation of Water Droplet Emergence

The focus of this chapter is the experimental investigation of the water droplet emergence process in a model PEMFC microchannel. Strategies for effective water management rely on an understanding of two-phase flow in gas channels in PEMFCs under realistic operating conditions. Since the primary source of the liquid phase in the gas channel is the water droplet transfer and formation through the GDL, the analysis of water droplet development, evolution and instability behavior on the GDL surface is essential. Building on our preliminary experiments [85] and previous computational work [36], we present an experimental characterization of the emergence, detachment and subsequent dynamic evolution of water droplets in laboratory model of a fuel cell cathode channel. The controlled ex-situ experiments are analyzed using flow visualization and image analysis and provide further insight into the droplet dynamics process and quantitative data for the validation of numerical models.

3.1. Method and Apparatus

3.1.1. Microchannel design

A specifically designed microfluidics platform was fabricated for the experimental study of droplet dynamics. The water pore size and shape as well as the dimensions and

surface properties of the microchannel must be considered in the design in order to model the phenomena of water emergence relevant to fuel cell operation. The microfluidic chip produced for this specific purpose (see Appendix A for detailed fabrication procedure) includes a single channel with a cross section of 250 µm × 250 µm for air flow, as well as a single water injection pore with a cross section of 50 µm × 50 µm located in the middle of the air channel. An elastomer, polydimethylsiloxane (PDMS, Dow Corning Sylgard 184), was selected as the casting material not only due to its transparent and optical clear characteristic but also because its surface is hydrophobic and provides a static contact angle of ~110°, a value similar to that of carbon paper without PTFE coating.

For an actual GDL, pore sizes and locations are randomly distributed thus making it a challenge to predict and control the locations of water droplets in the fuel cells. However, the size of the "pores" is of the order of 50 ~ 100 µm [10]. Experimentally, the emergence pore location can be prescribed on a GDL as was also shown by Kimball et al. [86] by creating 250 µm pores at specific locations. There is also evidence that preferential pathways do form spontaneously in standard treated GDLs [87], probably as a result of residual water. In the present study, the 50 µm square size of water pore is prescribed to represent such conditions.

A complete chip is shown in Figure 3.1a. Viewing from the side, Figure 3.1b, allows observation of an emerging droplet as illustrated. The total length of the microchannel is around 37 mm, whereas the field of view of the microscopic images only covers 3 mm (Figure 3.1c). The dimensions of the channel cross section are the same as reported by Zhu et al. [36], and are suitable for representing a typical gas flow channel used in micro PEM fuel cells [88]; the pore size for water emergence is close to the mean values for carbon paper reported in the literature [10][89]. Keeping in mind that the intended use of the data for validation of various numerical methods [36][67][41], a square geometry was selected as it is computationally more convenient to reproduce without requiring grid skewing or unacceptable grid aspect ratios. The experimental set-up exhibits the most salient physical mechanisms and maintains the appropriate range of values for the key non-dimensional parameters.

Since gravity is perpendicular to the direction of water emergence, it is necessary to clarify the potential gravitational effects. The Bond number, denoted as the ratio of the gravitational force to the surface tension force, is defined as

$$Bo = \frac{\rho g L^2}{\sigma} \tag{3.1}$$

where ρ is the density of water droplet, g is the gravitational acceleration, L is the characteristic length of the system (the measured maximum droplet height is around 200 μm), and σ is the surface tension force between water and air. The Bond number in the current system is estimated to be less than 0.0054 indicating that surface tension forces dominate and the effects of gravity are negligible.

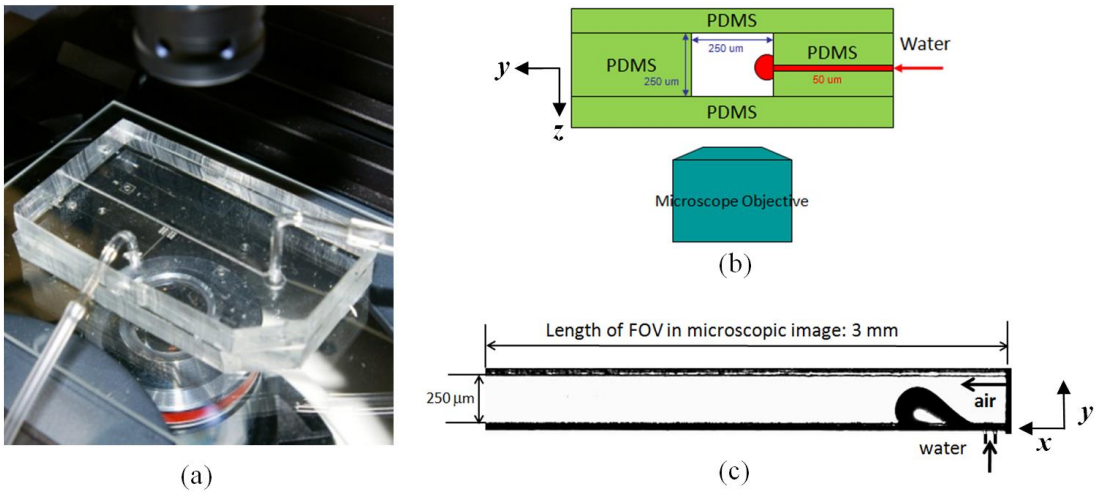

Figure 3.1. (a) PDMS chip for droplet manipulation. (b) Cross sectional view of chip. (c) Field of view in microscope.

3.1.2. Measurement apparatus

A schematic diagram of the experimental apparatus is shown in Figure 3.2. This setup allows injection of water from a small pore that emerges into an air stream while simultaneously monitoring the pressure drop across the gas channel (ΔP), the injected water volume (Q_w), and the air flow rate (Q_a). A side view visualization of two-phase flow is obtained as droplets move and interact with the gas stream inside the microchannel. The data acquisition system was developed using LabView 8.5 (National

Instruments) to integrate the water syringe pump (Harvard Apparatus, PHD 2000), air mass flow meter (Omega, FMA-1600A), differential pressure sensor (Honeywell, FP2000), and high speed camera (Vision Research, Phantom MIRO-4). Data streams are initialized by the high speed camera to trigger the image sampling process. Eight-bit, gray scale images are captured as well as time-resolved pressure drops, delivered water volumes, air flow rates, and inlet upstream pressures and temperatures. These can be measured simultaneously allowing correlation of droplet dynamics with flow regimes. The collected data provide initial conditions, making the experiments suitable for numerical validation. Digital image processing was performed using the toolbox in Matlab 7.8. Images were recorded through an inverted microscope (Zeiss, Axiovert 200M) and magnified by a 5x objective lens (Zeiss, EC Plan Neofluar). Bright-field illumination using a white light LED was applied throughout the image acquisition process.

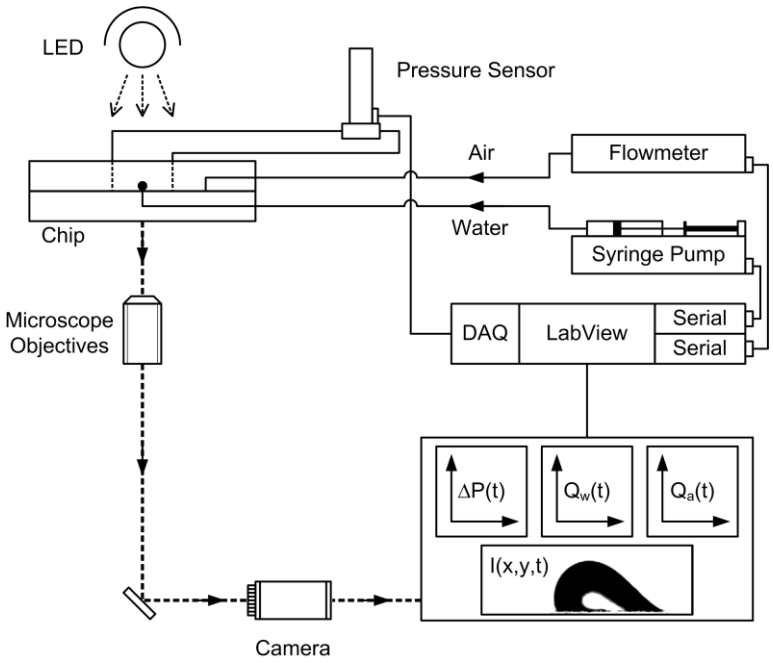

Figure 3.2. Schematic diagram of experimental apparatus.

The high speed camera consists of a CMOS (complementary metal oxide semiconductor) image sensor with a maximum of 800 × 600 pixels. It has a capability of 12 bit pixel depth and a maximum full-resolution frame rate of 1000 Hz. However, in

order to resolve the droplet dynamics, the images were adjusted to covering only 800×72 pixels. This boosts the camera frame rate up to 6006 Hz and provides around six seconds of recording time with the 2GB built-in memory in the camera. Time resolved images were fed into the contact angle measurement software (DataPhysics Instruments, SCA202 v3.51.3 build 187). The tangent method for sessile drop measurement that fit the three-phase point where the liquid touches the solid surface was used. A third degree rational function was used to evaluate the advancing and receding contact angles as well as to measure the droplet height and chord length. The accuracy of the contact angle analysis depends upon the image processing technique and parameters used to extract the drop edge from images. Droplet images are converted into 8 bit gray scale by thresholding, resulting in images consisting of a dark foreground representing the drop, and a white background. When moving from the background into the droplet, a sharp decline in pixel intensity is observed, and the edge of the drop is expected to be in a region along the curve (spline) corresponding to the highest gradient. Using a maximum of 80 points to define the interface profile, a least square fit is used to determine the tangent at the advancing and receding contact points. The raw image from the high speed camera provides a resolution of 4.54 µm/pix. Due to the small droplet dimension (100-350 µm), the raw images are imported into the contact angle evaluation program after a three-fold magnification. Combining the uncertainties result in a maximum uncertainty of ±1.3° of contact angle evaluation.

3.1.3. Flow conditions

The flow channel described in Section 3.1.1 (250 µm × 250 µm cross section and 37 mm length) nominally simulate an operating fuel cell active area (A_{act}) of 0.0925 cm^{-2}. The volumetric flow at the cathode due to water production and anode-to-cathode transport is given by:

$$Q_w = \frac{(1+2\alpha) i A_{act} M_{H_2O}}{2F} \tag{3.2}$$

Where α is the net drag coefficient, A_{act} is the active area, i is the current density, M_{H_2O} is the molecular weight of water, and F is Faraday's constant. For operation at i = 2.0 A

cm^{-2} with $\alpha = 1$, the water flux is 33.6 $\mu L\ min^{-1}\ cm^{-2}$. The injection rates used in this study range from 32.4 to 162.2 $\mu L\ min^{-1}\ cm^{-2}$. The higher water flow rates were specifically chosen to allow us to conduct the experiments in a reasonable time and without incurring secondary effects such as evaporation. Appropriate normalization of the time scale and the negligible impact of water injection rates on contact angles and droplet dimensions discussed in the results below support this. The Reynolds numbers for the air flow range from approximately 50 ~ 1200, representative of a range of operating conditions for parallel and serpentine PEMFC configurations. The inlet flow conditions used in the experiment are summarized in Table 3.1.

Table 3.1. Flow inlet conditions.

Test matrix for flow regime	
Air flow rate, Q_a (sccm)	12 ~ 300
Air superficial velocity, V_a ($m\ s^{-1}$)	3.2 ~ 80
Water flow rate, Q_w ($\mu L\ min^{-1}$)	3, 6, 15
Water superficial velocity, V_w ($m\ s^{-1}$)	0.02, 0.04, 0.10
Reynolds number of air, Re	51 ~ 1268
Temperature, T (K)	296

Two specific cases for qualitative droplet dynamic analysis, Case 1: $V_a = 10\ m\ s^{-1}$, $V_w = 0.02\ m\ s^{-1}$ and Case 2: $V_a = 10\ m\ s^{-1}$, $V_w = 0.04\ m\ s^{-1}$.

3.2. Results and Discussions

The flow visualization experiments were analyzed both qualitatively, to develop a flow regime map, and quantitatively, to determine the evolution of the dynamic contact angle, the characteristic detachment frequency and droplet size.

3.2.1. Flow regimes

In order to investigate the water droplet dynamics subjected to a shear flow in the microchannel corresponding to a range of fuel cell operating conditions, three water superficial velocity conditions were investigated. The superficial velocity is defined as the bulk velocity of the water flowing through the cross sectional area of the channel. Visualization of the water emergence process could be typically categorized into three distinct flow regimes shown in Figure 3.3:

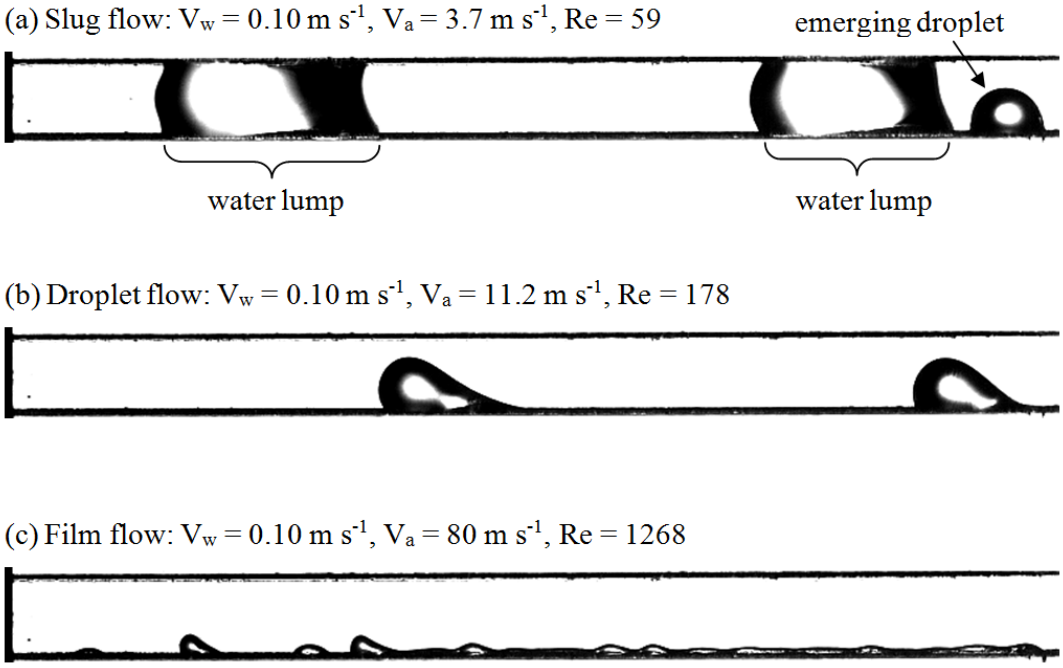

Figure 3.3. Typical flow regime in microchannel

1. *Slug flow* (Figure 3.3a) occurring at low air superficial velocities. The drag force is minimal at these velocities, and the droplets keep growing until they contact the channel wall and are then either slowly convected or remain on the wall until caught up by another droplet with which they coalesce and then move along the channel toward the outlet. Slug flow obstructs and limits air flow through the channel and thus

increases the possibility of flooding and decreases the water removal effectiveness in the channel.

2. *Droplet flow* (Figure 3.3b) occurring at increasing air velocity, with an individual droplet emerging from the water pore and remaining pinned at the water pore due to surface tension forces, until it grows to a critical size at which the air drag force overcomes the surface tension force. In this regime, the effect of air velocity on the changing shape of the emerging droplet and the time evolution of the emerging process can be clearly identified.

3. *Film flow* (Figure 3.3c) that ensues with further increase in air flow velocities that drag the droplets and induce the formation of an elongated and almost continuous wavy water film. Large droplets are no longer observed. Instead, smaller protrusions appear at the boundary of the film and are rapidly flattened due to a high air flow rate.

In summary, the water droplets can be shearing off the PDMS surface with a higher air flow velocity, causing only a minimal obstruction. This occurs most often while droplets are small compared with the channel geometry. Upon detachment, the droplet can interact with the different channel walls. The detached water droplets can adhere to the surfaces, coalesce and build up into water lumps, films or slugs, blocking the flow passage over time. The different coalesced structures of water inside the flow channel will produce different flow instabilities.

The different flow regimes are typically presented in two dimensional flow pattern maps, with the two coordinates representing some appropriate hydrodynamic parameters. The most popular coordinates are superficial phase velocities, but dimensionless Weber numbers have also been used, as suggested by Akbar et al. [90]. Both representations are shown in Figure 3.4. Dashed lines are used to delineate the three different regimes based on the testing conditions, and provide the threshold air velocities for the transitions from slug flow to droplet flow and then to film flow at a given water velocity. With increasing

water velocity, the droplet flow regime region becomes smaller, and at some point the slug and film regimes intersect, with transition occurring directly and bypassing the droplet flow regime.

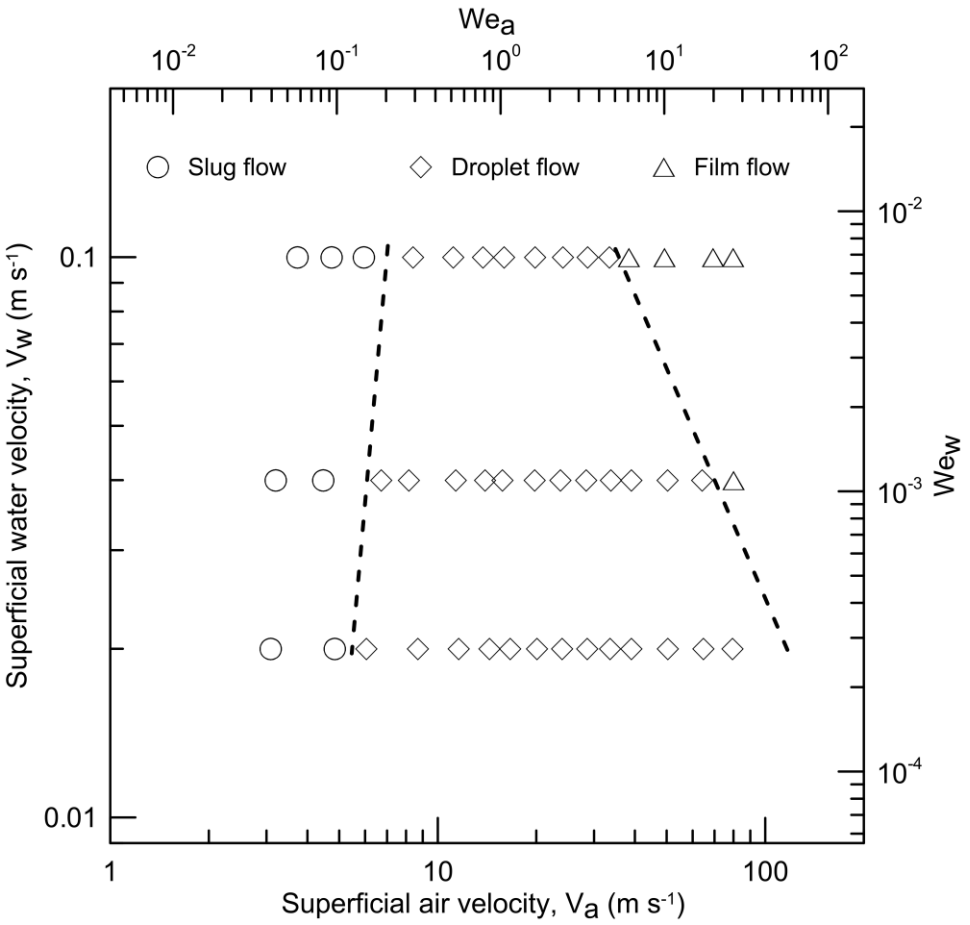

Figure 3.4. Flow map of water emergence phenomena in a model PEMFC cathode gas microchannel.

3.2.2. Droplet emergence frequency

The flow visualization presented above indicates that the periodicity of the droplet emergence process is specific to the flow regime. Time series analysis was performed to further characterize the droplet dynamics using digital imaging processing. Time series raw images are first subtracted from a reference background image taken in the absence of droplets. All images are cropped to the region of interest covering a single droplet in a preselected registered image. This registered image is then compared with other images by using a MATLAB image processing and signal analysis toolbox. Preselected registered image A is compared with every other image B in the same recording series. An algorithm to determine the two-dimensional correlation coefficient index, *r*, is applied based on

$$r = \frac{\sum_m \sum_n (A_{mn} - \overline{A})(B_{mn} - \overline{B})}{\sqrt{\left(\sum_m \sum_n \left(A_{mn} - \overline{A}\right)^2 \right)\left(\sum_m \sum_n \left(B_{mn} - \overline{B}\right)^2 \right)}} \tag{3.3}$$

where A_{mn} and B_{mn} are $m \times n$ matrices, and $\overline{A}$ and $\overline{B}$ are the mean matrix elements. The correlation coefficient values range from 0 to 1. When using the algorithm to compute time resolved image correlations, a few images are randomly selected to serve as the register image A, and are compared with image B in the image stack. The two experimental flow conditions listed in Table 3.1 were selected to demonstrate the concept.

A typical time domain signal for Case 2 is shown in Figure 3.5a and the corresponding frequency spectrum obtained using a Fast Fourier Transform (FFT) analysis is shown in Figure 3.5b, clearly identifying the periodicity. In case 2, the droplet emerges at a dominant frequency of 13.2 Hz. A sample MATLAB source code for determining the correlation coefficient index and emergence frequency is given in appendix B.

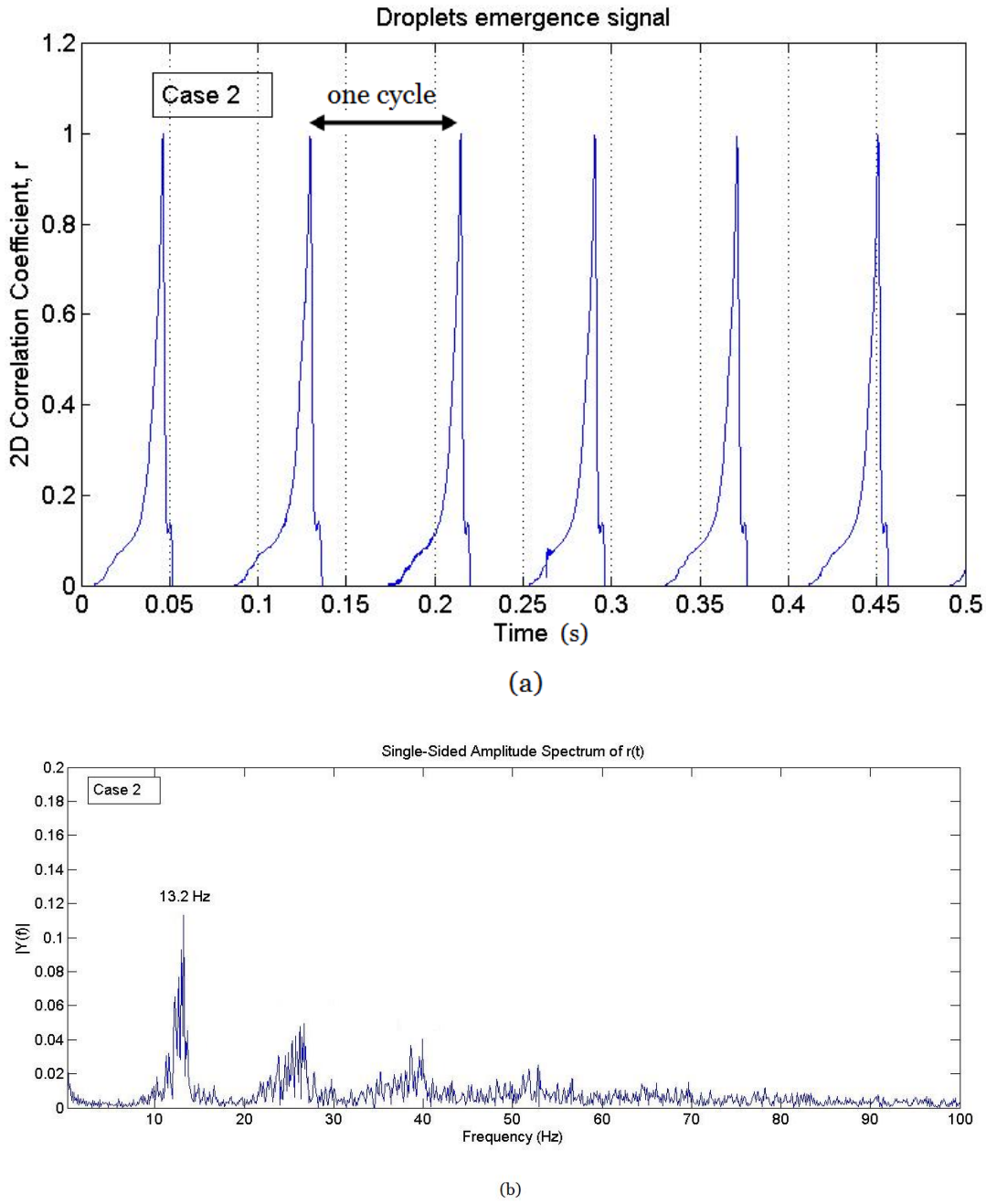

Figure 3.5. (a) Time domain signal and (b) frequency distribution of droplet emergence process.

The evolution of the dominant emergence frequency with flow conditions is presented in Figure 3.6. The low emergence frequency at low air velocities allows droplets to grow sufficiently large to contact the side walls. The frequency increases linearly with air

velocity and reaches its highest value before transitions to film flow. No dominant frequency is observed in the film flow regime, where the process is inherently a periodic due changes in detachment frequency and necking, splitting and coalescence of the films. The volume of a droplet can be further deduced from the water flow rate and the emergence frequency. In the current studies, the droplet volumes reached up to the onset of detachment range from 4.2 to 10 nL, 1.1 to 10 nL and 0.7 to 2.5 nL for water flow rates of 0.02, 0.04 and 0.1 µL min^{-1}, respectively. Interestingly, this suggests that this chip platform is promising for manipulation of a nanoliter droplet.

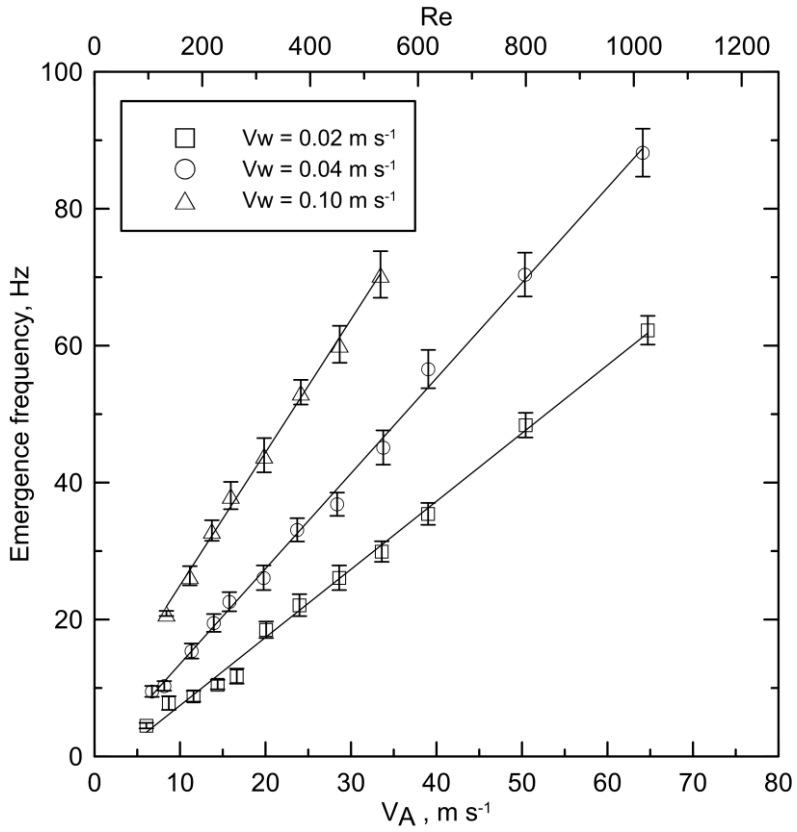

Figure 3.6. Emergence frequency in droplet flow regime under different flow conditions.

3.2.3. Further image analysis of droplet emergence

Figure 3.7 displays the time series images captured at 6006 Hz illustrating the evolution and cyclic nature of the water emergence into the gas stream. Only one cycle of emergence is shown corresponding to Case 2. The emergence frequency is 13.2 Hz (with a period of 75.75 ms), as presented earlier. The right boundary of the droplet is pinned at the water outlet where the air, water and the PDMS surface meet. The dynamics of a droplet is governed by the balance of pressure, shear and drag forces exerted on it. Surface forces dominate the beginning of the growth and emergence cycle (0 to 10 ms) shown in Figure 3.7a-d during which the droplet retains a symmetric shape.

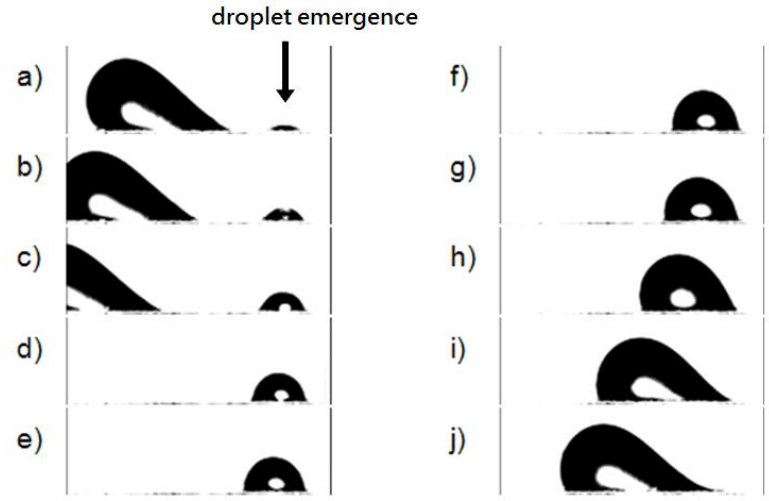

Figure 3.7. Time resolved images of water emerging from a 50 µm square pore in a 250 µm square gas microchannel with the flow condition of Case 2. a) t = 1 ms, b) t = 3 ms, c) t = 5 ms, d) t = 10 ms, e) t = 15 ms, f) t = 20 ms, g) t = 25 ms, h) t = 45 ms, i) t = 65 ms, j) t = 75 ms

Starting with Figure 3.7e, the larger droplet produces increasing blockage of the air flow that results in increasing drag force inducing deformation with tilting toward the downstream direction and the onset of contact angle hysteresis. However, the surface adhesion forces still dominate drag and the droplet remains pinned. For these flow conditions, the droplet does not grow sufficiently large to contact the top and side walls, but eventually detaches (Figure 3.7j) and starts to move along the surface while another emergence cycle begins.

3.2.4. Dynamic contact angle

The high speed visualization images were further analyzed frame by frame to deduce the evolution of the droplet chord and height and of the dynamic contact angles. The advancing (θ_a, upstream de-wetting side) and receding (θ_r, downstream wetting side) contact angles of a droplet vary from the static value as shown schematically in Figure 3.8a, and their evolution during the emergence process up to the point of detachment is presented in Figure 3.8b for Case 2. Three different periods can be identified. Period I (0 ~ 11 ms: surface tension dominated) corresponds to the beginning of emergence. In this region, θ_a and θ_r increase at the same rate which corresponds to a symmetric change of the droplet shape and thus no contact angle hysteresis is observed. In Period II (11 ms ~ 17 ms: transition region), θ_a keeps increasing but θ_r stops increasing. This occurs as a result of pressure forces acting on the upstream surface of the droplet and countering the increase in θ_r due to droplet growth. In Period III (17 ms ~ 75.75 ms) increasing pressure and shear forces combined with growth induce further increase in the advancing contact angle θ_a up to 110°. During this process, significant distortion of the droplet occurs. Conversely, the receding contact angle becomes smaller as the cycle progresses up to detachment. The small variations in measurements around the trend lines are due to local variations in the PDMS surface of each batch of fabricated chips. Additionally the experimental surfaces are not perfectly homogeneous and occasional slip, jump and stick motion of the contact line were observed in flow visualization using a high speed camera. These phenomena are expected to be more pronounced in actual GDL, in which is likely to play an even more prominent role.

The chord length of a growing droplet increases and reaches about 350 μm at detachment which is larger than the channel dimension of 250 μm. This underscores the significant deformation and elongation due to the hydrodynamic forces exerted by the air stream. The assumption of a spherical droplet in the simplified models for predicting the onset of droplet instability [7] are thus only very approximate. The data presented here for the time evolution of the dynamic contact angles can be used to empirically prescribe the dynamic contact angle in order to improve the physical realism of simulation.

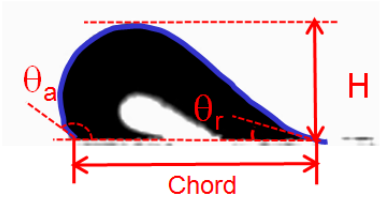

(a)

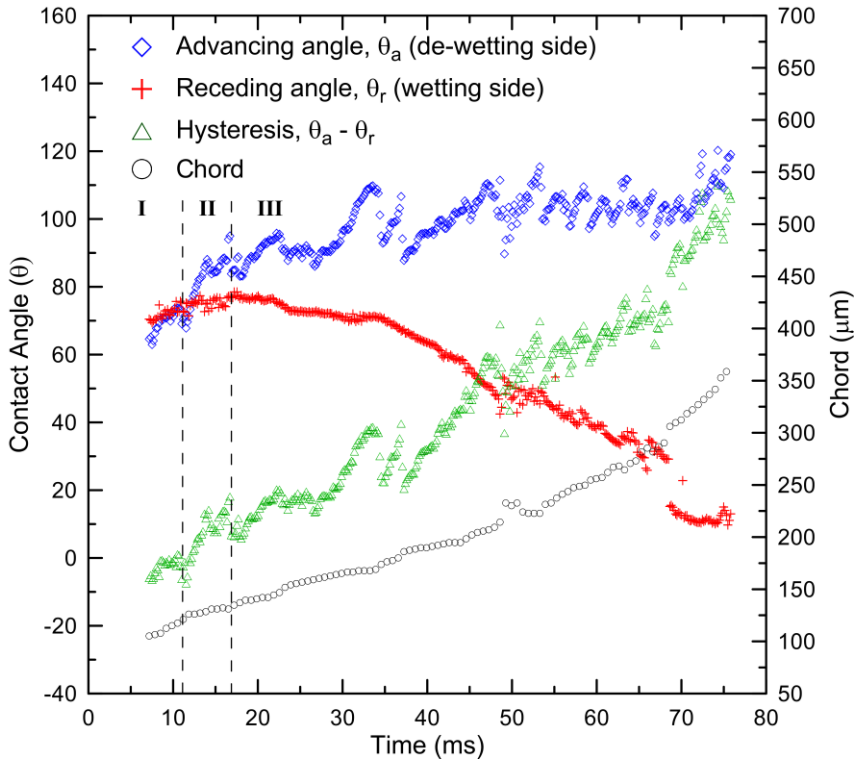

(b)

Figure 3.8. Dynamic contact angle evolution through an emergence cycle (13.2 Hz under Case 2 flow conditions). Period I: surface tension force dominant. Period II: transition. Period III: drag force dominant.

3.2.5. Droplet dynamic at the onset of detachment

When water is introduced into the air stream, the droplet initially emerges, grows and remains pinned at the pore until it attains a critical size and detaches. The detachment droplet size is a function of several parameters, including water and air flow rates surface conditions, and pore size [55]. The droplet chord length, height, and the advancing and receding contact angles can be deduced from the flow visualization at the onset of

detachment. The dependence of the detachment droplet chord (C) and height (H) on air velocity/Reynolds number is plotted in Figure 3.9 for various water injection velocities.

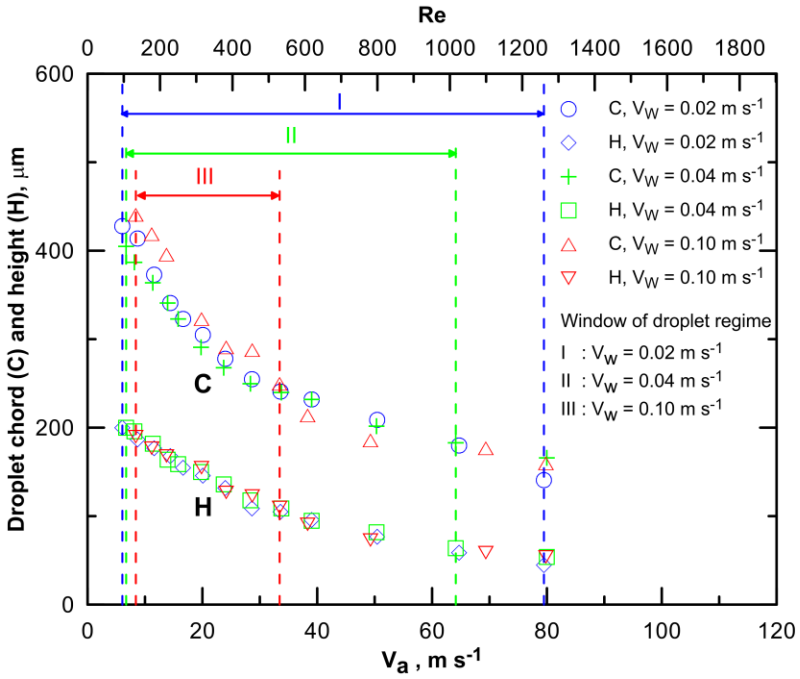

Figure 3.9. Effect of air flow velocity on characteristic droplet size (chord C and height H) at detachment.

The air velocities can be interpreted as the critical operating velocities which must be used in a PEMFC to ensure detachment and removal of liquid water to prevent flooding and the subsequent blockage of the transport of reactants to the reaction sites [2]. The windows in the figure delineate the size of droplet flow regime for three different water injection velocities. The left and right hand sides of the window represent slug and film flow regimes, respectively. The low velocity boundary of the windows at around V_a = 8 m s^{-1} can be interpreted as the threshold air velocity that prevents the formation of slug flow which is characterized by larger droplets and blockage. Slower water injection velocities broaden the droplet flow regime window. The figure also shows a similar trend to the numerical data presented by Zhu et al. [56] with the rate of size decrease tapering at higher velocities.

The effect of the air flow on contact angle hysteresis ($\Delta = \theta_a - \theta_r$) is plotted in Figure 3.10. This angle could be interpreted as the measure of the ability of the droplet to resist the drag force and the capability of the flat PDMS surface to remove water under

controlled experimental conditions. The data for different water velocities collapses to the same curve and decreases linearly from 80° to 40°. As the air flow velocity increases, the flow regime changes from a droplet pattern to a film pattern with a smaller advancing contact angle and a reduction in the contact angle hysteresis.

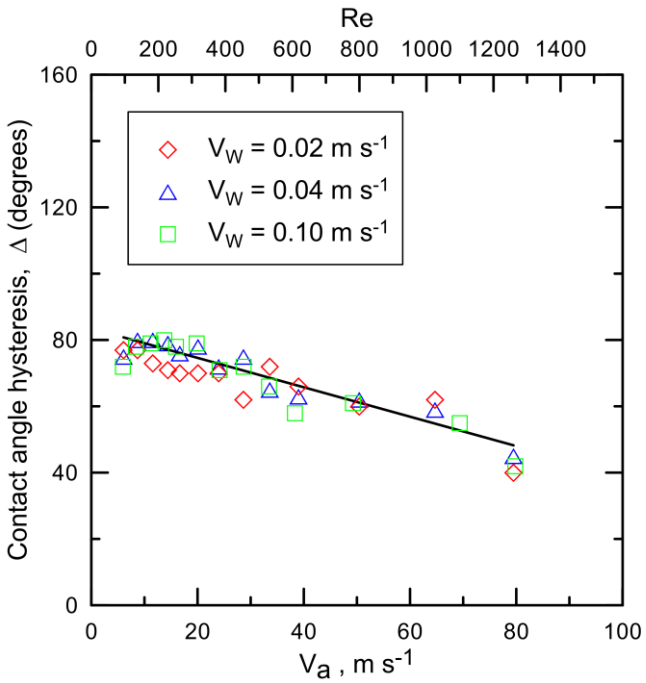

Figure 3.10. Effect of air flow on contact angle hysteresis.

The analysis of Kumbur et al. [9] indicated that the contact angle hysteresis depends on the channel air flow rate (or Reynolds number), droplet size (H and C) and surface properties. The plot of the contact angle hysteresis versus the H/C ratio at different Reynolds numbers is shown in Figure 3.11a. The data differs from that predicted by Kumbur et al. [9]. However, in their analysis, in addition to different flow conditions, the droplet was assumed to be hemispherical and symmetric and the effect of pore pinning was not accounted for. The importance of accounting for pore connectivity in determining the critical detachment size was highlighted by Zhu et al. [36]. The data obtained here reflects the distribution on a flat PDMS surface under flow conditions described in the test matrix of experiments.

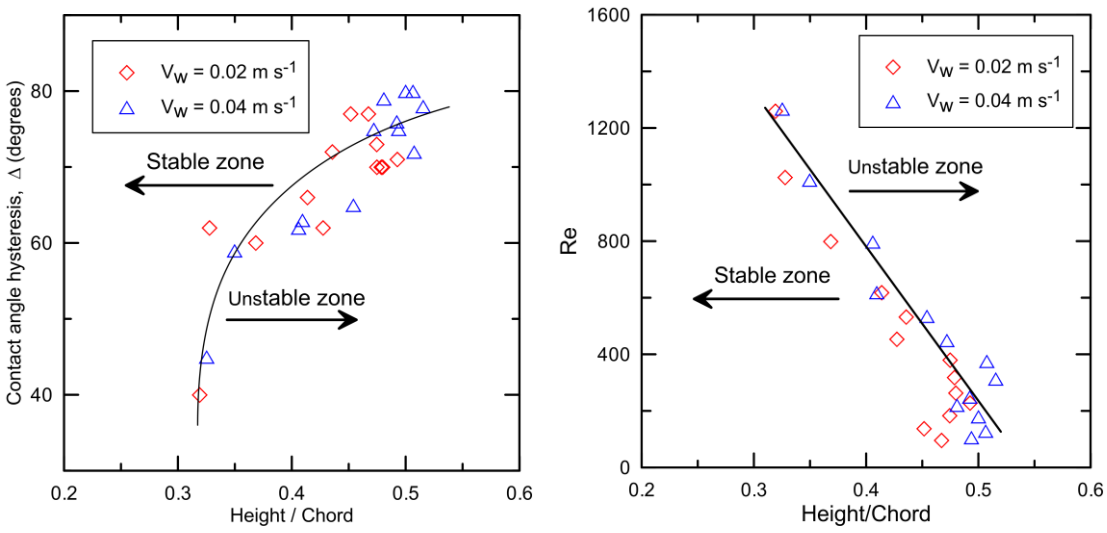

Figure 3.11. Contact angle interpretations and effect of airflow on droplet aspect ratio at the onset of detachment.

For a given droplet size (or aspect ratio, H/C), a higher contact angle hysteresis will increase the capability of the droplet to resist the drag force. The droplet will thus have a broader stability zone as shown by plotting the data appropriately in Figure 3.11a. In fuel cell applications, a broader instability zone is desirable to enhance water removal capabilities. Figure 3.11b shows the critical droplet size in terms of the aspect ratio versus the Reynolds number. A higher Reynolds numbers at a given droplet size increases instability and potential for removal of the droplet. The Reynolds number required to sweep out a droplet is found to increase with decreasing droplet aspect ratio. Spreading of the droplet, as discussed in [9], results in a decrease of the aspect ratio and requires higher air velocities/ Reynolds number for detachment. As shown in the flow visualization, a decrease in the aspect ratio occurs when the flow regime switches to a film flow pattern. This flow regime makes water removal more difficult in fuel cell applications. Another parameter that impacts the droplet detachment process is pore diameter. Varying pore size was outside the scope of the present experiments, but numerical simulations [55] indicate that although the aspect ratio decreases with decreasing pore diameter, the critical Reynolds number for droplet removal decreases as

a result of weaker surface tension due to the reduced connectivity with the pore. The role of pore connectivity is clearly important and requires more in-depth analysis.

3.3. Summary

The dynamics of water droplets emerging from a pore in the presence of a cross flow of air was investigated experimentally using a modeled PEMFC cathode gas channel. Quantitative analysis of high speed flow visualizations was performed to deduce characteristic process frequencies, contact angle hysteresis and critical droplet sizes. The study shows

1. Three flow regimes: slug, droplet and film flow patterns, are identified under different air and water velocities. At low air velocities, slug flow blocks the air flow through the channel. At higher air velocities, a periodic pattern of droplet emergence, growth and detachment appears. Further increase in air velocity induce wavy water film pattern. A flow map of the flow regimes as a function of superficial air and water velocities was presented.

2. For emerged droplets, significantly higher critical air velocities are observed compared to results in the literature which only considered processes starting from droplet initially static on a flat surface. This highlights the important impact of pore connectivity.

3. The dynamic contact angle at the onset of detachment decreases as the air velocity increases; as a result, the flow regime shifts from slug to droplet and film flow. This angle is representative of droplet stability, i.e. its ability to resist the drag force on a given surface.

4. A decrease in the droplet aspect ratio and contact angle hysteresis is observed in the film flow regime, and is found to reduce water removal capacity.

While the experiments presented here were obtained using a laboratory model of a PEMFC cathode, they isolate and represent some of the salient flow features of operating fuel cells, and the data and documented boundary conditions should prove useful for the validation of simulation methods. Two key characteristic of GDLs that will be considered in future work are roughness and inhomogeneities. These are expected to impact the effective contact angle, induce additional pinning and alter the droplet growth and dynamics. Finally, the critical impact of pore connectivity and pinning, which was also qualitatively reproduced in earlier numerical work [36], needs to be incorporated into practical force-balance models that can be used in design.

Chapter 4

4 Numerical Simulation Using VOF Method

The simulation of two-phase flow presents many challenges, particularly for conditions corresponding to an operating fuel cell. To complement the experiments, numerical simulations of the droplet emergence using VOF based free surface capture method were investigated. VOF simulations have been presented for a similar problem as noted in Chapter 1. However to date they relied on a static prescription of the contact angle. The work in this chapter focuses primarily on the implementation of a dynamic contact angle model. Two different approaches were implemented for the treatment of dynamic contact angle of a moving contact line using commercial Computational Fluid Dynamics (CFD) software, CFD-ACE+ and ANSYS FLUENT. Both are well established and widely used for research and development and incorporate state of the art numerical algorithm including a well-documented VOF module. The first approach used for the dynamic contact angle model is through the velocity dependent contact angle function derived from the experiments, and was implemented in the computational framework of free surface module using CFD-ACE+ version 2010. The second approach is by implementing the Hoffman function (cf. Eq. (2.11)) within the user defined function framework of the multiphase flow module using ANSYS FLUENT version 14.0.

4.1. Volume of Fluid Method

The VOF method is a computationally intensive approach first developed in the early 1980s by Hirt and Nichols [52] and refined continuously by many others. The VOF model can model two or more immiscible fluids by solving a single set of momentum equations and by tracking the volume fraction of each of the fluids through the solution of an additional volume fraction transport equation. In each control volume, the volume fractions of all phases sum to unity. The fields for all variables and properties are shared by the phases and represent volume-averaged values, as long as the volume fraction of each of the phases is known at each location. Thus the variables and properties in any given cell are either purely representative of one of the phases, or representative of a mixture of the phases, depending upon the volume fraction values [91]. The volume fraction of fluid q in the cell is denoted as α_q, where:

$$\begin{aligned} &\alpha_q = 0: && \text{The cell is empty of the } q^{th} \text{ fluid.} \\ &\alpha_q = 1: && \text{The cell is full of the } q^{th} \text{ fluid.} \\ &0 < \alpha_q < 1: && \text{The cell has an interface containing the } q^{th} \text{ fluid.} \end{aligned} \tag{4.1}$$

Based on the local value of α_q, the appropriate properties and variables are assigned to each control volume within the domain. The tracking of the interface between the phases is accomplished by the solution of a continuity equation for the volume fraction of one (or more) of the phases. For the q^{th} phase, this equation has the following form:

$$\frac{\partial}{\partial t}\left(\alpha_q \rho_q\right) + \nabla \cdot \left(\alpha_q \rho_q \vec{V}_q\right) = 0 \tag{4.2}$$

in the absence of source terms and mass transfer between phases. The volume fraction equation is not being solved for the primary phase. Instead, it is computed through explicit time discretization based on the following constraint.

$$\sum_{q=1}^{n} \alpha_q = 1 \tag{4.3}$$

Using the explicit approach, finite-difference interpolation schemes are applied to the volume fractions that were computed at the previous time step.

$$\frac{\alpha_q^{n+1} - \alpha_q^n}{\Delta t} V + \sum_f \left(U_f^n \alpha_{q,f}^n\right) = 0 \tag{4.4}$$

where

n+1 : index for new (current) time step

n : index for previous time step

$\alpha_{q,f}$: face value of the q^{th} volume fraction, computed from second order upwind scheme

V : volume of cell

U_f : volume flux through the face based on normal velocity.

The properties appearing in the transport equations are determined by the component phases in each control volume. In general, for *n*-phase system, the volume-fraction-averaged composition variable takes the following form:

$$B = \sum_{q=1}^{n} \alpha_q B_q \tag{4.5}$$

where B is a fluid property such as density or viscosity. This allows the calculation and updates of the entire set of fluid properties in any given cell, based on the phases that are present in that cell. A single momentum equation is solved throughout the domain, and the resulting velocity field is shared among the phases. The momentum equation, shown below, is dependent on the volume fractions of all phases through the properties ρ and μ [91].

$$\frac{\partial}{\partial t}\left(\rho\vec{V}\right) + \nabla\cdot\left(\rho\vec{V}\vec{V}\right) = -\nabla P + \nabla\cdot\left[\mu\left(\nabla\vec{V} + \nabla\vec{V}^{T}\right)\right] + \rho\vec{g} + \vec{F} \tag{4.6}$$

where P is the static pressure, $\vec{F}$ is body force term, ρ and μ are the volume averaged density and dynamic viscosity which can be computed using Eq.(4.5).

In the present study of microchannel, due to the relatively small mass of water droplets, body forces are negligible compare to surface tension forces. For a flow channel, with droplet dimensions in the order of less than 0.5 mm and a water velocity less than 0.04 m/s, the Weber number is:

$$We = \frac{\rho U^2 L}{\sigma} \quad \frac{\text{Inertia}}{\text{Surface Tension}}$$

$$We = \frac{(998)\left(0.04^2\right)(0.0005)}{0.0728} \approx 0.011 \tag{4.7}$$

From experimental observation, the typical dimension of a water droplet is less than 0.5 mm even under extreme operating conditions. Hence, the surface tension force is dominant and approximately 100 times the strength of the inertia force. Further decreasing of water injection velocity will result in smaller droplets and an even smaller Webber number.

Surface tension is accounted for by using the continuum surface force (CSF) model [92] to represent the pressure jump induced by the surface tension within the transition region. This pressure jump depends on the surface tension coefficient and the surface curvature as measured by two radii in orthogonal directions, R_1 and R_2:

$$p_2 - p_2 = \sigma\left(\frac{1}{R_1} + \frac{1}{R_2}\right) \tag{4.8}$$

where p_1 and p_2 are the pressures in the two fluids on either side of the interface. The surface curvature is computed from local gradients of the surface normal at the interface [91].

$$n = \nabla \alpha_q \tag{4.9}$$

where n is the surface normal, defined as the gradient of the volume fraction of the q^{th} phase. The curvature, k, is expressed by the divergence of the unit normal, $\hat{n}$.

$$k = \nabla \cdot \hat{n} \tag{4.10}$$

where

$$\hat{n} = \frac{n}{|n|} \tag{4.11}$$

A continuous transition is implemented in the momentum equation as a volume force source term, F_{vol}, with the following form when only two phases are considered:

$$F_{vol} = \sigma_{ij} \frac{\rho k_i \nabla \alpha_i}{\frac{1}{2}\left(\rho_i + \rho_j\right)} \tag{4.12}$$

where ρ is the volume-averaged density computed using Eq. (4.5). This implies that the surface tension source term for a cell is proportional to the average density in the cell. In conjunction with the surface tension model while using wall contact angle as a boundary condition, the surface normal is expressed in terms of the prescribed contact angle, θ_w.

$$\hat{n} = \hat{n}_w \cos\theta_w + \hat{t}_w \sin\theta_w \tag{4.13}$$

where $\hat{n}_w$ and $\hat{t}_w$ are the unit vectors normal and tangential to the wall, respectively. It is worth noting that the combination of this contact angle with the calculated surface normal one cell away from the wall determine the local curvature of the surface, and this curvature is used to adjust the body force term in the surface tension calculation. Therefore, suitable mesh refinement is necessary at the near wall location.

The geometric interface reconstruction is obtained from a piecewise linear interface calculation (PLIC) method [93]. This assumes that the interface between two fluids has a linear slope within each cell having a volume fraction greater than zero and less than one; this linear shape is then used for the calculation of the advection of fluid through the cell faces. A faithful determination of the interface normal vector is a critical step in the PLIC method, since it determines the slope of the interface as well as the fluid volume matching the given volume fraction for the cell.

In performing a time-dependent VOF calculation using an explicit scheme, the time step used for the volume fraction calculation is not necessarily the same as the time step used for the rest of the transport equations. A dimensionless Courant number, *Co*, is introduced which compares the time step in a calculation to the characteristic time of transit of a fluid element across a control volume.

$$Co = \frac{u_{fluid}\Delta t}{\Delta x_{cell}} \tag{4.14}$$

The Courant number is a measure of the transport distance crossed over a time step as a fraction of the local length scale of the cell.

For instance, a Courant number 0.2 in a VOF computation would enforce a time step that allows the fluid or the interface to cross up to 20 percent of the width of a cell during each time-step, regardless of the actual velocity or cell dimension [94]. In order to minimize calculation time while ensuring stability, the Courant number must formally satisfy only $Co < 1$. However, in practice, values as low as 0.1 are often required. The length of the next time step is calculated based on a fixed local Courant number in the cells. The smallest time step is used as the characteristic time, which represents the maximum velocity found in a given group of cells. Therefore, the time step size for a

group of cells will be restricted to ensure that the free surface crosses less than a cell during that time step.

The VOF free surface module in CFD-ACE+ provides several additional features for solver control to remove tiny unphysical isolated droplets of liquid in gas region or tiny isolated gas bubbles in liquid region [94]. These droplets and bubbles are collectively called flotsam and jetsam, and are due to inadequate convergence, improper Currant number or excessive skewness in the grid. Though, this can be minimized with the PLIC reconstruction, it cannot be avoided entirely. Another feature of CFD-ACE+ is the dynamic contact angle numerical implementation that can be achieved as an option by simply introducing an user define function rather than having to implement this through an user define subroutines in FLUENT.

4.2. Implementation of Dynamic Contact Angle

In the VOF method, a description of the contact angle is essential. The contact angle at each location represents an interface or a boundary between a solid and a fluid zone. A fixed value static contact angle (SCA, θ_s) provides the simplest option. The value is often pre-specified and remains unchanged regardless of changes in the flow or other conditions. This is a suitable option if a quasi-steady or equilibrium solution is being considered. In the absence of knowledge about the variation of the contact angle with the flow or other conditions, applying the static value is the most expedient, but not necessarily accurate approach. In the present study, however, the droplet emergence phenomenon in the cathode gas channel is rarely quasi-steady. Instead, droplets emerge randomly from the rough surface of the gas diffusion layer and interact dynamically with the gas stream. Hence, treatments of dynamic contact angle using two different modeling tools, CFD-ACE+ and FLUENT, are discussed in the following sections. The first model is based in an empirical determination of the dynamic contact angle determined from the experiments in the preceding Chapter. The second model is based in the theoretical framework and Hoffman function discussed in Section 2.5.5.

4.2.1. CFD-ACE+

The dynamical dependence of the contact angle on the local tangential speed of the liquid-gas interface is important and is often specified based on empirical observations. The dependence of the contact angle on the local gas flow velocity enables the simulation of dynamic contact angle (DCA) effects, which are manifested by a difference in the contact angle for the receding and advancing contact lines. Generally, the contact angle varies continuously as the motion of the contact line changes from a receding to an advancing pattern. This variation can be approximated by a contact angle function. The variation in the contact angle with the velocity can be appreciable, and the required functional dependence is obtained herein by curve fitting the experimental data. In this section, two different methods are proposed to derive the velocity dependent contact angle function; these are then implemented in the free surface module of CFD-ACE+. The module provides options in the solver to activate the input of empirical dynamic contact angle relations. The general form of such relations is:

$$\theta_d = f\left(\theta_s, \bar{v}_t, \bar{x}, s\left(\bar{v}_t\right), \theta_{lc}, \theta_{uc}\right) \tag{4.15}$$

$$s\left(\bar{v}_t\right) = \begin{Bmatrix} \left|\bar{v}_t\right|, if\ \bar{v}_t \cdot \nabla F < 0 \\ -\left|\bar{v}_t\right|, if\ \bar{v}_t \cdot \nabla F > 0 \end{Bmatrix} \tag{4.16}$$

where

θ_d: dynamic contact angle

θ_s: static contact angle

$\bar{x}$: location on boundary surface

$\bar{v}_t$: tangential velocity at solid boundary

$\left|\bar{v}_t\right|$: magnitude of $\bar{v}_t$

$s\left(\bar{v}_t\right)$: sign magnitude of $\left|\bar{v}_t\right|$

θ_{lc}: lower cut off angle

θ_{uc}: upper cut off angle

∇F : gradient of volume fraction.

Several function forms are available in the module, such as single ramp, double ramp, quadratic, cubic, hyperbolic tangent function, etc. The selection of the function and associated parameters has to be made such that the contact angle function remains bounded and smooth since the velocity might depart from the anticipated range especially in the convergence process. Therefore, a lower contact angle cut-off of zero and upper cut-off of 180 degrees is prescribed [94].

4.2.1.1. Method 1: derivation from droplet emergence experiment

The measurements of DCA and corresponding experimental conditions were described in Chapter 3. The derivation of the velocity dependent contact angle function is based on the water injection velocity (V_w) at 0.04 m/s and air flow velocity (V_a) at 10m/s (as listed as the Case 2 condition in Table 3.1). To obtain the velocity dependent contact angle function during the period of one emergence cycle, i.e. from the onset of droplet emergence into the air stream to the time just before it detaches from the water injection pore. A snapshot of the droplet illustrates the associated parameters in Figure 4.1.

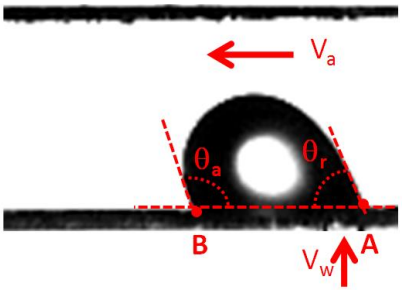

Figure 4.1. Image of water droplet subjected to the air flow stream. Points A and B are the receding and advancing points in a 2-D plane of view, whereas θ_r and θ_a designate the receding and advancing contact angle, respectively.

When a droplet emerges into the air stream, it will pin temporarily at receding point A, however, the advancing point B will keep moving toward the channel outlet along the surface until the droplet reaches a certain size, after which, it detaches and starts moving along the surface. Details of the DCA evolution through an emergence cycle were presented in Section 3.2.4. The relative motion of advancing point B is characterized as a moving contact line. It should be noted that the experimental analysis are based on 2D images, whereas the contact line of a droplet moves in a plane orthogonal to the image.

Between the advancing leading edge and the receding trailing edge, it is assumed that the contact line is connected in the same manner as the contact line velocity. Coordinates of point B relative to point A as well as the contact angle distribution in one emerging cycle in the time-series images are analyzed and presented in Figure 4.2.

To specify the dependence of the contact angle on the contact line velocity of a liquid-gas interface along the local surface, the position data were fitted to a second order polynomial function; the first derivative of this function was used to obtain the contact line velocity function.

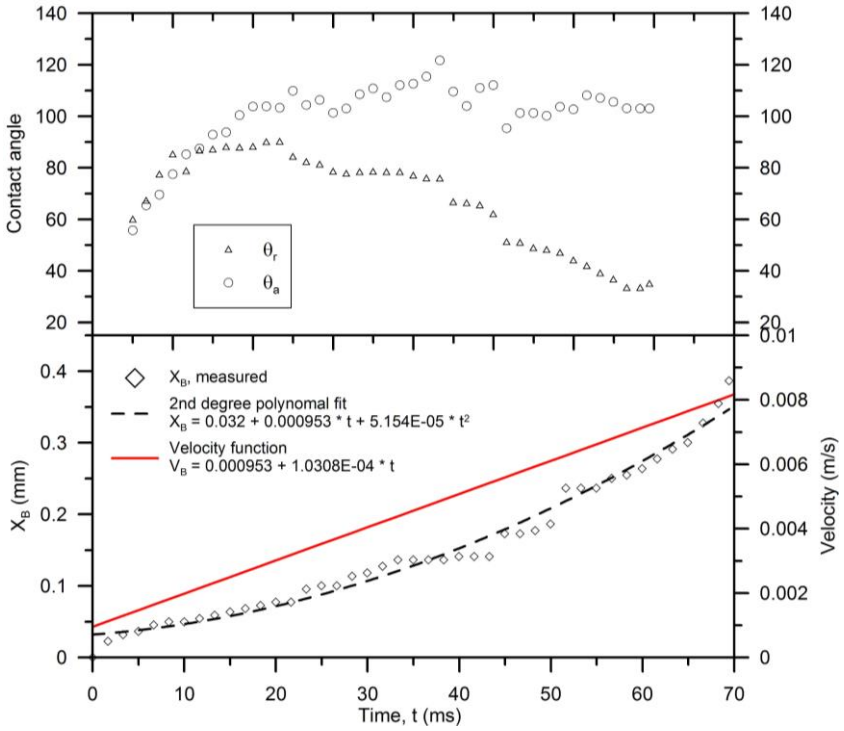

Figure 4.2. Position of advancing point (X_B), velocity function and DCA distribution for droplet emergence cycle Case 2.

The contact line advancing velocity, V_c, varies from about 0.001 m/s to 0.008 m/s (where the droplet starts to detach). Plots of the positions and advancing velocity versus time and the corresponding advancing contact angle are shown in Figure 4.3. The final form of the velocity dependent contact angle function is deduced as a single ramp function:

$$\theta_D = 25552 \cdot V_c + 25 \tag{4.17}$$

It should be noted that the data and connection are somewhat ambiguous during the initial emergence when the contact line is influenced by two surfaces: the pore surface and the channel surface which are normal to each other. This occurs when the droplet just enters the air channel and has to overcome the air stream pressure in the channel. The droplet has to move from one quasi equilibrium position to the other and must overcome the energy barrier between the interface of droplet and surface. An external disturbance or a sudden change of equilibrium condition can affect the contact angle on a rough surface [95].

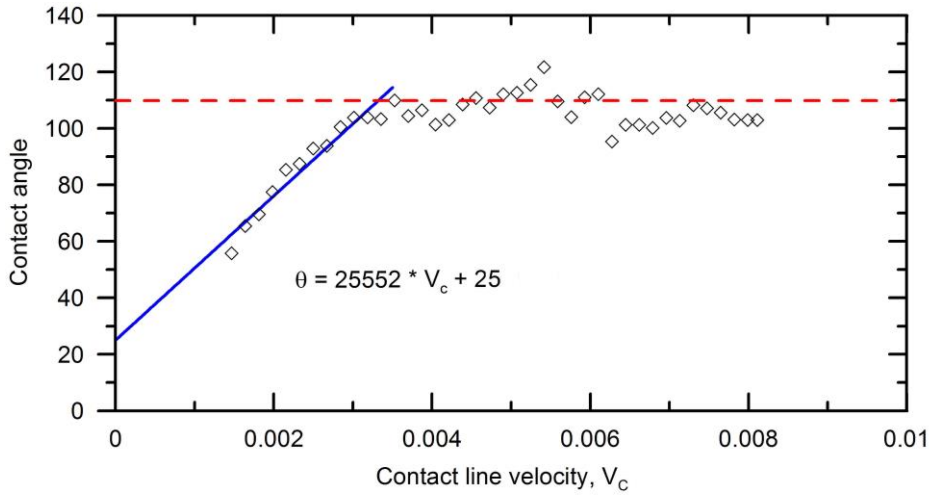

Figure 4.3. Velocity dependent contact angle function from droplet emergence experiment.

4.2.1.2. Method 2: derivation from capillary rise experiment

A cross sectional dimension of 250 µm square of PDMS microchannel was fed with water from one side, with the other side open to atmosphere. The PDMS chip was placed on the same experimental platform as described in Chapter 3. Water was pumped from one side to the other, and the evolution of the shape of the water meniscus and of the advancing contact angle was observed over a range of pumping velocities. Similarly, the receding contact angle was observed and measured by sucking the water back into the syringe pump as illustrated schematically in Figure 4.4.

Figure 4.4. Schematic diagram of capillary rise experiment.

The flow images were analyzed using contact angle measurement. For each run of this experiment, there is only one contact angle and only one velocity. This experiment provides a more accurate measurement for advancing and receding angles. The pumping flow rate provides the advancing data with positive velocity, and the withdrawing flow rate provides the receding data with negative velocity. The resulting velocity dependent contact angle function is presented in Figure 4.5. The data obtained with the first method are also plotted for comparison.

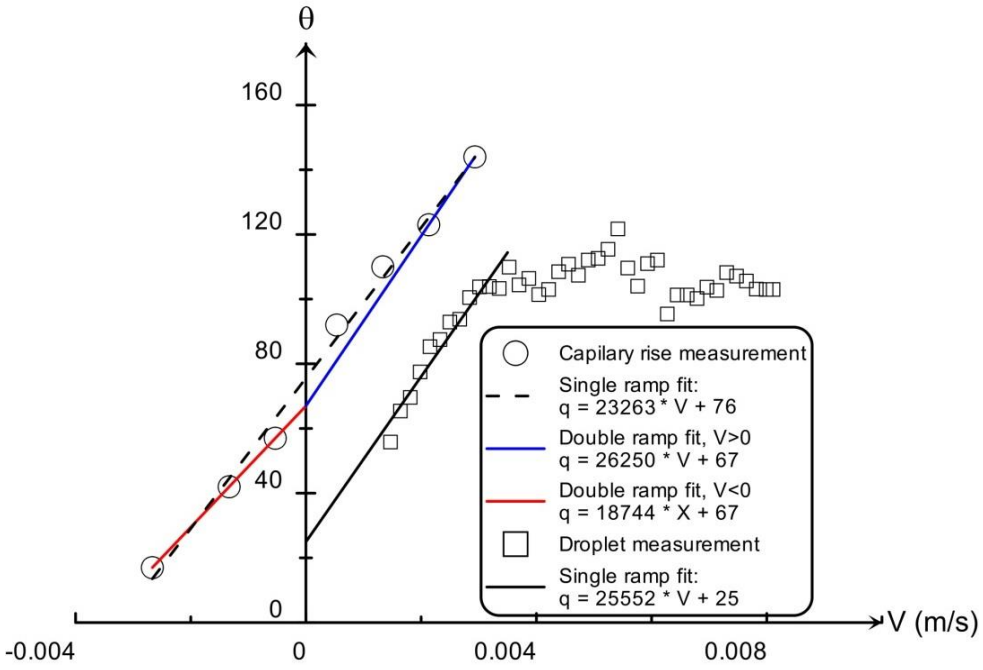

Figure 4.5. Velocity dependent contact angle function.

The two different curve fitted functions, single and double ramp, were implemented as the input parameters for the VOF free surface module of CFD-ACE+ using the dynamic contact angle option. The final forms of the velocity dependent contact angle functions for the single and double ramp cases, are:

$$\text{single ramp}: \theta_D = 23263 \cdot V_c + 76 \tag{4.18}$$

$$\text{double ramp}: \begin{cases} \theta_D = 26250 \cdot V_c + 67 & for\, V_c > 0 \\ \theta_D = 18744 \cdot V_c + 67 & for\, V_c < 0 \end{cases} \tag{4.19}$$

The double ramp function allows representation of the change in slope for the advancing and receding contact angle. Since prior to detachment, the velocity is close to zero and therefore the contact angle corresponds closely to the intercept angle (67°) in the curve, the specification of the intercept angle might affect the emergence phenomena slightly in the simulations.

4.2.2. ANSYS FLUENT

Using user defined function (UDF) in FLUENT, the Hoffman function (cf. Eq.(2.11)) is implemented in two different steps in subroutines written in C code [51]. The first step is to determine the unit normal for the phase boundary. The second step is to provide the main program with a local contact angle by determining the local capillary number and evaluating the Hoffman function. Details of the source code are listed in Appendix C.

In the step of determining the unit normal, the gradients and other phase information is released from memory after the calculation of the phase composition. A dummy source term (DEFINE_SOURCE) is reserved to exchange the information for evaluating the VOF equations together with the associated data. The solver will call this dummy source term code every time the VOF equations are solved. An additional function (DEFINE_ADJUST) is also required to setup the system variables and allocate a memory buffer to store the related information. When the dummy source term code is called, it collects the phase gradients (C_VOF_G) for the boundary, and stores them in a user defined function (C_UDMI). The code then returns a source term of zero to the equations. This is a key step to enable the VOF gradient data to be accessible by the main contact angle code specifically when the boundary conditions are imposed.

The second step involves the evaluation of local contact angle through the UDF (DEFINE_PROFILE) to determine the Hoffman function which has the form of:

$$\theta_D = f_{Hoff}[Ca + f_{Hoff}^{-1}(\theta_e)] \tag{4.20}$$

The inverse Hoffman function needs to be evaluated based on the static contact angle through a zero finding function. The main code obtains the phase gradients (C_VOF_G) from the UDF which was saved in the first step. The phase gradients are then brought into the code and normalized. The contact line velocity can then be determined by taking the dot product of flow field velocity (C_U, C_V, C_W) for the mixture with the normalized unit vector along the direction of the interface normal vector (NV_DOT). The capillary number is then determined by this velocity normal and the Hoffman function is evaluated. Finally, the dynamic contact angle is returned to the main program at each location and the next iteration starts.

4.3. Simulation Domain and Mesh, Boundary and Initial Conditions

4.3.1. CFD-ACE+

A schematic of the three dimensional computational domain and the corresponding mesh is shown in Figure 4.6.

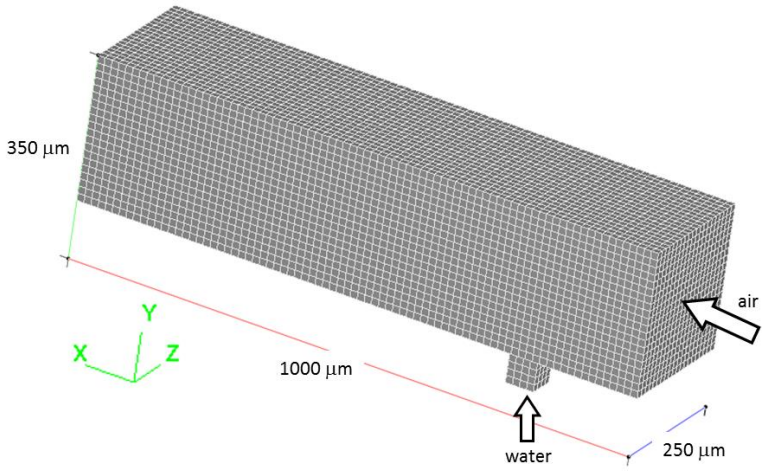

Figure 4.6. Three-dimensional domain and mesh for the numerical simulations of droplet emergence using CFD-ACE+.

The domain consists of a 3-D geometry with square air and water channels of width 250 µm and 50 µm, respectively. These dimensions are identical to those in the experimental

setup up described in Chapter 3, except for the channel length used in numerical simulation is 1,000 μm. While this is shorter than in the experiments to reduce computational costs, the simulations still cover the flow region of interest. Uniform mesh interval 12.5 μm (32,128 cells) and 6.25 μm (257,024 cells) were used. The uniform velocity profiles are specified at the channel air inlet and water inlet. A convective outflow condition is used at the channel outlet. Air flow enters the channel from the right-hand side at a velocity U = 10 m/s, pressure of 101.3 kPa and temperature of 298K. The water is injected into the channel with a velocity of V = 0.04 m/s through the pore located on the midline of bottom surface (cf. Case 2 condition in Table 3.1). A no-slip boundary condition is applied on all of the surfaces. Surface tension and contact angle are specified on the wall as the boundary condition. The simulations are initialized with a uniform air velocity field and no liquid water present in the channel. For the base case study, a static contact angle (SCA), $\theta_s = 110°$, is specified on all the surfaces; this coincides with the experimental conditions in Chapter 3 which a microchannel using PDMS (Polydimethylsiloxane) material. For the dynamic contact angle (DCA) simulation, a velocity dependent contact angle function (discussed in Section 4.2.1) is specified. To minimize the computation time without interfering with stability, the size of the next time step Δt was computed before every new time step based on fixed Courant number (*Co* = 0.2) and the variable local velocity in the cells. Thus the largest velocity in the domain determines the maximum time step. The resulting time step was of the order of 10^{-8} s ~ 10^{-7} s. For the geometric reconstruction of the interfaces between water droplets and air, a PLIC (piecewise linear interface calculation) method was used in conjunction with Gauss's theorem.

4.3.2. ANSYS FLUENT

Two different simulation conditions are discussed herein. The first addresses model validation for the dynamic contact angle formulation using droplet impact on a horizontal surface. The second one describes the condition for droplet emergence simulation used for dynamic contact angle modeling.

4.3.2.1. Droplet impact

The numerical code for dynamic contact angle is first validated using a well-established two phase flow study before application to the droplet emergence simulation. The droplet impact on a horizontal surface selected as a “benchmark” case is well discussed in the literature and exhibits spreading and recoiling phenomenon that correspond to advancing and receding contact lines [43]. Though a three dimensional model is the best to predict the entire droplet impact process, it was shown that a two dimensional axisymmetric simulation can represent the process faithfully [43].

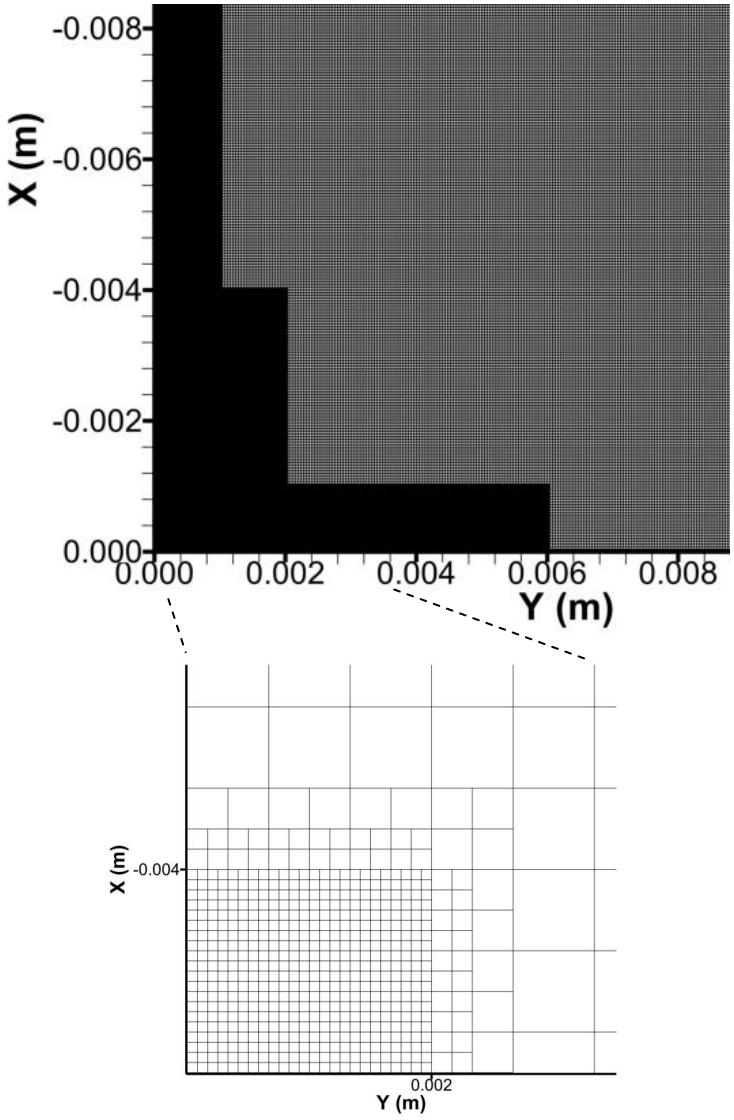

Figure 4.7. Illustration of numerical grids used for the droplet impact computations. The region of an adaptive refinement is presented.

Thus, a two dimensional axisymmetric simulation is used in this study where the changes in azimuthal direction are not considered for a droplet normal impact on a horizontal wax surface. The computational domain consists a two dimensional plan of 12 × 12 mm large square in x-y plane as shown in Figure 4.7 where a single free falling droplet along the x-direction impacts a plane in the y-direction. The largest uniform mesh interval is 40 μm away from the boundary. Further mesh refinement using adaptive grid is applied to the near wall boundary as well as the center line (cf. black region in Figure 4.7) where the major liquid droplet movement occurs. The mesh refinement is critical in order to capture the particular details of lamella motion near the wall boundary. The finest cell near the wall is 2.5 × 2.5 μm. The total number of cells used in this case is 597,447.

Water is used as the test liquid and encounters a normal impact on a horizontal waxed surface. The static contact angle for water on the wax is in the range of 95° - 105°, therefore 105° is used for the SCA case study. Flow conditions and fluid properties are summarized in Table 4.1. The water droplet size D is 2.7 mm and the impact Webber number *We* is 90, equivalent to an impact velocity of 1.57 m/s along the *x* direction in Figure 4.7. The droplet is initialized at the instant of impact using the FLUENT UDF code for initialization which is listed in Appendix D.

Table 4.1. Properties of liquid and flow conditions.

Liquid	σ (N/m)	μ (Ns/m^2)	ρ (kg/m^3)	D (mm)	*We*	V (m/s)	*Re*	θ_s
Water	0.0728	0.001	998.3	2.7	90	1.57	4223	105

Where σ is surface tension, μ is dynamic viscosity, ρ is density, D is droplet diameter before impact, V is impact velocity, Re is impact Reynolds number and θ_s is the static contact angle.

A variable time step is applied by controlling the Courant number, *Co* = 0.25, as a result the time step is of the order of 10^{-6} s for SCA and 10^{-8} s DCA modeling. The introduction

of the DCA model makes the numerical convergence process much slower and necessitates variable time steps that are typically two orders of magnitude lower.

4.3.2.2. Droplet emergence

Figure 4.8 presents the three dimensional computational domain and corresponding mesh for droplet emergence modeling. The width of the square air and water channels is 250 µm and 50 µm, respectively, and is described in Section 4.3.1.

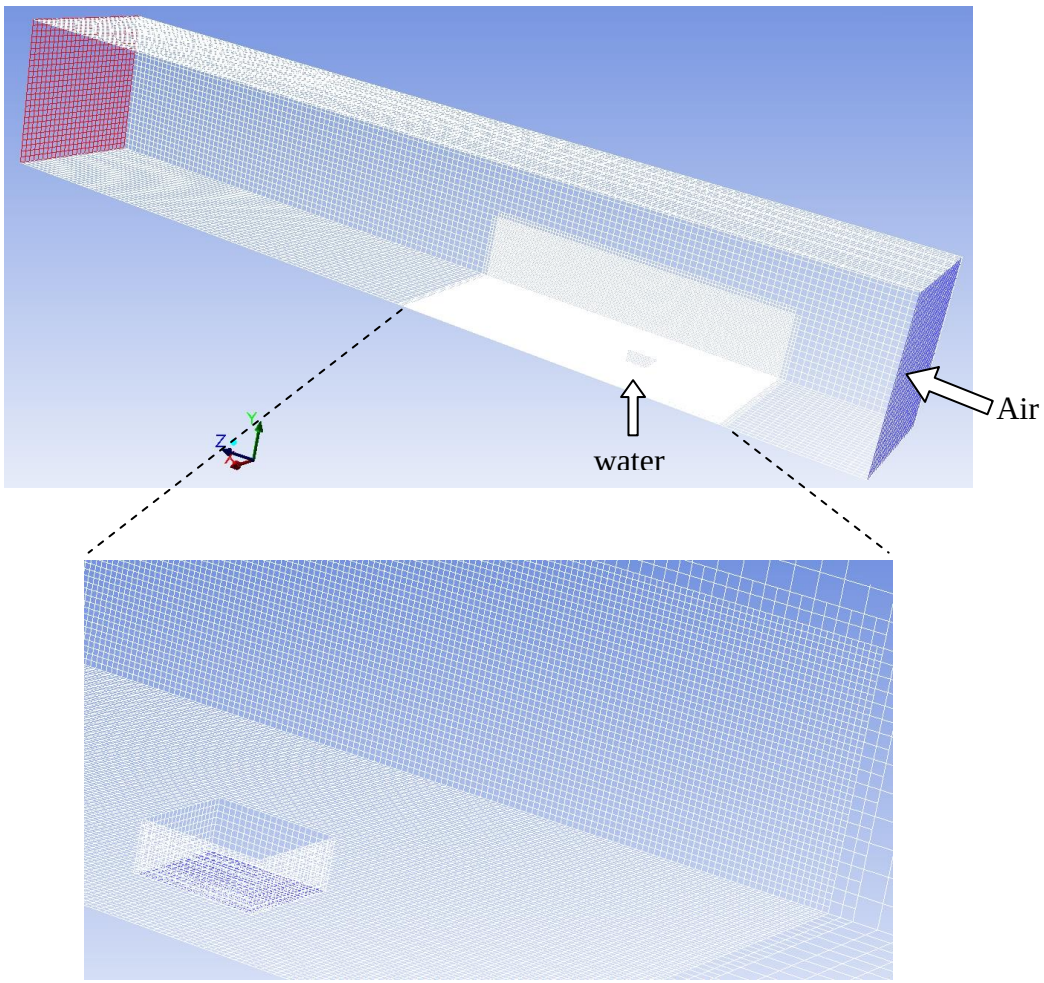

Figure 4.8. Computation domain and mesh illustration for the droplet emergence study, presenting the region of an adaptive refinement.

These dimensions are identical to the experimental ones described in Chapter 3, except for the channel length of 1,500 µm used in numerical simulation. Flow conditions of air and water inlet velocities are 10 m/s and 0.04 m/s, respectively. These conditions are the same in the case 2 condition in Table 3.1. A uniform mesh interval of 10 µm is used

throughout the domain, except for the near-pore subdomain which is further refined. To enhance the accuracy of the simulations and fully resolve the dynamic droplet emergence and detachment, adaptive gridding was used to refine the mesh in the near pore region and corresponding boundaries (cf. zoom-in region in Figure 4.8). The size of the adaptive refinement region is adjusted to cover one emerging droplet in order to capture the contact line movement. The finest cell near the wall is 2.5 × 2.5 × 2.5 μm. The total number of cells used in this case is 896,700. A factor of 0.5 for under-relaxation is applied for the pressure based solver control. The adaptive refinement and relaxation factor play a key role for the droplet emergence simulation. Variable time step is applied by setting the Courant number, Co = 0.25, as a result the time step is of the order of 10^{-7} ~ 10^{-6} s for SCA modeling and 10^{-9} ~ 10^{-8} s for DCA modeling.

4.4. Results and Discussions

4.4.1. CFD-ACE+

4.4.1.1. Static contact angle (SCA): base case

The base case using SCA is first presented at the instant in time when the droplet detaches (Figure 4.9).

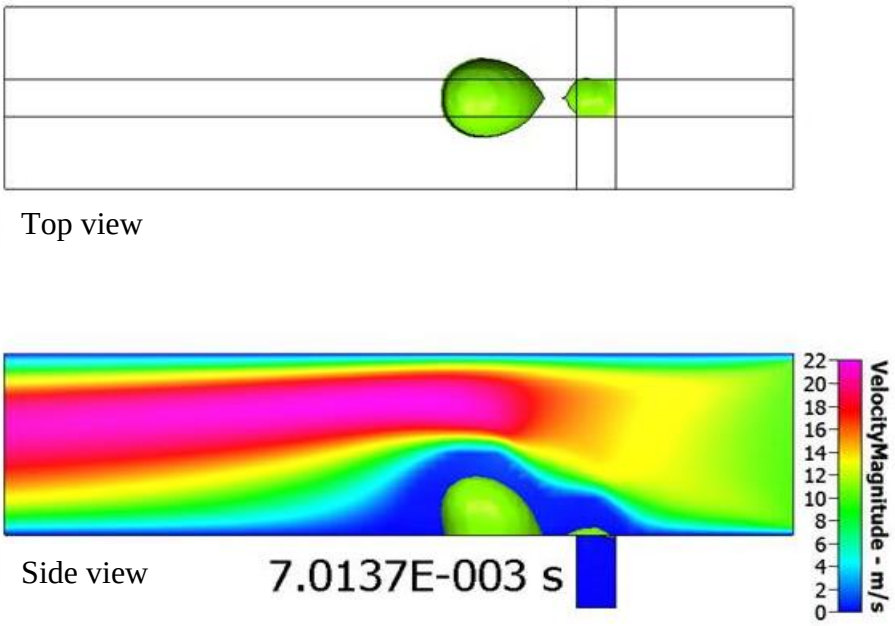

Figure 4.9. (a) Top view. (b) Side view of the instant at droplet detachment using SCA.

Examination of the animation sequence shows that each individual droplet emerging from the water pore remains pinned around the pore due to surface tension forces until it grows into a critical size before detaches from the pore. The effect of air velocity on the changing shape of the emerging droplet and the time evolution of the emerging process can be observed. The periodic emerging frequency is around 142.6 Hz (T = 7.0137 ms). Images at different instants are analyzed to evaluate the advancing and receding contact angles and further compared with the experimental results presented in Chapter 3. The droplet shape at detachment differs significantly from the shape observed in the

experiments. The long water trailing observed in the experiment does not present in the simulations in which instead the droplet maintains a fuller height. Deviation of dynamic contact angle evolution in an emergence cycle using normalized time scale ($\tau = t / T$) is presented in Figure 4.10.

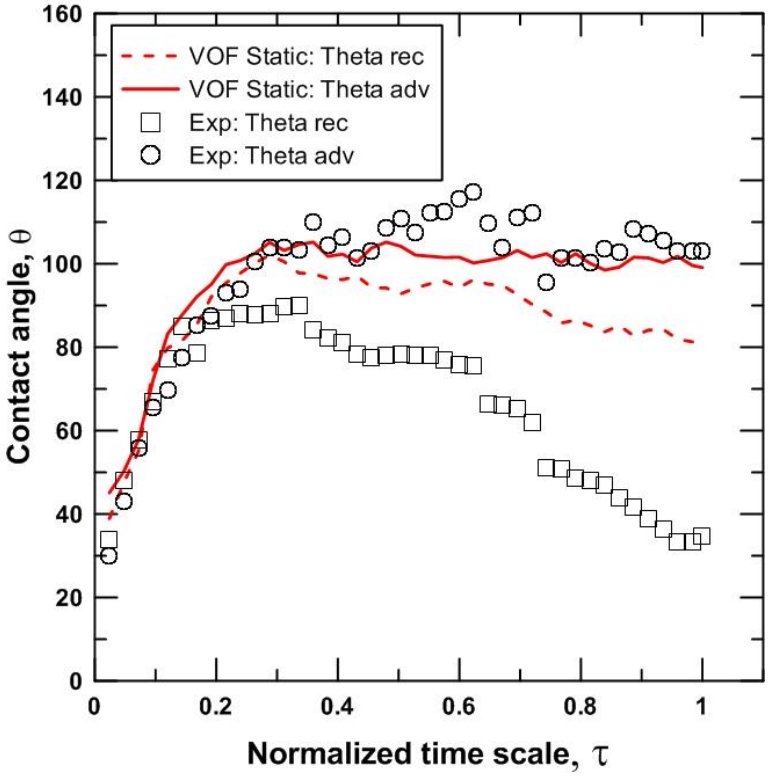

Figure 4.10. Comparison of contact angle evolution of VOF simulation (SCA, mesh 12.5um) and experiments.

While the evolution of the advancing angle is reproduced reasonably by the simulation, the static angle formulation results in there significant discrepancy between the simulation and experimental receding angles. Additionally, a smoother evolution rather than the stick and jump motion that is observed in the experiment. This highlights the effect of surface roughness or inhomogeneities which are not taken into account in this study. It's worth noting that the droplet emergence is around 10.8 times faster than that of the experimental results (142.6 Hz versus 13.2 Hz), and the simulation droplets are smaller than observed in the experiment immediately after detachment.

4.4.1.2. Dynamic contact angle (DCA): Method 1, Eq. (4.17)

DCA simulation results using Eq. (4.17) derived from the droplet emergence experiment are presented in Figure 4.11.

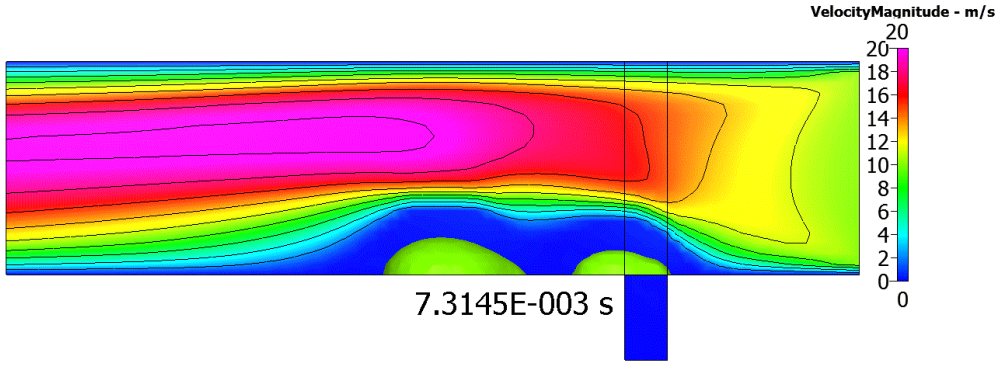

(a)

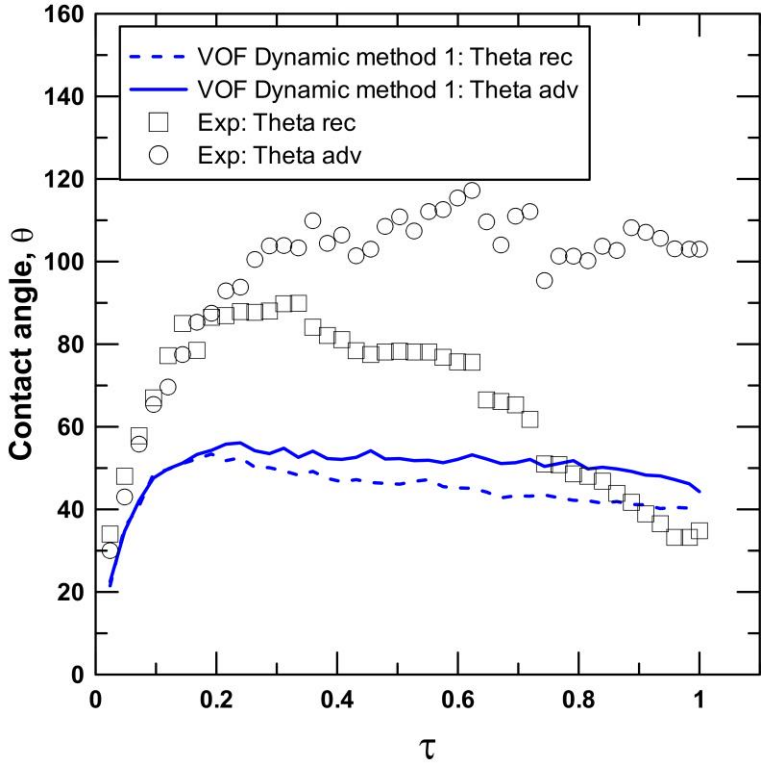

(b)

Figure 4.11. (a) Side view of the instant at droplet detachment using DCA Eq. (4.17). (b) Comparison of contact angle evolution of VOF simulation (DCA, method 1, mesh 12.5 μm) and experiment.

The simulated droplet exhibits water trailing but its shape isn't otherwise faithful to the experiment. The contact angle evolution shows a monotonic decrease before crossing over the experimental curve and over predicting the contact angle. The emergence frequency is around 137 Hz. It is shown that using method 1 for deriving the velocity dependent contact angle function Eq. (4.17) is clearly deficient for describing the contact line motion. In this method, the data is deduced from point A and point B (cf. Figure 4.1 and Figure 4.2) and thus characterize the whole droplet behavior based on only two points. Whereas, in realty, there is a different contact angle vs. velocity relation at each point of the curve defined by the intersection of the droplet surface and the bottom wall on which it moves. The contact angle at point A and B is not a function of their velocity only. There are different contact angles along the footprint and they all influence each other by deforming the droplet surface. Using a two dimensional image and axisymmetric assumption is not suitable to delineate the velocity dependent contact angle function since the effect of through plan motion is not well described. In addition, there is a window of about 17 ms (cf. Figure 3.8 Period I and II) during which data points include a surface tension dominant and transition region when the droplet is growing but held in place by the strong surface tension; this phenomenon skews the data set and the velocity. Finally, Eq. (4.17) doesn't include a negative velocity dependent contact angle relation.

4.4.1.3. Dynamic contact angle (DCA): Method 2, Eq. (4.19)

Figure 4.12 presents the results using DCA Eq. (4.19) with a uniform mesh of 12.5 μm. The droplet emergence frequency is around 114 Hz, which is slightly lower than the SCA results. An improvement of contact angle evolution is observed. Though the receding angle is still not well captured, the evolution of the advancing angle is in better agreement with the experiments. The surface tension dominates period (cf. Figure 3.8) ends around $\tau = 0.15$, however no transition period is observed. Although some of the discrepancies can be attributed to the dynamic contact angle model, detailed examination of these results also indicated that a finer mesh is required by the VOF technique to resolve the droplet dynamics, especially close to the solid surface.

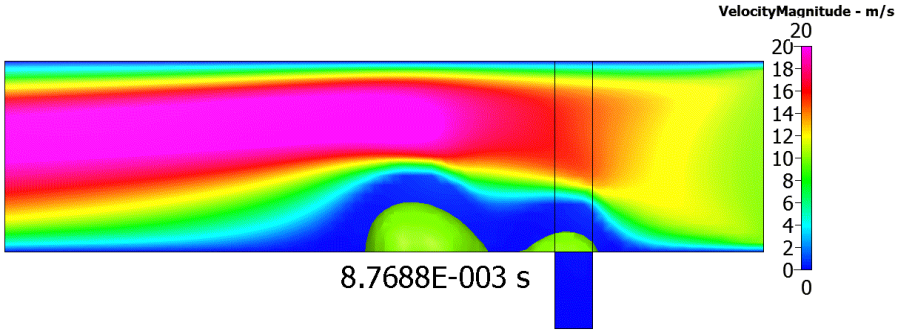

(a)

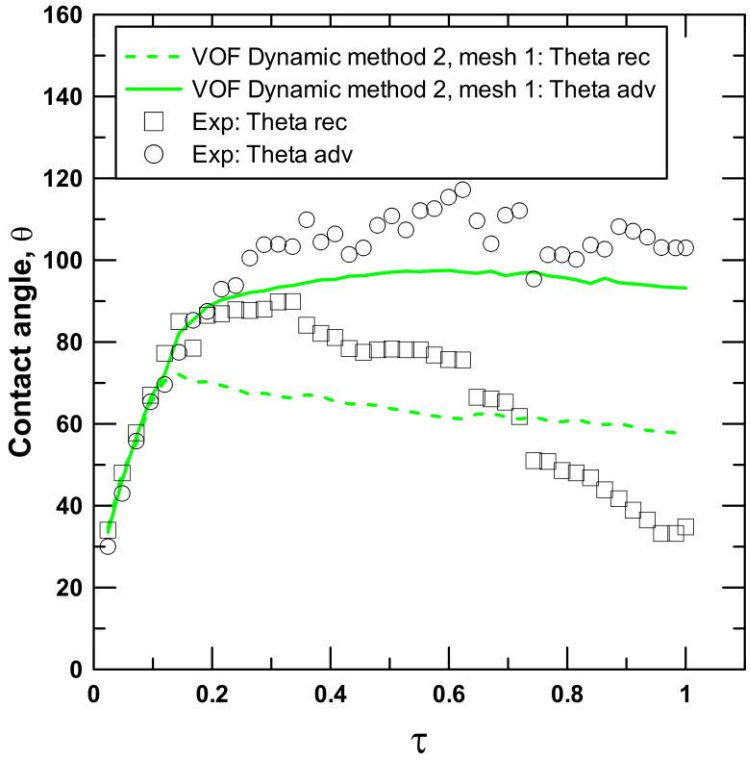

Figure 4.12. (a) Side view of the instant at droplet detachment using DCA Eq. (4.19) and [3]. (b) Comparison of contact angle evolution of VOF simulation (DCA, method 2, mesh 12.5 μm) and experiment.

Figure 4.13 presents the results using a finer 6.25 μm mesh. This mesh resolution yields a significant improvement in the droplet emergence frequency, but the value of about 70 Hz, is still five times higher than the experimental results. Although further mesh refinement might be warranted, the discrepancy is primarily attributed to the effect of surface inhomogeneities and roughness effects that are not accounted for in the simulations.

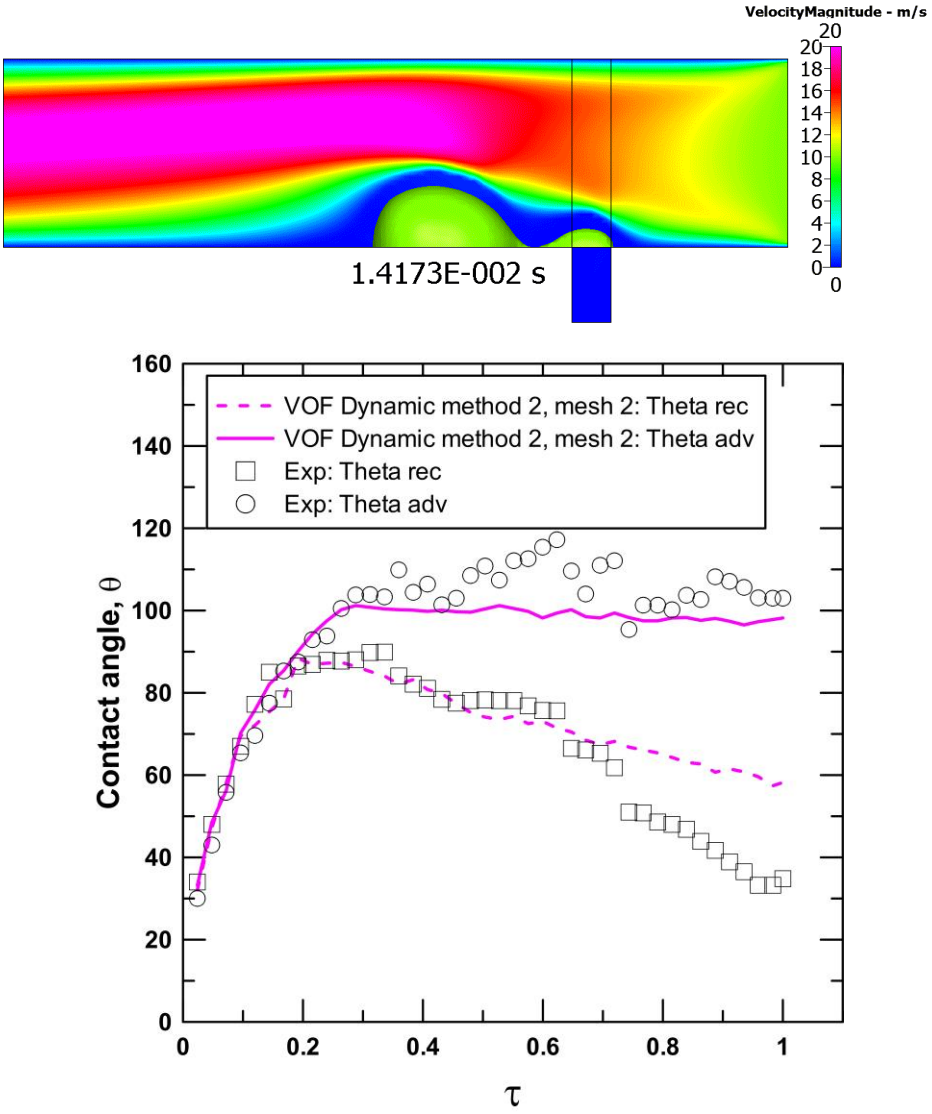

Figure 4.13. (a) Side view of the instant at droplet detachment using DCA Eq. (4.19) and [3]. (b) Comparison of contact angle evolution of VOF simulation (DCA, method 2, mesh 6.25 μm) and experiment.

4.4.2. ANSYS FLUENT

4.4.2.1. Droplet impact on a horizontal surface

Base case study using SCA under the flow condition as listed in Table 4.1 is discussed herein for the benchmark problem of a free falling droplet impacting a horizontal surface. The results are compared against the experimental and numerical results presented by Šikalo and Ganić [96] and are shown in Figure 4.14.

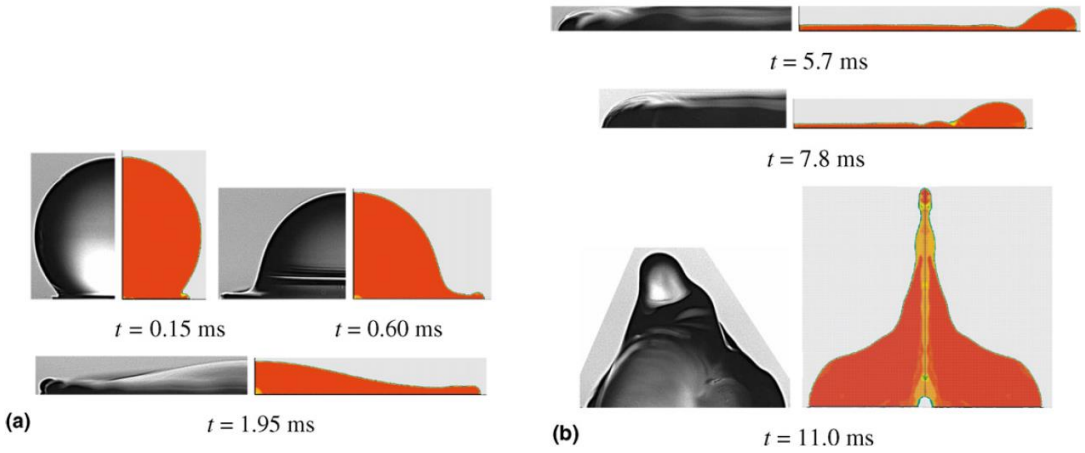

Figure 4.14. Comparison of time sequence of water droplet impact onto wax surface (*We* = 90), experiment (left) and numerical (right) (reproduced from [96] with permission of Experimental Thermal and Fluid Science).

As pointed out by Šikalo and Ganić [96], the liquid film (lamella) thickness is less than 6µm at the beginning of the impact observed from the experiment. This observation emphasizes the importance of using grid refinement at the wall boundary. It was noted that due to the depth field in the experimental images, the experimental images present some blurriness especially during the later spreading process which exhibits wrinkling on the edge due to circumferential instability. Consequently, only the sharpest image boundary should be considered when comparing with the numerical results. The image at t = 11.0 ms shows an uprising central jet in the axisymmetric simulation which azimuthal variations present in the latter phase of the experiments.

The time series images during the spreading and recoil phases using SCA model are shown in Figure 4.15 and Figure 4.16, respectively.

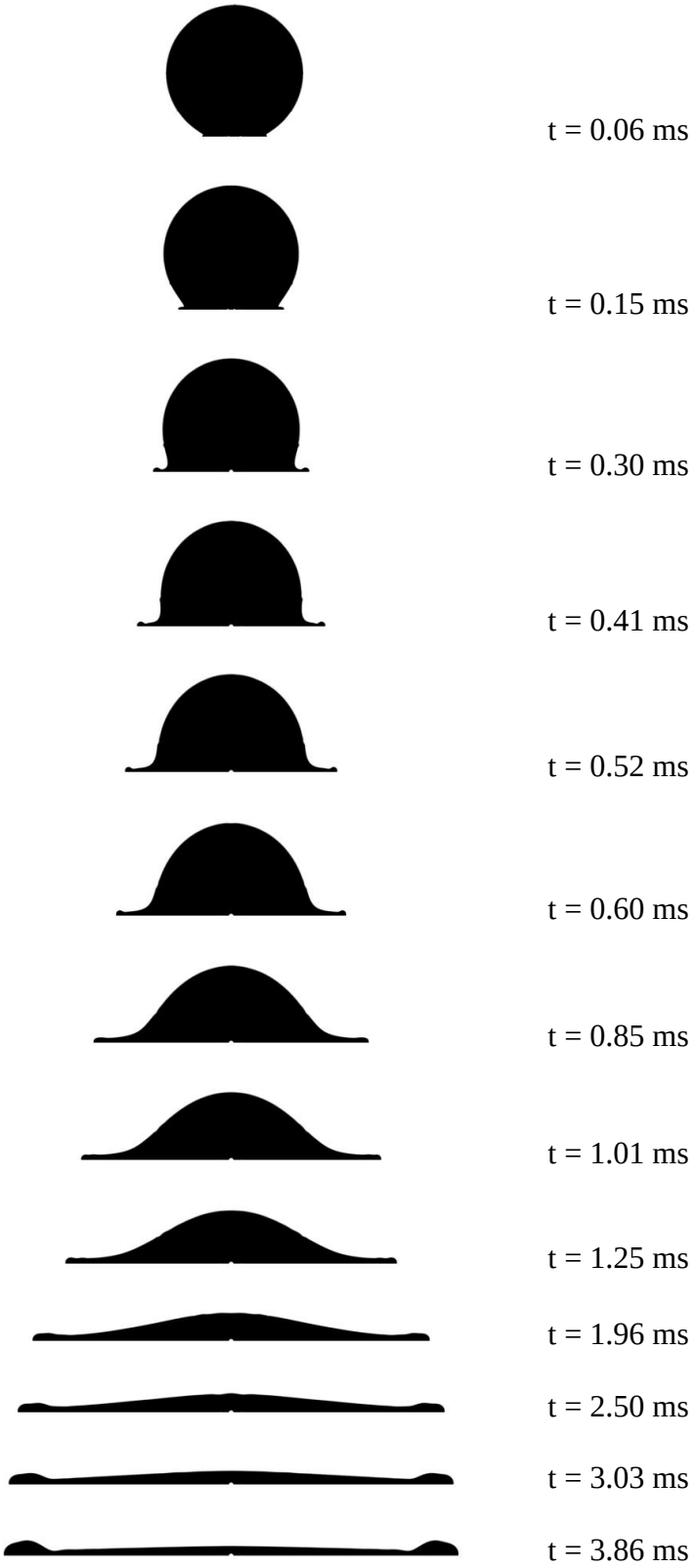

Figure 4.15. Time series images during the spreading phase for SCA modeling of droplet impact on wax surface.

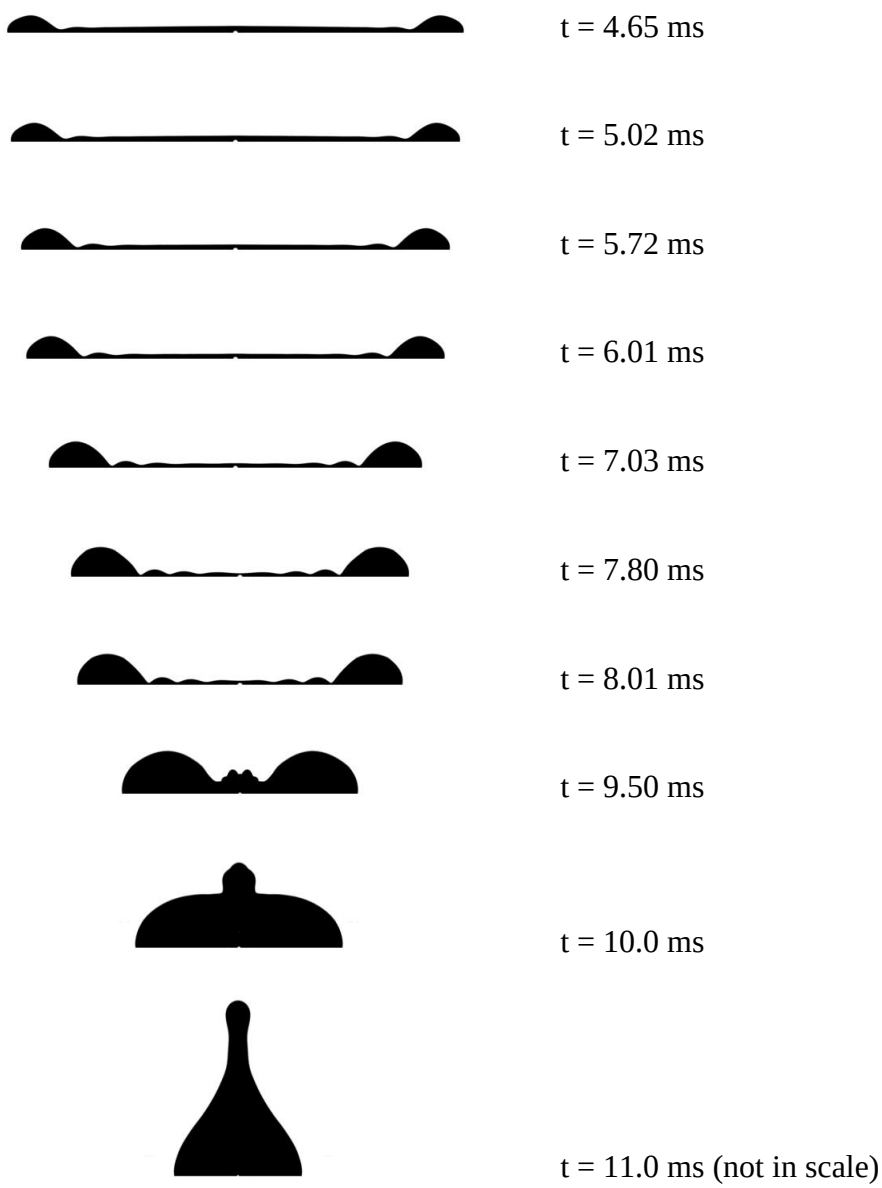

Figure 4.16. Time series images during the recoiling phase for SCA modeling of droplet impact on wax surface.

Additionally, the time series images during the spreading and recoiling phases using the DCA model are shown in Figure 4.17 and Figure 4.18, respectively.

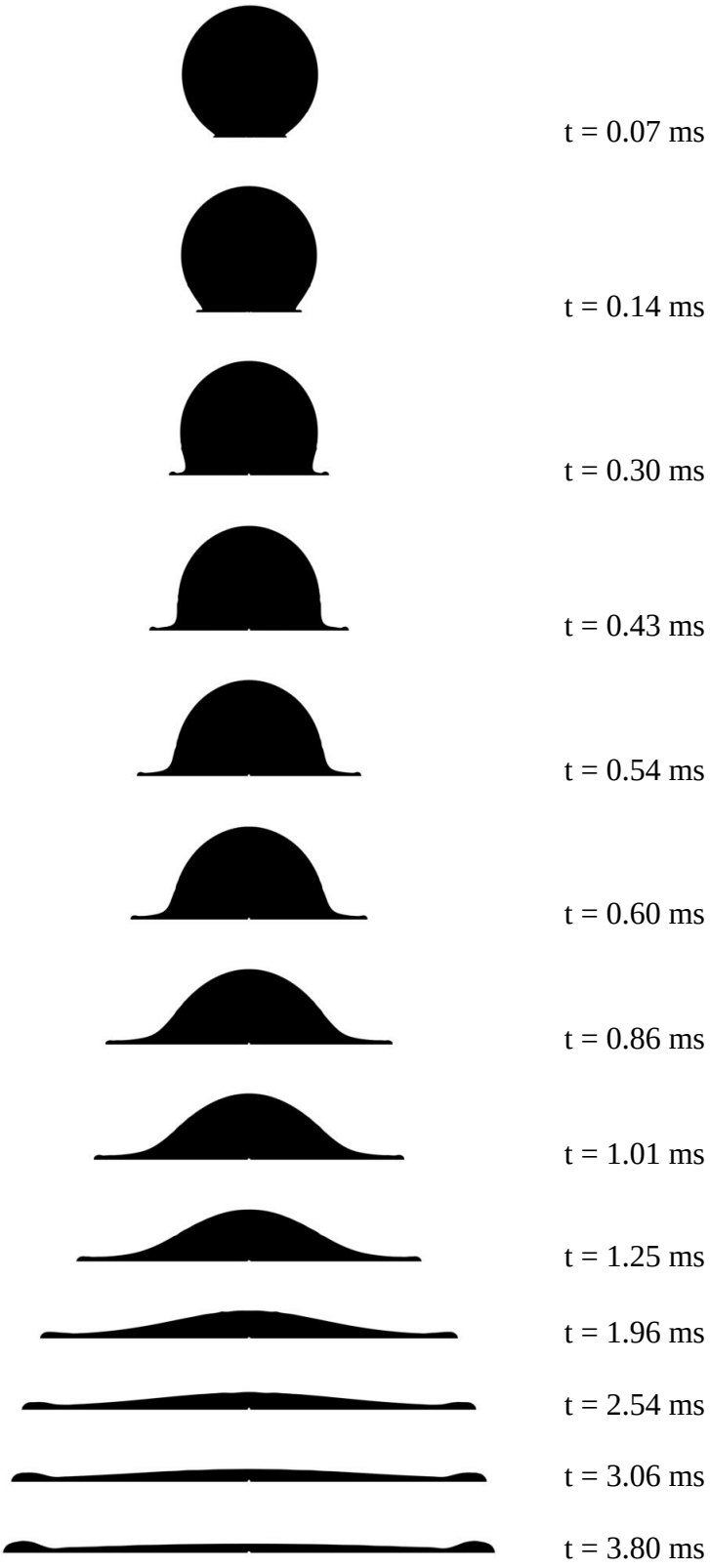

Figure 4.17. Time series images during the spreading phase for DCA modeling of droplet impact on wax surface.

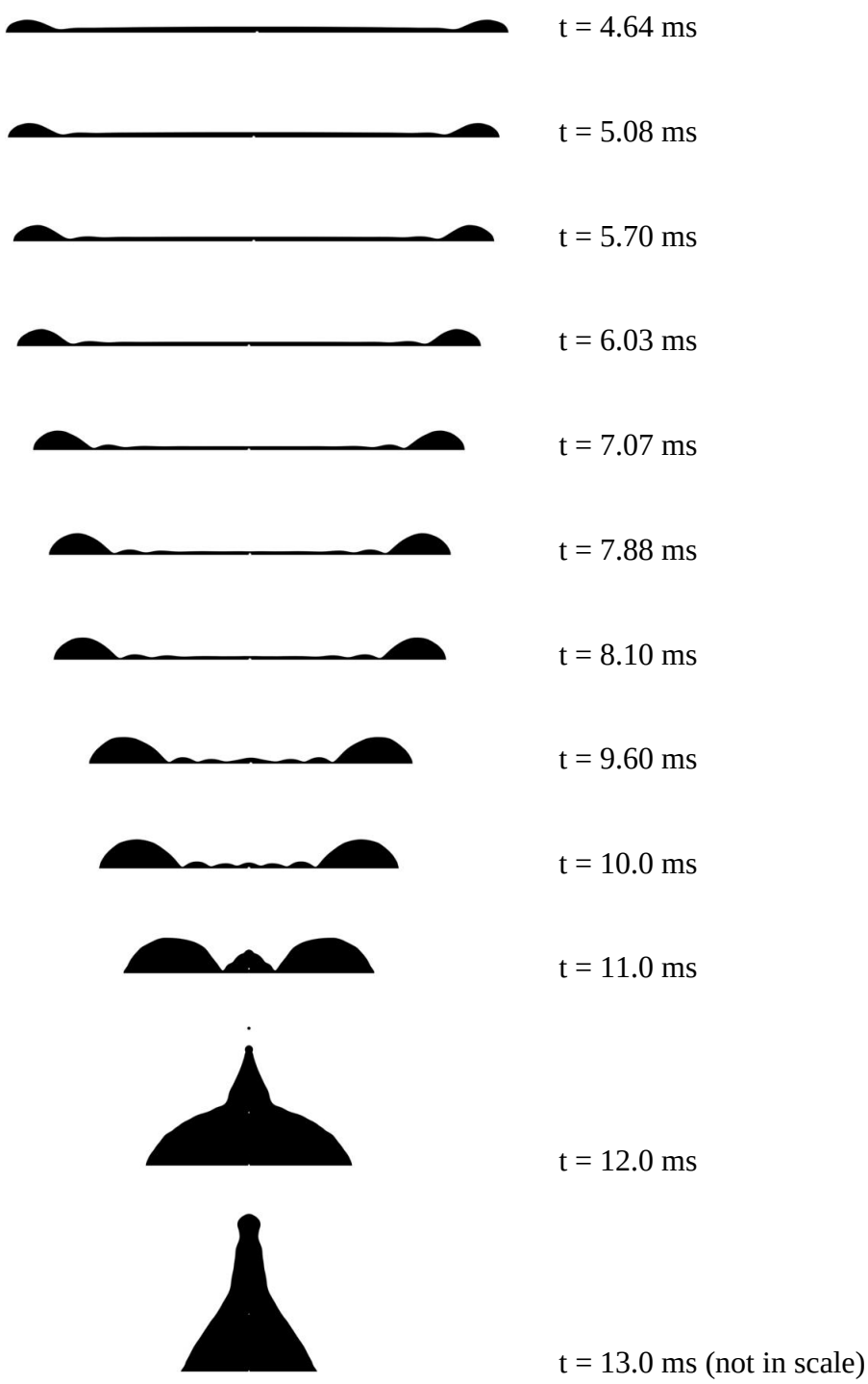

Figure 4.18. Time series images during the recoiling phase for DCA modeling of droplet impact on wax surface.

In each case, an air micro-bubble is shown near the impact point at the origin of the coordinate system due to the deformation of the droplet surface at the instant of contact. The entrapment of air bubble is numerically and experimentally observed over a wide range of impact conditions by Mehdi-Nejad et al. [97] and Thoroddsen et al. [98], respectively. The non-dimensional spreading diameter (d/D) and apex height (y/D) of a droplet, shown schematically in Figure 4.19, are quantified for further analysis as a functions of dimensionless time (tV/D) from impact.

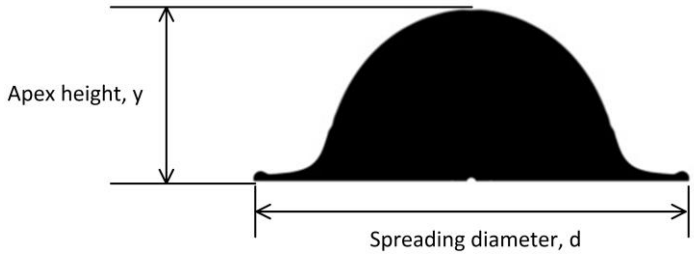

Figure 4.19. Schematics of spreading diameter and apex height of drop impacts.

The numerical are with the work of Šikalo et. al [81] for the spreading diameter are shown in Figure 4.20 for different contact angle approach.

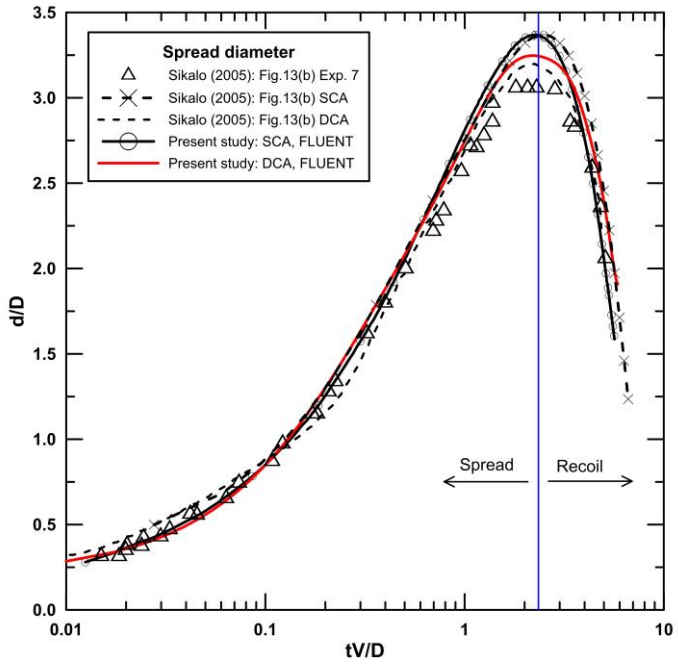

Figure 4.20. Numerical simulation of the temporal evolution of the spread diameter in comparison with the results of Sikalo et. al [81].

The present results agree with the experimental data very well in the early spreading phase when the inertial force is dominant in the early phase and the effect of wettability is relatively minor. During the later advancing phase of the spreading while close to the maximum spreading distance and the drop begins to recoil, the results of using DCA algorithm provide better evidence the ability to track the wettability effect together with the drop deformation. The maximum spreading diameter using DCA approach is about 1.2% larger than the numerical results in Šikalo et. al [81]. The simulated and experimental apex heights are also compared in Figure 4.21.

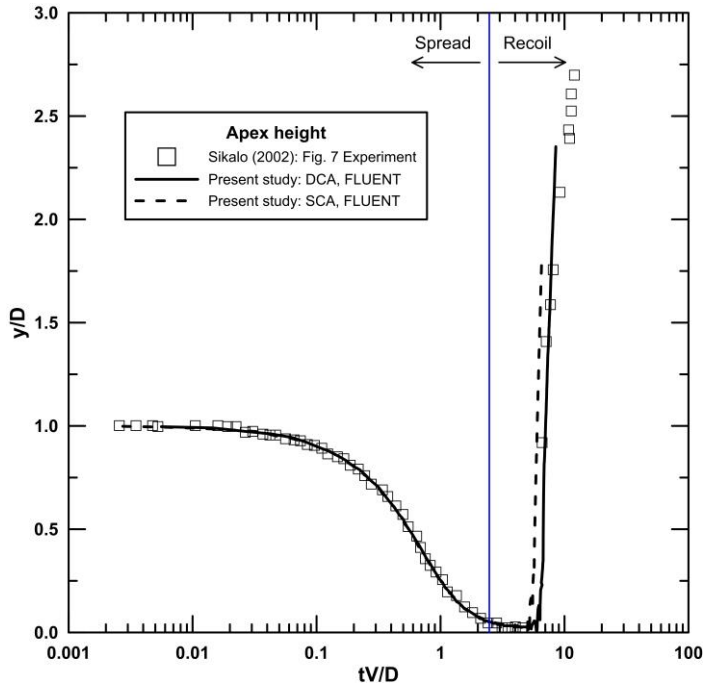

Figure 4.21. Numerical simulation of the temporal evolution of the apex height in comparison with the results of Šikalo et. al [99].

The dimensionless apex height decreases from 1, the highest value at the instant of impact, to around 0.05 in the spreading phase. There is no significant difference in the spreading phase between DCA and SCA simulations, and the results coincide with the experimental results of Šikalo et. al [99]. This is expected since the inertial force is dominant in the spreading phase until the droplet reaches the maximum spreading distance; by the time the recoil phase takes over as a viscous effect starts to play a major role. During the recoil phase, the DCA approach follows the experimental data faithfully.

4.4.2.2. Droplet emergence in a fuel cell channel

The base case for droplet emergence study is using SCA approach. Figure 4.22 shows the time evolution of the droplet in one emergence cycle.

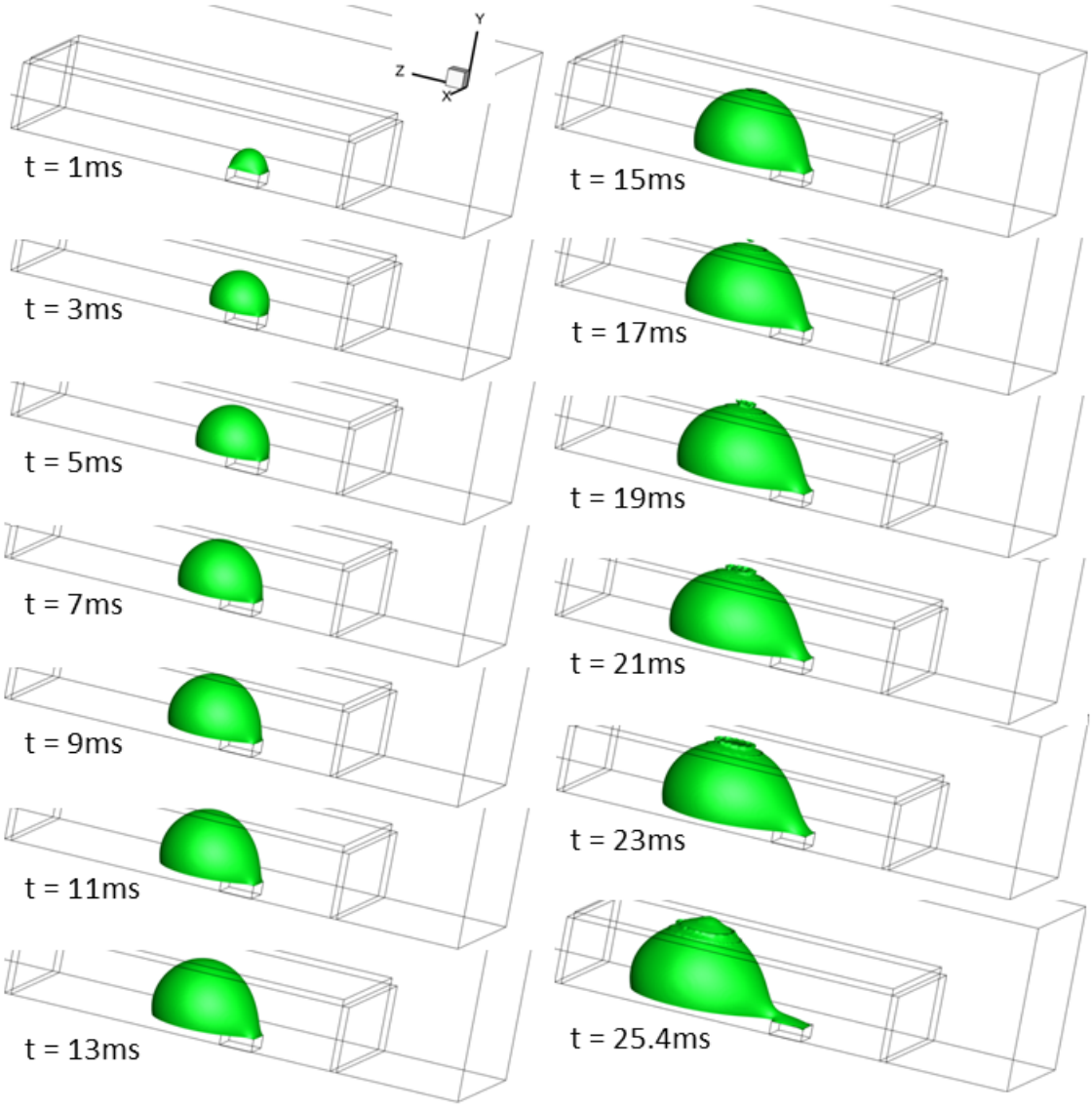

Figure 4.22. One cycle of droplet emergence time resolved images of numerical results using static contact angle (SCA, θ_s = 110°) approach in FLUENT. Air inlet velocity, V_a = 10m/s; water inlet velocity, V_w = 0.04 m/s.

The edges inside the channel delineate the near-wall grid refinement region as shown in Figure 4.8. The droplet is essentially hemispherical before 5 ms, and then tilts slightly toward the channel outlet after 7 ms. The droplet detaches from the water pore at around 25.4 ms which corresponds to a shedding frequency of 39 Hz.

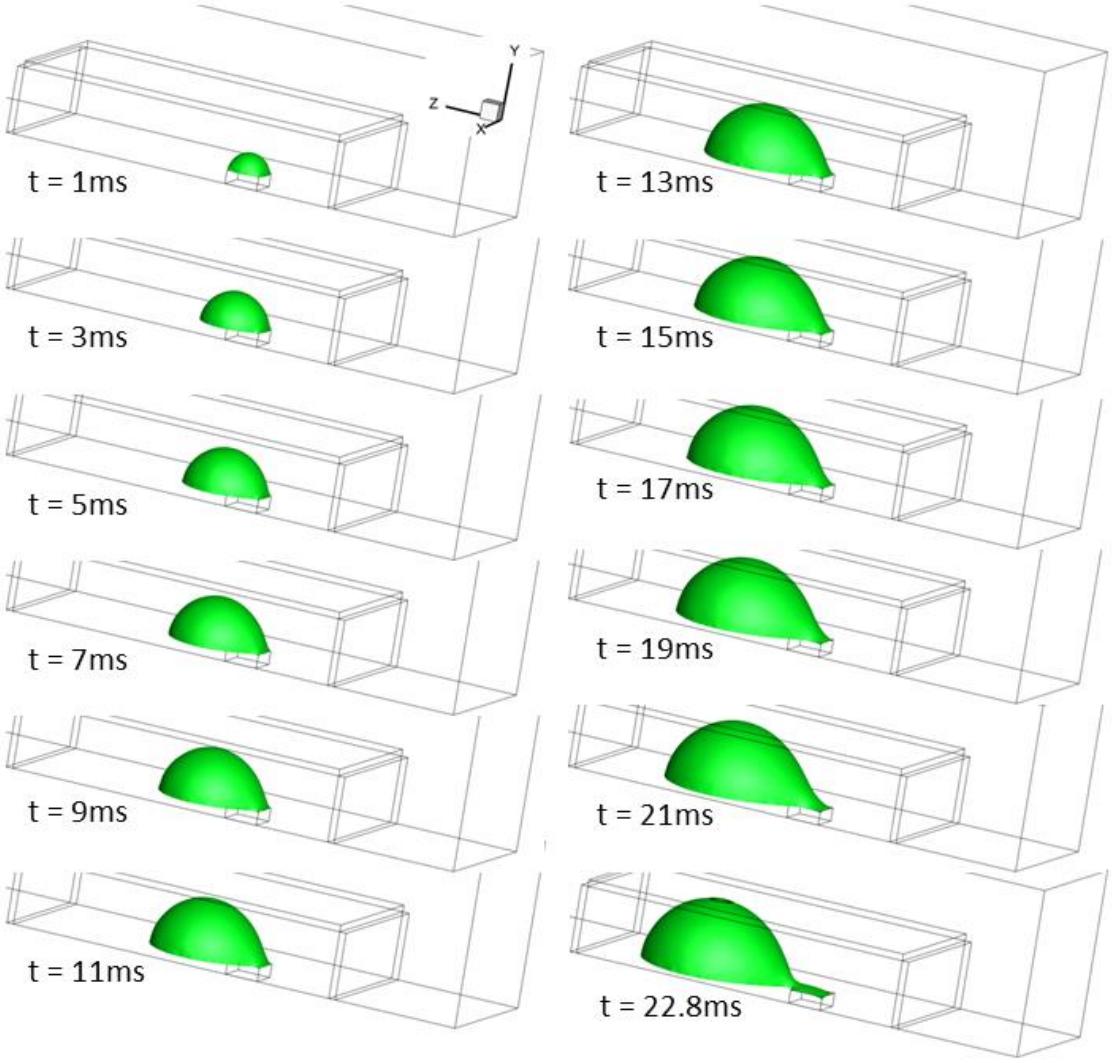

Figure 4.23. One cycle of droplet emergence time resolved images of numerical results using dynamic contact angle (DCA) approach in FLUENT. Air inlet velocity, V_a = 10 m/s; water inlet velocity, V_w = 0.04 m/s.

Similarly, the time evolution using dynamic contact angle (DCA) simulation is presented in Figure 4.23. In comparison with the results in SCA, the droplet interface in DCA is less spherical with a longer chord length and a shorter height. Droplets emerge faster compared to the SCA case, and detach from the water pore at around 22.8 ms which is equivalent to a shedding frequency of 44 Hz. The emergence frequency is smaller in SCA simulations thus allowing the droplet to grow slightly higher in comparison with DCA simulations.

To further investigate the treatment of the dynamic contact line, the advancing and receding contact angles as well as the droplet chord length are presented in Figure 4.24 for both SCA and DCA using FLUENT.

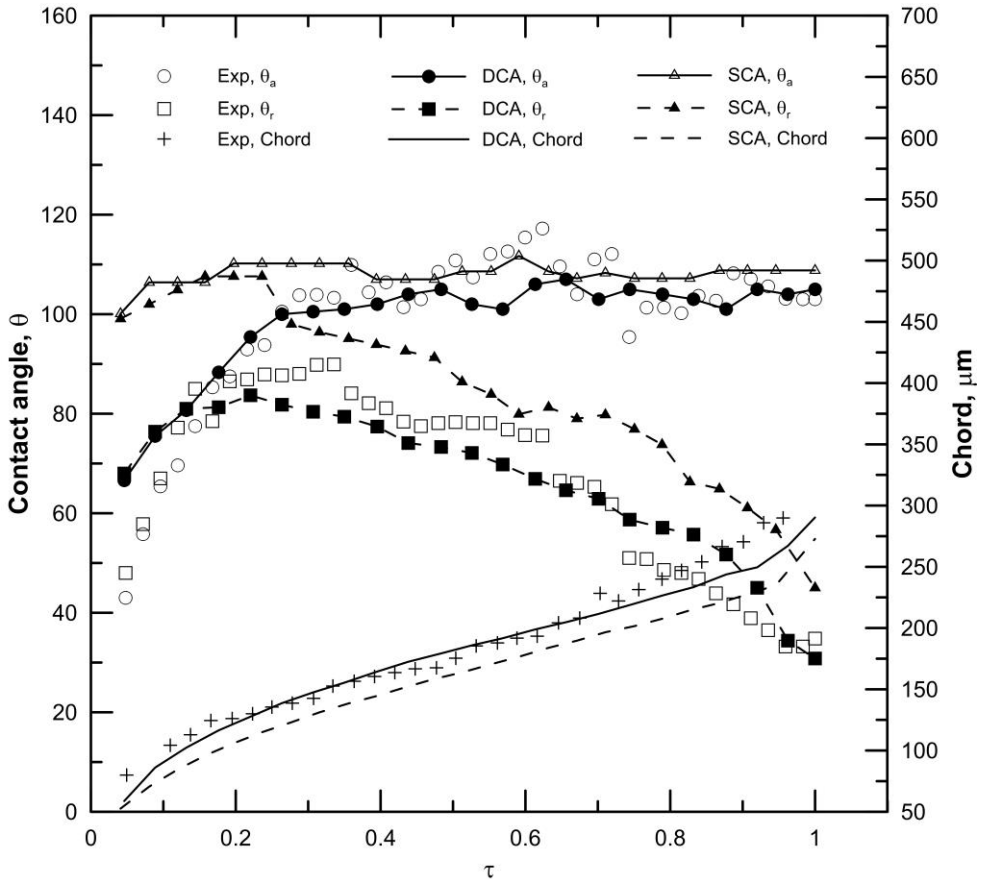

Figure 4.24. Comparison of experimental result and the evolution of dynamic contact angle using FLUENT.

The results using DCA approach provide a significant improvement in dynamic contact angle as well as the chord length compare to the SCA results. Considerable deviation in receding contact angle between SCA and experimental results is observed. Using DCA approach, the results of receding angle as well as the chord length agree with the experiments well overall except in the early emergence phase ($\tau < 0.2$). The higher advancing and receding contact angles in early emergence phase cause the droplet to form a nearly spherical shape.

Furthermore, comparing the results of DCA simulations using CFD-ACE+ (cf. Figure 4.13) and FLUENT, both numerical approaches track the dynamics of the droplet reasonably well in a dimensionless time scale. Although the emergence frequency (70 Hz in CFD-ACE+ vs. 44 Hz in FLUENT) are still higher than the value in experiment (13.2 Hz in Figure 3.5). Note that a uniform grid size 6.25 μm is used in CFD-ACE+ simulation, whereas the finest adaptive grid size for FLUENT is 2.5 μm. The CFD-ACE+ simulations are consistent with the experimental observations in the early emergence phase (i.e. period I: surface tension force dominant in Figure 3.8). However, they deviate significantly for the receding angle in the later part of the emergence phase (i.e. period III: drag force dominant). The DCA approach in CFD-ACE+ using Eq. (4.19) derived from the one-dimensional capillary rise experiment provides better capability to capture the wettability in the surface tension dominated regime but is not satisfactory in the drag force dominated regime where the effect of flow field is important in the vicinity of the moving contact line. On the other hand, the DCA modeling using the Hoffman function in FLUENT presents better results in both regime though deviations still exist in the surface tension force dominated period which might be due to surface roughness and inhomogeneities physically present in the experiment and not accounted for in the numerical model.

4.5. Summary

The dynamics of single water droplet emerging from a pore in the presence of a cross flow of air was investigated numerically in a modeled PEMFC cathode gas channel. The importance of accounting for the pore connectivity during the initial emergence phase was highlighted in the prior work of Zhu et al. [56]. In the present work, we explicitly resolve the pore and also examine the critical role of dynamic contact angle modelling. Different approaches of dynamic contact angle implementations were examined, and the results were compared with the results using static contact angle model as well as the experimental measurements. The emphasis here is placed upon the implementation of two empirical velocity dependent contact angle functions as well as the theoretically based Hoffmann equation in two different numerical software CFD-ACE+ and FLUENT. There are two main conclusions of this study. First, grid refinement is critical in order to

capture the salient motion of a moving droplet. With the extensive use of nonuniform, adaptive refinement in the region of droplet movement the dynamic evolution of contact angles are well modeled in one emergence cycle without sacrificing the computational cost. Second, a velocity dependent contact angle function derived either from droplet emergence experiments or from one-dimensional capillary rise experiments doesn't provide satisfactory tracking of the contact line motion of an emerging droplet in a single channel because droplets encounter different flow regimes and emergence phase. Significantly improved simulations are obtained by introducing the Hoffmann equation which takes into account more fundamental aspects of the local contact line velocity as a function of the flow field. The dynamic contact angle model was validated against numerically and experimentally documented droplet impacts on a horizontal surface. Spreading and recoiling parameters were compared and presented for validation. This model was then used to investigate a flow condition from our own experiments in a model fuel cell microchannel and the results show that the Hoffmann equation improves the accuracy of predicting the advancing and receding contact angle of an emerging droplet inside a channel.

Chapter 5

5 Pressure Signature and Diagnostic Tool

Experimental data and signal analysis of pressure drop measurement from a two-phase flow fixture are presented in this chapter. The pressure drop setup consists of a single-channel fixture, flow delivery for air and water, data acquisition and a high speed digital camera. The flow fixture was designed to allow replaceable GDL and bipolar plates for testing of different channel geometries and materials. High accuracy dynamic pressure sensors were installed at different locations of the fixture. Experiments were conducted for flow rates of air and liquid water similar to those in an operating fuel cell. Power spectrum analysis was performed on the pressure time series data and the results were used to construct a flow regime map. When comparing with footage from the high speed digital camera, it was found that the presence of water at the outlet was the major cause of a low-frequency periodic oscillation of pressure signal. The present study concludes with several suggestions for future work, including verification of data repeatability, multiple water injection, modification of design of flow plate outlet to avoid water accumulation, and real time monitoring using power spectrum of pressure signal.

5.1. Introduction

Understanding the behaviour of liquid water in PEMFC gas channels is a key to effective water management. From an on-board diagnostic aspect, the pressure signature of a unit cell shows significant advantages in providing immediate and real time linkage between the air/water two-phase flow behaviours [3]. An increase of pressure drop would

indicate water accumulation or water film build-up in the channel, while an abrupt decrease would imply water removal at the outlet [18]. However, using pressure drop as a diagnostic tool for the water behaviour, particularly in water removal, still has deficiencies. For example, high frequency oscillations in pressure drop signal, which arise from unstable two-phase flow transport in the channel, are usually observed. Such oscillations might not indicate any water removal/build-up at the outlet yet they are difficult to distinguish and separate from regular increase/decrease patterns of pressure drop profile. Moreover, considering the requirement of relatively low pressure drop (usually < 10 mbar) across fuel cell channels, signal noises from disturbances and measurement errors may contribute considerably to the results as well as reducing the accuracy and even changing the pattern of the pressure drop profile. Real-time visualizations are used here to assist the interpretation of the pressure drop profiles, and to identify the potential of using the pressure drop as a diagnostic tool for two-phase flow in PEMFCs. The specific objectives are to perform pressure signal measurement in the two-phase flow fixture with liquid water fluxes representative of real operating conditions (i.e. current density) and identify and delineate the water management regimes in the channel and GDLs.

5.2. Method and Apparatus

Figure 5.1 shows the experimental setup which comprises a two-phase flow fixture (supplied by Ballard Power System), water pump (Harvard Apparatus, PHD2000), mass flow controller of air (Brooks, MFC 5850i), differential pressure sensor (Honeywell, FP2000), gauge pressure senor (Noshok, 100 series) and data acquisition system (National Instruments, LabVIEW 8.6 and DAQ). The combination of small hydraulic diameter of the flow channel with dry (air only) and two-phase flow regimes, the pressure drops span a large range of values making precise measurements challenging. The mass flow controller provides fine adjustment of air flow rate from 0 to 1,000 sccm in a 1% full scale precision. The measurement range of the differential pressure sensor is up to 5 psi, with a 0.1% accuracy and 3 KHz frequency response.

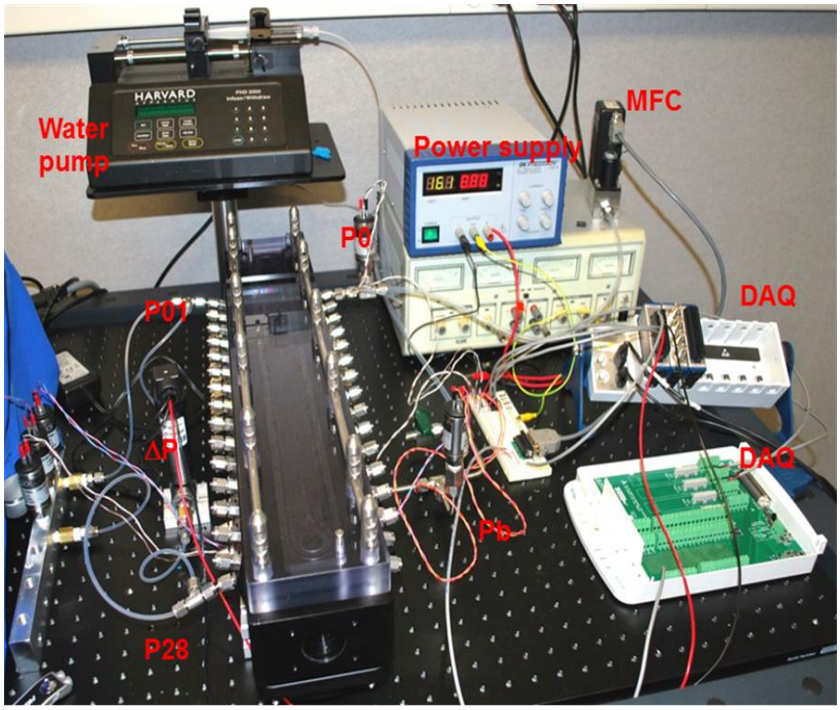

Figure 5.1. Experimental setup in pressure drop measurement.

The user control interface was developed using LabVIEW 8.6 to provide real-time equipment control, monitoring and data logging. The two-phase flow fixture can be configured with several options including a transparent plastic flow channel or a non-transparent carbon flow plate (CFP), and an untreated carbon paper which is clamped together using an air pressurized device. The clamping pressure (Pb) is maintained at around 75 psi to provide reliable sealing without leakage. The chamber of the clamping device provides 29 pressure ports (denoted as P01 to P29) and 28 water injection ports (W01 to W28) which are 15 mm apart, respectively. Figure 5.2 illustrates the corresponding locations of pressure and water ports.

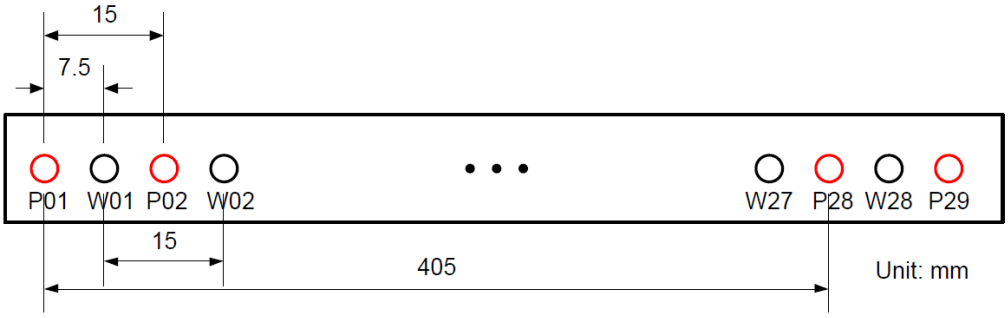

Figure 5.2. Illustration of the pressure measurement and water injection ports.

A Toray TGP-H-060 non-woven fibrous GDL material was used. A series of 1 mm diameter holes were punched into the GDL at the corresponding locations of pressure and water ports. In this arrangement, the water droplet is thus allowed to enter the flow channel through the 1 mm GDL holes. A design sample of the flow channel plate is presented in Figure 5.3 and is either made from transparent plastic or non-transparent carbon.

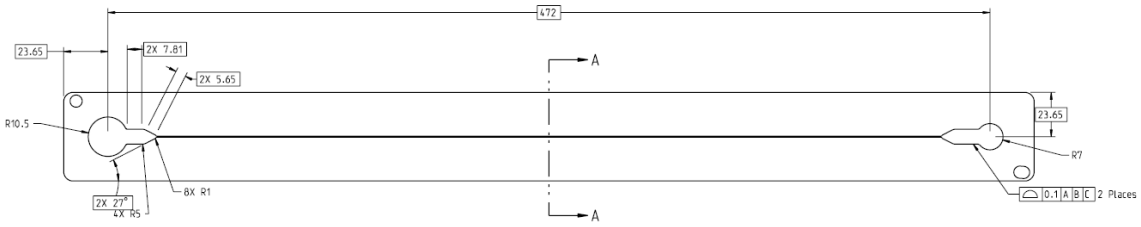

Figure 5.3. Flow channel plates (Ballard Power System). Unit: mm

The schematics and dimensions of several flow channels are shown in Figure 5.4. Dimensions are measured under a microscope to ensure accuracy in prescribing the hydraulic diameter (D_h) required for calculating the theoretical pressure drop across the channel. Note that the drawing of CFP-0D is not shown here due to confidentiality.

Plate	Plastic-0A	Plastic-02	CFP-010A	CFP-0D
D_h (μm), measured	675	536	895	737
D_h (μm), designed	603	463	889	NA

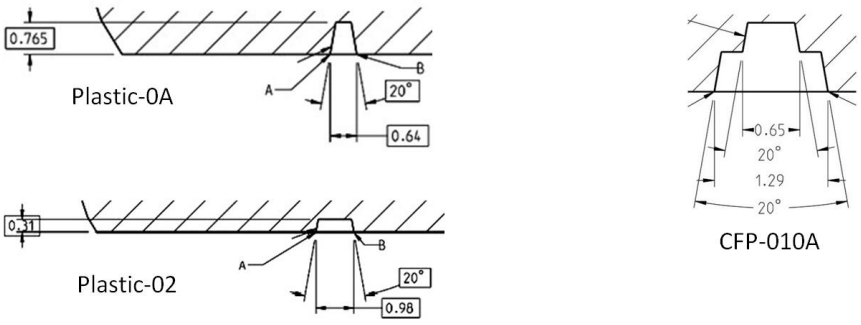

Figure 5.4. Schematics and dimensions of the flow channels.

The pressure drop (ΔP) in this study is measured between P01 and P28. First of all, the system is examined by measuring the pressure drop of a dry channel (i.e. only gas phase) under different air flow rates. A sample of the real time signal of the flow rate and the

pressure drop (ΔP_{0128}) across port P01 and P28 in flow plate Plastic-0A is shown in Figure 5.5. The corresponding Reynolds number range from 110 to 1100 where a laminar flow regime is maintained.

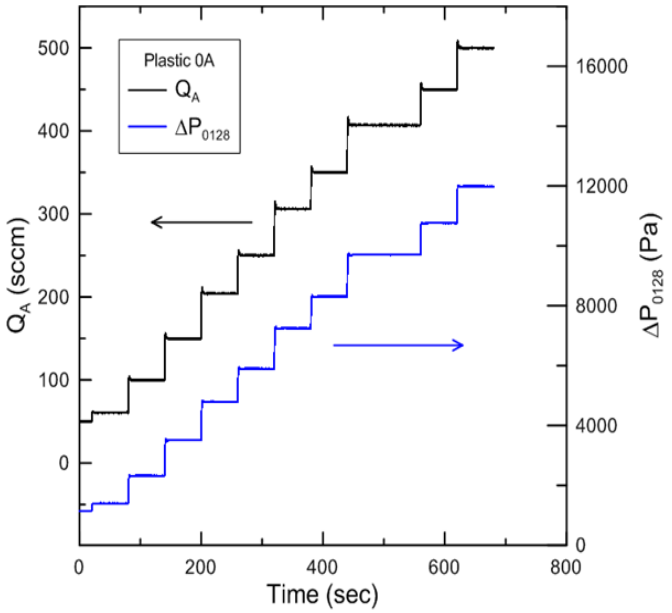

Figure 5.5. Real time signal of flow rate versus pressure drop in flow plate Plastic-0A.

Four different flow plates are investigated and the comparison of Darcy friction factor between the experimental and theoretical value using Poiseuille equation is shown in Figure 5.6. The Darcy friction factor, *f*, determined from the pressure drop measurement is expressed as:

$$f = \frac{2\Delta P_{0128} D_h}{\rho_A V_A^{\,2} L_{0128}} \tag{5.1}$$

where L_{0128} is the channel length between pressure port P01 and P28. The curves are in good agreement. This verification provides a calibration curve and a reference base for wet channel measurements.

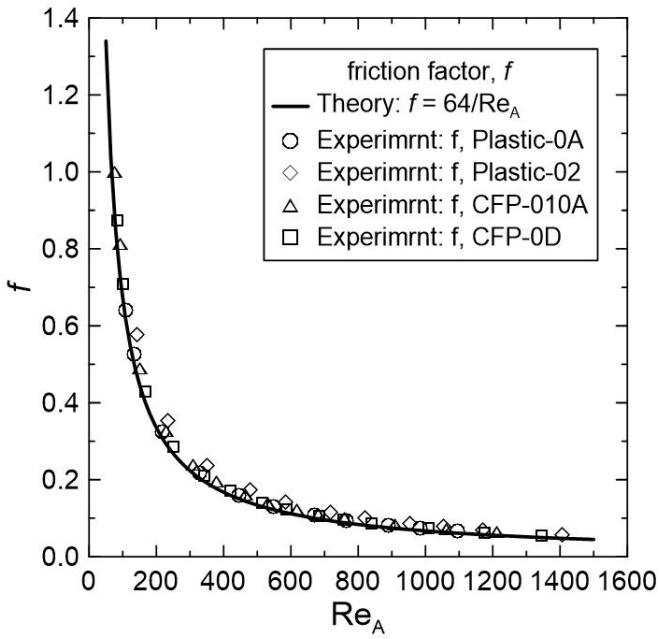

Figure 5.6. Pressure drop calibration curve for various flow plates.

The matrix of flow conditions (each element represents the case number) shown in Table 5.1 comprises the combinations of air and water flow rates derived from typical fuel cell operating conditions. Two plastic plates (0A and 02) and two carbon flow plates (010A and 0D) are examined using this matrix.

Table 5.1. Test conditions matrix

F	96484
% reactant	20.90%
Fixture area	6.696 cm2
R	8.314
Po	1.01E+05 Pa
To	293.15 K

Current Density (A/cm^2)	Ox Stoic	Water injection (mL/min)	Air Flow (cc/min)
2	1.7	0.075	407
1.5	1.7	0.056	306
1	1.7	0.037	204
0.3	1.7	0.011	61

Qw (ml/min) \ Qa (sccm)	407	306	204	61
0.075	11	12	13	14
0.056	21	22	23	24
0.037	31	32	33	34
0.011	41	42	43	44

Air velocity ranged from 1.4 m/s ~ 23.6 m/s

In each measurement, the pressure drop signal is initially recorded for three minutes in the dry state to ensure the pressure drop ΔP_{0128} falls within the calibration curve range shown in Figure 5.6. Single water injection from water port W01 as well as dual injection from W01 and W15 are both tested for certain flow plates. To maintain the amount of water injected into the channel constant, the flow rate is divided by two for the dual injection case. After each measurement and before starting a new test, the flow channel is air purged for at least 30 minutes to ensure both channel and GDL are in a dry state.

5.3. Results and Discussions

5.3.1. Characterization of mean pressure drop

A sample of the real-time pressure drop signal of Plastic-0A flow plate using single injection and under the flow condition of Case 11 is shown in Figure 5.7. While water is introduced, a spike appears in the signal due to the water accumulation in the chamber before being pushed into the channel; some oscillations are also evident. A time span of more than 20 minutes is recorded and averaged to represent the mean pressure drop for a given test condition. The mean pressure drop in this case is 10,506 Pa compare to a value of 9,731 Pa in a dry state. That is, an increase of 775 Pa due to water coverage in the channel is observed. The increase of pressure drop due to water accumulation is a key challenge of water management and may lead to flow misdistribution, and reduction of the fuel cell performance and durability.

The signal exhibits various oscillation patterns in different stage which indicate dynamic characteristics. Though there seems to be a characteristic frequency present in some intervals, a dominated value could not be identified. The dynamic features underly the complexity of the flow and the challenge in achieving an analytic model of the process.

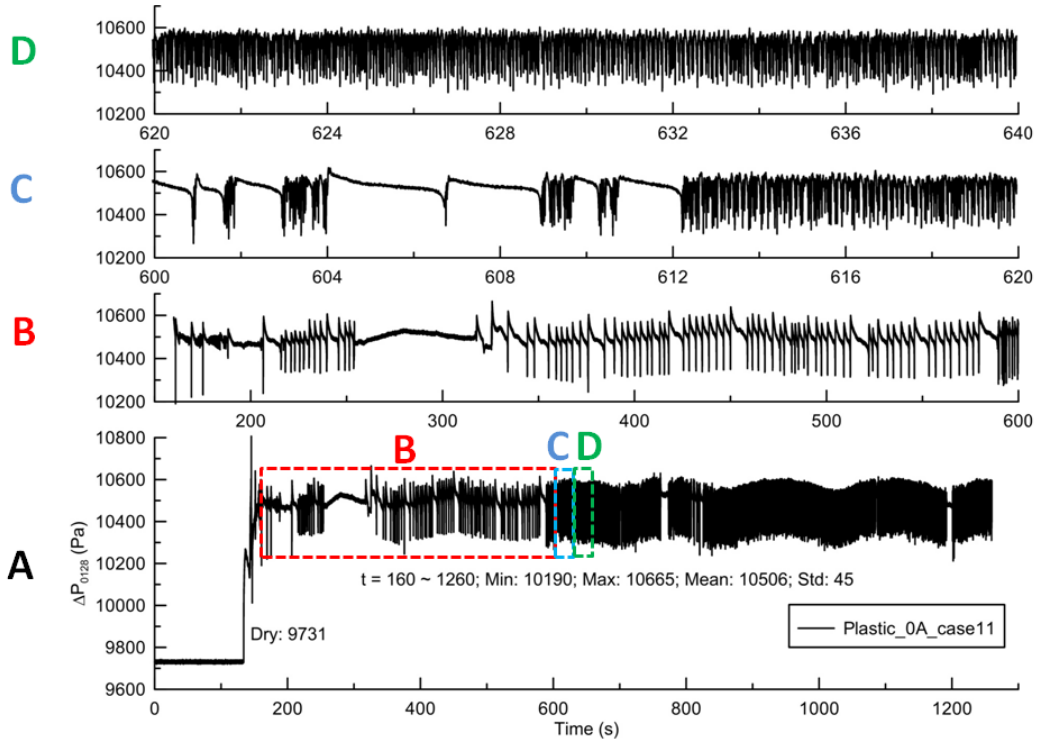

Figure 5.7. Pressure drop signal of Plastic-0A using single injection under the Case 11 test condition.

The ratio of two-phase flow to the single gas phase pressure drop can be used as a simple indicator of the liquid buildup in fuel cell flow channel. This ratio, also known as the normalized pressure drop or the two-phase friction multiplier [24], is defined by Eq. (5.2):

$$\phi_g^{\,2} = \frac{\Delta P_{2\phi}}{\Delta P_g} \tag{5.2}$$

where $\Delta P_{2\phi}$ and ΔP_g is the pressure drop with a two-phase flow and a single-phase gas flow in the channel, respectively. A higher ratio represents a higher water buildup in the channel. The mean pressure drop of Plastic-0A flow channel using single injection for different flow conditions is listed in Table 5.2. The additional database of pressure drop in different test cases is listed in Appendix E. It is shown that while varying the air flow rate (Case 11 to 14), the difference of pressure drop ($\Delta P_{2\phi}$ - ΔP_g) decreases; though the friction multiplier (ϕ_g^2) increases. The highest friction multiplier which appears in Case 24, implies a higher tendency of slug flow is formed. Whereas, in highest air flow rate

(Qa = 407 sccm), the friction multiplier tends to unity and implies a strong air flow inducing a mist two-phase flow regime in the channel.

Table 5.2. Pressure drop measurement of Plastic-0A using single water injection.

Plastic-0A single injection, ΔP_{0128}							
Case	Qw	Qa	Re_A	Dry (ΔP_g)	Wet ($\Delta P_{2\phi}$)	Wet-Dry ($\Delta P_{2\phi} - \Delta P_g$)	Wet/Dry ($\phi_g{}^2$)
#11	0.075	407	891	9,731	10,506	775	1.080
#12		306	670	7,276	7,924	648	1.089
#13		204	447	4,814	5,359	545	1.113
#14		61	134	1,488	1,794	306	1.206
#21	0.056	407	891	9,699	10,322	623	1.064
#22		306	670	7,238	8,083	845	1.117
#23		204	447	4,818	5,279	461	1.096
#24		61	134	1,431	1,752	321	1.224
#31	0.037	407	891	9,804	10,625	821	1.084
#32		306	670	7,307	7,858	551	1.075
#33		204	447	4,792	5,429	637	1.133
#34		61	134	1,422	1,679	257	1.181
#41	0.011	407	891	9,793	9,983	190	1.019
#42		306	670	7,325	7,555	230	1.031
#43		204	447	4,850	5,248	398	1.082
#44		61	134	1,435	1,698	263	1.183

The difference of pressure drop between dry and wet channel is expected to be controlled at below 1 kPa (10 mbar) for a given flow channel in order to minimize the excess power loss[1]. In this study, as shown in Table 12.2 in Appendix E, the difference of pressure drop of Plate-02 is worth noticing since the majority of its value exceeds 1 kPa except in the lowest water injection rate (i.e. Case 41 to Case 44). The flow channel geometry of Plastic-02 might not be optimized when large amount of water exist in the gas channel at high current density conditions. However, CFP-010A and CFP-0D flow channels present a relatively low pressure drop deviation and are all below 1 kPa criterion. As discussed in Figure 2.5, a secondary channel design on top of a triangular gas channel can provide passive water removal due to capillary forces. This type of channel design provides an

[1] Private communication, Ballard Power Systems

effective way to let water path through the secondary channel in the upper portion while maintaining a suitable air passage in the lower portion of the channel. Plots of the difference of pressure drop in test conditions are shown in Figure 5.8.

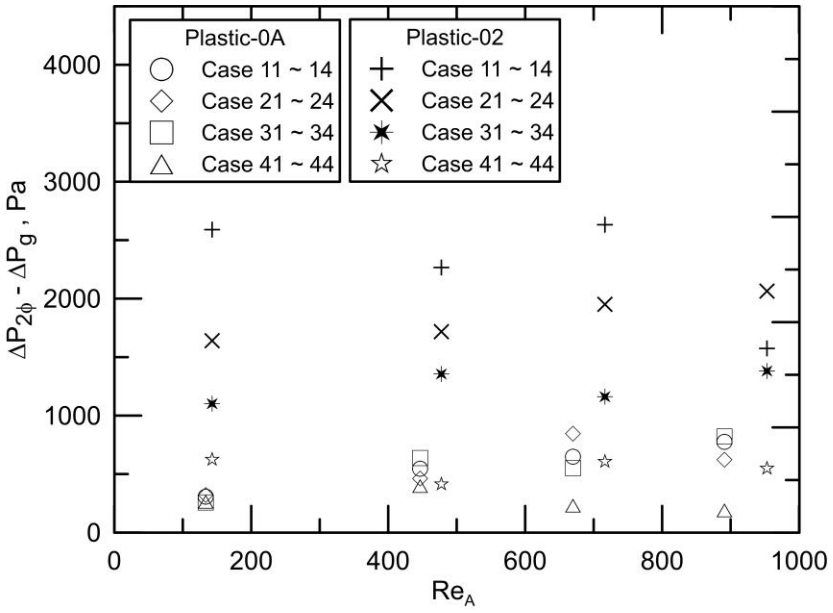

(a)

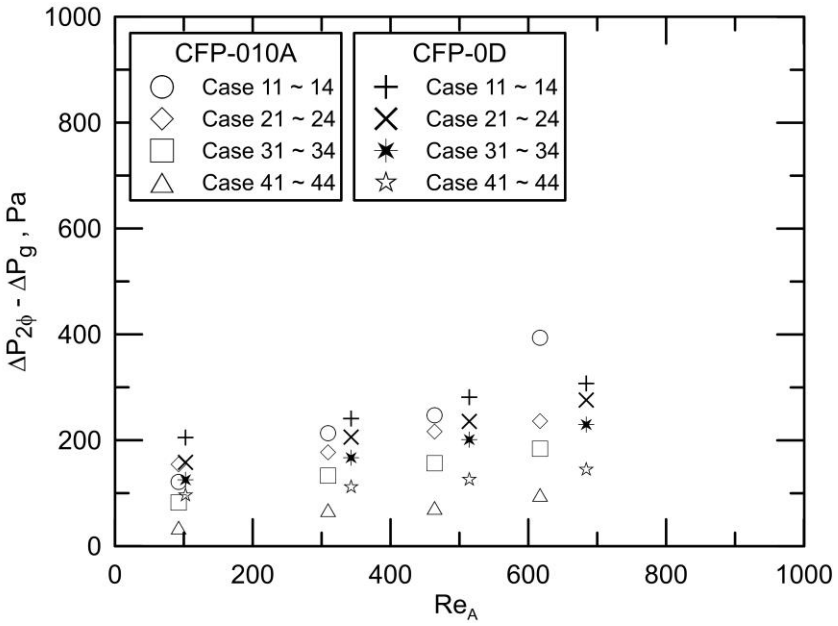

(b)

Figure 5.8 The effects of air flow (Re_A) and flow channel geometry on the difference between wet and dry pressure drop under single water injection. (a) Plastic-0A and Plastic-02, (b) CFP-010A and CFP-0D.

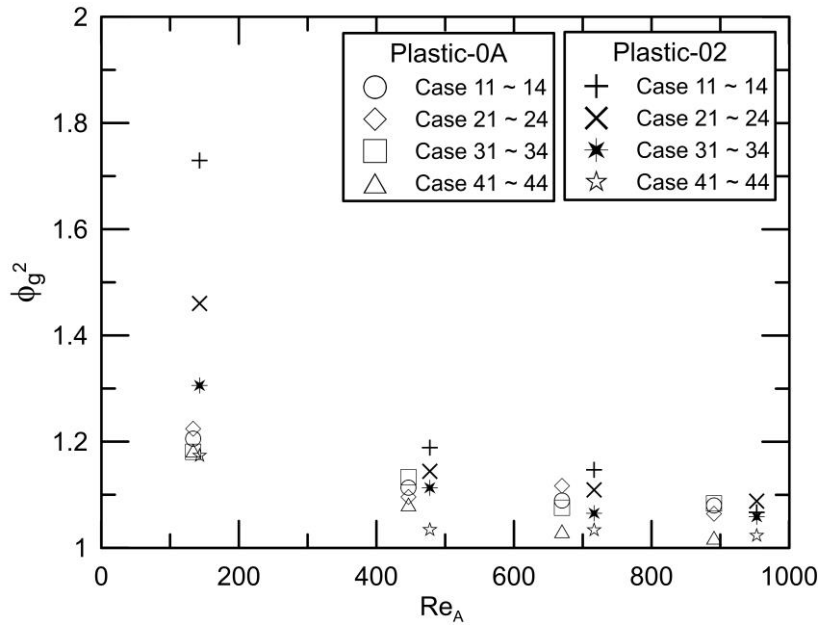

(a)

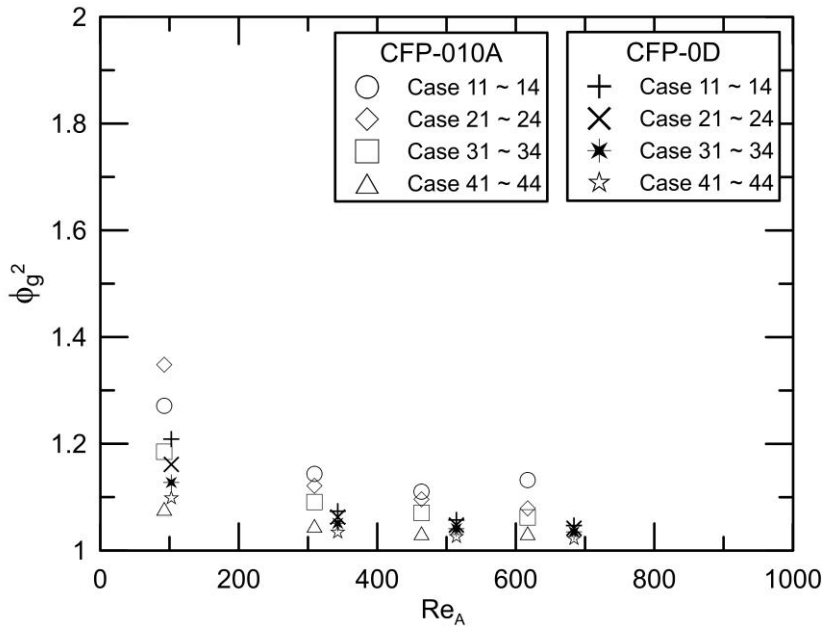

(b)

Figure 5.9. The effects of air flow (Re_A) and flow channel geometry on the friction multiplier under single water injection. (a) Plastic-0A and Plastic-02, (b) CFP-010A and CFP-0D.

To better describe the effect of air flow on the water coverage in the flow channels, comparison of the friction multiplier using single water injection are plotted against the

Reynolds number of air flow as shown in Figure 5.9. The friction multiplier decreases as Re_A increases. It generally varies from nearly 1.0 to around 1.7. However, at lowest Re_A, Plastic-02 channel exhibits a higher ratio in some test conditions which indicate a higher tendency for slug flow formation. Moreover, carbon flow plate CFP-0D reveals a lower friction multiplier ratio in most cases.

5.3.2. Dynamic characteristics

An oscillation of the pressure drop signal is observed in Plastic-0A flow channel plate using single water injection under Case 34 flow conditions. A sample of real time pressure drop signal is presented in Figure 5.10.

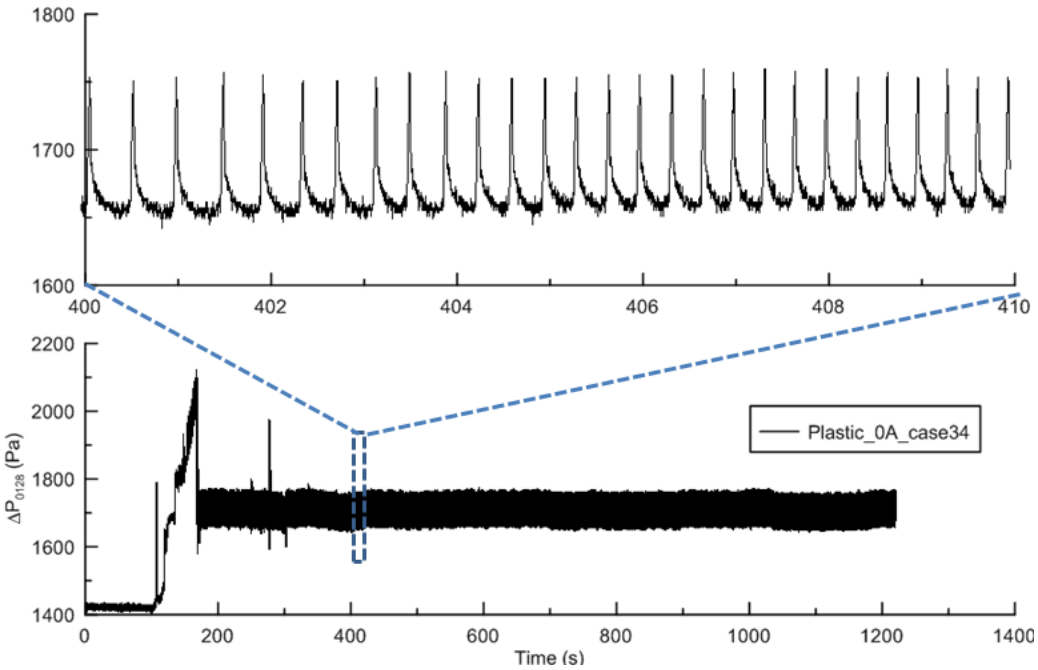

Figure 5.10. Real-time pressure drop signal of Plastic-0A channel using single water injection under Case 34 flow conditions.

The oscillation frequency is identified as 2.8 Hz using DFT (Discrete Fourier Transform). This frequency was found to be correlated to the water accumulation and drainage process at the opening of channel outlet. The accumulated water block the opening for a certain period of time which causes the pressure to increase until it levels off when water has been purged out of the outlet. Some snap shot images shown in Figure 5.11 highlights

this process. It is worth to noting that a proper design of the end of the channel linking to the outlet as well as the shape and surface property of the outlet are critical in order to enhance water expulsion.

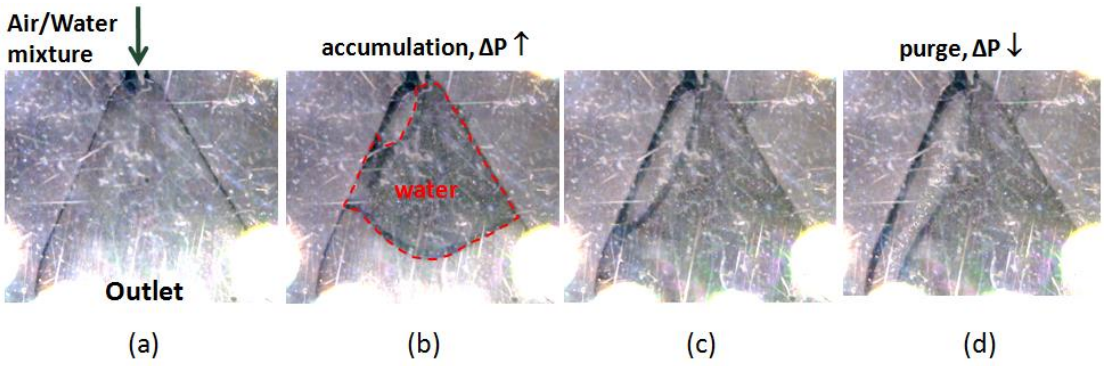

Figure 5.11. Snap shot images of water accumulation and drainage process.

Though the frequency is related to the water expelling process, it does not present in all the flow plates in this study. Therefore, we focus our attempt to devise a flow regime diagnostic relation to plate CFP-010A due to its lower pressure drop difference as discussed earlier.

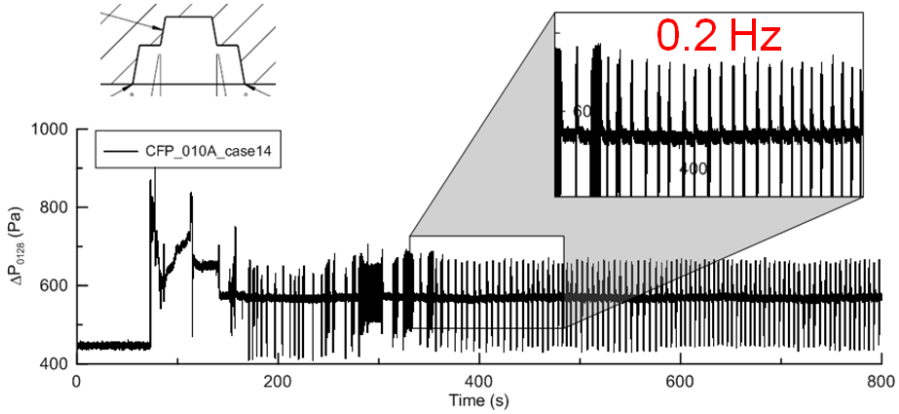

Figure 5.12. Typical real time pressure drop signal of CFP-010A channel using single water injection under Case 14 flow condition.

Figure 5.12 shows the pressure drop signal using single water injection in CFP-010A under Case 14 flow condition. Under this condition, the air flow rate is at the lowest value whereas the water flow rate is highest. The analysis reveals lower frequency oscillations which implies slug regime in the channel. This is consistent with the fact that slug flow is characterized by a slower water build up process. The overall picture of the

frequency analysis is shown in Figure 5.13. The frequencies range mostly below 1 Hz but do not present a clear trend for identifying the flow regimes.

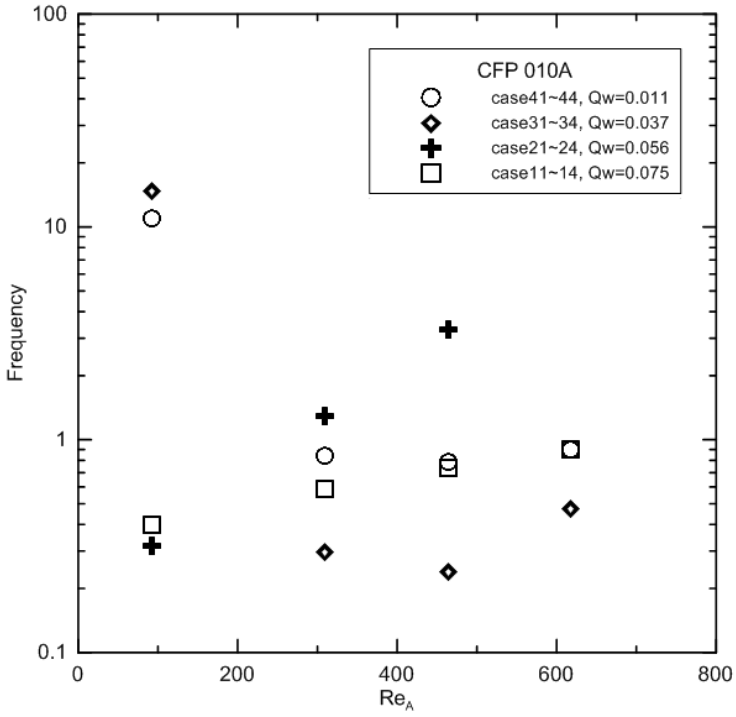

Figure 5.13. Dominant frequency in two-phase flow regime of CFP-010A.

At lower water injection rate e.g. Qw = 0.011 and Qw = 0.037, increasing the air flow rate reduces the frequency from about the order of 10 Hz to 1 Hz indicating a flow regime changes. On the other hand, the trend is reversed while using higher water injection rate e.g. Qw = 0.056 and Qw = 0.075 since the frequency increase with air flow rate. To further investigate the evolution of flow regime and how the strength of the pressure drop signal is distributed in the frequency domain respective to the strengths of other background signals associated with the flow regime, the power spectral density (PSD) of the pressure drop signal is deduced by squaring its amplitude. A plot of power spectrum of CFP-010A using different flow conditions to illustrate the extreme conditions is presented in Figure 5.14. That is, at highest water injection, Case 11 and Case 14 represent highest air flow versus lowest air flow, respectively. At lowest water injection, Case 41 and Case 44 represent the effect of highest and lowest of air flow.

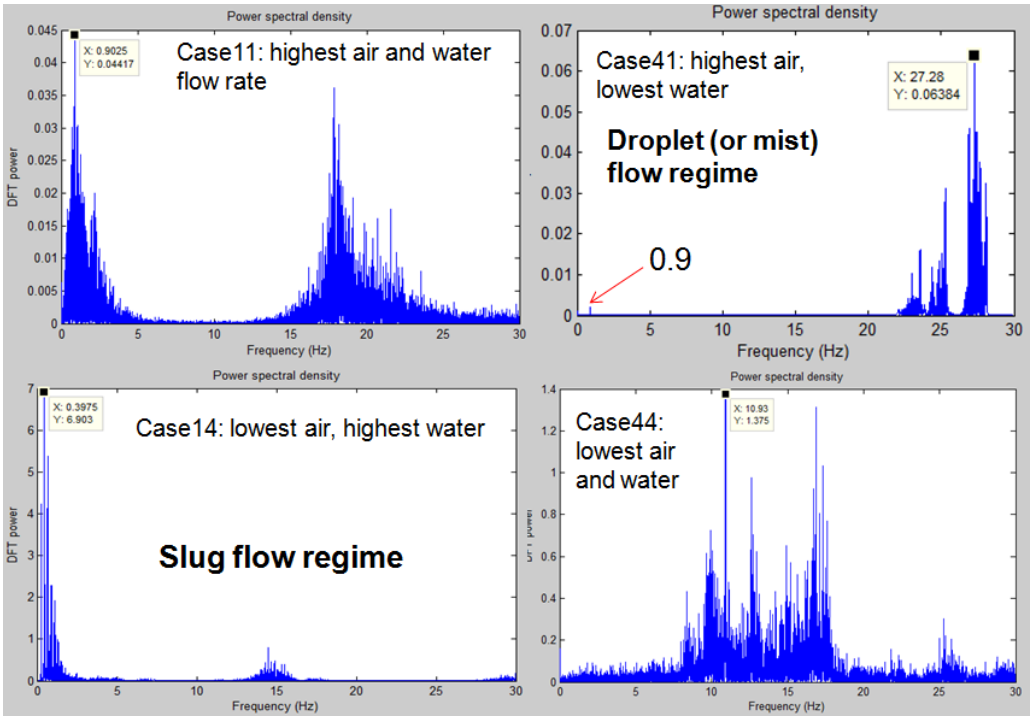

Figure 5.14. Power spectrum of Case 11, 14, 41 and 44 of CFP 010A.

The amplitude of the spectrum reveals the change between flow regimes. For slug slow regime, the amplitude of the signal surpasses that for the other flow regime even though the frequency is low. This implies a strong pulse-like signal relative to the background which might due to the water accumulation and purging process.

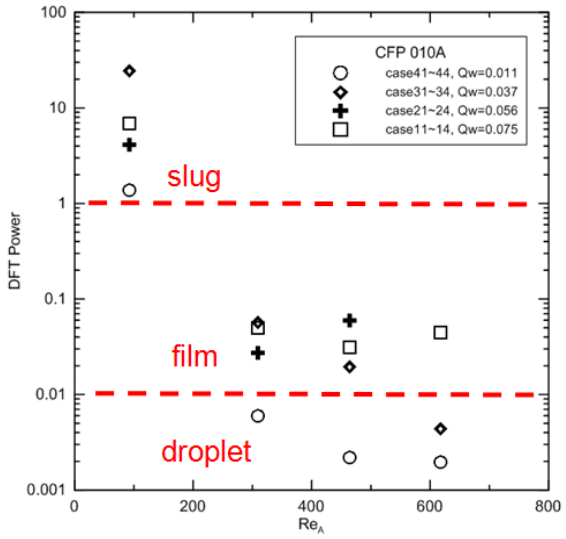

Figure 5.15. Flow regime identification using DFT (Discrete Fourier Transform) power of the pressure drop signal.

Figure 5.15 synthesizes the relationship between the spectra power amplitude and the flow regimes under the effects of water and air flow rates. The amplitude corresponds to the highest value in each test condition. This successfully identifies the boundaries between different flow regimes under various test conditions. These boundaries might change slightly if test conditions varied further. This is a distinct, order of magnitude difference between flow regimes. The power spectrum analysis of the pressure drop is proposed as a useful and practical approach to identify and characterize dominant flow patterns and regime where in operating fuel cells where flow visualization is not possible due to the opaque flow channel. This approach also has the potential to be extended to real time monitoring of flow regimes in the channels and stack.

5.4. Summary

The ability to monitor or diagnose flow regime change and the onset of flooding in operating fuel cells would open the door for active control of flow conditions to achieve more effective water management strategies. The experiments and analysis presented in the Chapter show that pressure signal analysis cab be used to provide real time monitoring of air/water two-phase flow behaviors. The experimental work was conducted to characterize the two-phase flow in a single flow channel using an ex-situ two-phase flow fixture. Several flow channels design identical to those used in the commercial fuel cell stacks were tested under different operating conditions. Database of pressure drop as well as the characterization of flow regimes and the development of flow diagnostics tool were explored. A flow channel with secondary channel design located on the top was found to provide a better passage to lift the water due to the effect of capillary force. The accumulation and purging process of water at the outlet is the primary cause for the low frequency periodic oscillation of pressure drop due to water. Finally, using power spectrum analysis on the pressure drop signal provides a suitable approach for constructing the flow regime.

Chapter 6

6 Conclusion and future works

6.1. Conclusion

An experimental and numerical investigation of the two-phase flow in a fuel cell gas channel was presented in this thesis. First, observations of the dynamics of a single droplet emerging from a pore into a model PEMFC flow channel were made using microfluidics technology. The development of the transparent microchip platform allowed quantitative flow visualization of droplet dynamic under a range of air flows and water injection rates. Different flow patterns were analyzed and a flow map was constructed, and the time evolution of the contact line during the droplet emergence and detachment cycle was determined. These results set the foundation for validation of the numerical model. Numerical simulations using the VOF method were then undertaken with to resolving the time-dependent behaviour of a single droplet throughout and emergence cycle. The focus of the modeling was treatments of the contact angle at the three-phase interface on a hydrophobic surface. Both empirical and theoretical velocity dependent contact angle functions were implemented in CFD software and their performance examined through a set of simulations representing experimental conditions. The last part of the thesis was focused on identifying relationships between pressure drop signals and flow regimes as a basis for developing design and diagnostic tools for water management. A two-phase flow fixture consisting of gas flow channel identical to those used in a commercial fuel cell stack was used to further study the two-phase flow behaviour via ex-situ measurements and observations. This two-phase flow fixture

provides allowed examination of the effect of channel geometry and flow conditions on the pressure signature. The results were analyzed and the potential for using pressure drop signals as a diagnostics tool was discussed.

The main contributions of this work are:

1. Single droplet dynamics: The detachment and subsequent dynamic evolution of single droplet in microchannel was analyzed experimentally. Three different flow patterns were identified and a flow regime map was obtained. The time evolutions of the advancing and receding contact angles in the droplet regime were also determined.
2. Modeling of dynamic contact angle: VOF simulations with a dynamic contact angle treatment were performed for the first time. A velocity dependent contact angle function deduced from experiments as well as theoretical contact line relation (Hoffmann function) were implemented into VOF simulations. The simulations highlight the critical importance of a dynamic contact line treatment and show that using the Hoffmann function yields more physical simulations.
3. Flow diagnostic tool: Pressure signature were acquired and analyzed using a custom designed two-phase flow apparatus with flow field plates identical to those in commercial stacks. The results provide evidence of the importance of channel design with secondary channels. It is shown that the flow regimes can be characterized using power spectrum density of the normalized pressure drop signal. This provides a good basis for ex-situ diagnostics.

6.2. Future works

Future work includes further investigation on the experimental and numerical works for droplet emergence as well as the flow diagnostics tool.

Experimental work on droplet emergence

In present study, only smooth surface channels were examined. To further study the effect of surface properties, implementation of surface roughness is essential. Some preliminary experiments were performed, but were not analyzed as systematic experimental tests were not completed due to the challenges of microfabrication process.

Experiments with multiple water injection would also be valuable to approach fuel cell operating conditions when simultaneous emergence and interaction of multiple droplets occurs.

Numerical work on droplet emergence

To complement the experimental work, modelling developments should be undertaken to extend the dynamic angle model (Hoffmann function) to rough surfaces representative of GDLs. Simulations with further grid refinement should also be undertaken with high performance computing resources.

Flow diagnostics tool

The pressure signal-flow regime correlation identified in this study opens the possibility for practical flow diagnostics. Several avenues could be pursues: (1) repeatability verification of pressure drop; (2) the design of the flow plate outlet to minimize the water accumulation and increase drainage capability; (3) real time monitoring using power spectrum of pressure drop; (4) validation and further analysis with the VOF; (5) multiple water injections.

7 Bibliography

[1] N. Shao, A. Gavriilidis, P. Angeli, Flow regimes for adiabatic gas-liquid flow in microchannels, Chem. Eng. Sci. 64 (2009) 2749–2761.

[2] T. Berning, N. Djilali, A 3D, multiphase, multicomponent model of the cathode and anode of a PEM fuel cell, J. Electrochem. Soc. 150 (2003) A1589–A1598.

[3] T.A. Trabold, Minichannels in Polymer Electrolyte Membrane Fuel Cells, Heat Transf. Eng. 26 (2005) 3–12.

[4] A. Bazylak, J. Heinrich, N. Djilali, D. Sinton, Liquid water transport between graphite paper and a solid surface, J. Power Sources. 185 (2008) 1147–1153.

[5] K. Tüber, D. Pócza, C. Hebling, K. Tuber, D. Pocza, Visualization of water buildup in the cathode of a transparent PEM fuel cell, J. Power Sources. 124 (2003) 403–414.

[6] X.G. Yang, F.Y. Zhang, A.L. Lubawy, C.Y. Wang, Visualization of liquid water transport in a PEFC, Electrochem. Solid State Lett. 7 (2004) A408–A411.

[7] K.S. Chen, M.A. Hickner, D.R. Noble, Simplified models for predicting the onset of liquid water droplet instability at the gas diffusion layer/gas flow channel interface, Int. J. Energy Res. 29 (2005) 1113–1132.

[8] F.Y. Zhang, X.G. Yang, C.Y. Wang, Liquid water removal from a polymer electrolyte fuel cell, J. Electrochem. Soc. 153 (2006) A225–A232.

[9] E.C. Kumbur, K. V Sharp, M.M. Mench, Liquid droplet behavior and instability in a polymer electrolyte fuel cell flow channel, J. Power Sources. 161 (2006) 333–345.

[10] A. Theodorakakos, T. Ous, A. Gavaises, J.M. Nouri, N. Nikolopoulos, H. Yanagihara, Dynamics of water droplets detached from porous surfaces of relevance to PEM fuel cells, J. Colloid Interface Sci. 300 (2006) 673–687.

[11] R. Anderson, L. Zhang, Y. Ding, M. Blanco, X. Bi, D.P. Wilkinson, A critical review of two-phase flow in gas flow channels of proton exchange membrane fuel cells, J. Power Sources. 195 (2010) 4531–4553.

[12] A. Gunther, S.A. Khan, M. Thalmann, F. Trachsel, K.F. Jensen, Transport and reaction in microscale segmented gas-liquid flow, Lab Chip. 4 (2004) 278–286.

[13] S. Waelchli, P.R. von Rohr, Two-phase flow characteristics in gas-liquid microreactors, Int. J. Multiph. Flow. 32 (2006) 791–806.

[14] N. Kim, E.T. Evans, D.S. Park, S.A. Soper, M.C. Murphy, D.E. Nikitopoulos, Gas-liquid two-phase flows in rectangular polymer micro-channels, Exp. Fluids. 51 (2011) 373–393.

[15] I.S. Hussaini, C.-Y. Wang, Visualization and quantification of cathode channel flooding in PEM fuel cells, J. Power Sources. 187 (2009) 444–451.

[16] C.H. Hidrovo, F.-M. Wang, J.E. Steinbrenner, E.S. Lee, S.S. Vigneron, C.-H. Cheng, et al., Water Slug Detachment in Two-Phase Hydrophobic Microchannel Flows, in: Proc. 3rd Int. Conf. Microchannels Minichannels, ASME, 2005: pp. ICMM2005–75261.

[17] Z.J. Lu, C. Rath, G.S. Zhang, S.G. Kandlikar, Water management studies in PEM fuel cells, part IV: Effects of channel surface wettability, geometry and orientation on the two-phase flow in parallel gas channels, Int. J. Hydrogen Energy. 36 (2011) 9864–9875.

[18] Z. Lu, S.G. Kandlikar, C. Rath, M. Grimm, W. Domigan, A.D. White, et al., Water management studies in PEM fuel cells, Part II: Ex situ investigation of flow maldistribution, pressure drop and two-phase flow pattern in gas channels, Int. J. Hydrogen Energy. 34 (2009) 3445–3456.

[19] C.E. Colosqui, M.J. Cheah, I.G. Kevrekidis, J.B. Benziger, Droplet and slug formation in polymer electrolyte membrane fuel cell flow channels: The role of interfacial forces, J. Power Sources. 196 (2011) 10057–10068.

[20] G. Minor, N. Djilali, D. Sinton, P. Oshkai, Flow within a water droplet subjected to an air stream in a hydrophobic microchannel, Fluid Dyn. Res. 41 (2009).

[21] N. Yousfi-Steiner, P. Mocoteguy, D. Candusso, D. Hissel, A. Hernandez, A. Aslanides, A review on PEM voltage degradation associated with water management: Impacts, influent factors and characterization, J. Power Sources. 183 (2008) 260–274.

[22] P. Rodatz, F. Büchi, C. Onder, L. Guzzella, Operational aspects of a large PEFC stack under practical conditions, J. Power Sources. 128 (2004) 208–217.

[23] W. He, G. Lin, T. Van Nguyen, Diagnostic tool to detect electrode flooding in proton-exchange-membrane fuel cells, Aiche J. 49 (2003) 3221–3228.

[24] R.W. Lockhart, R.C. Martinelli, Proposed correlation of data for isothermal two-phase two-component flow in pipes, Chem. Eng. Prog. 45 (1949) 39–48.

[25] Y. Wang, S. Basu, C.Y. Wang, Modeling two-phase flow in PEM fuel cell channels, J. Power Sources. 179 (2008) 603–617.

[26] N. Akhtar, A. Qureshi, J. Scholta, C. Hartnig, M. Messerschmidt, W. Lehnert, Investigation of water droplet kinetics and optimization of channel geometry for PEM fuel cell cathodes, Int. J. Hydrogen Energy. 34 (2009) 3104–3111.

[27] J. Scholta, G. Escher, W. Zhang, L. Kuppers, L. Jorissen, W. Lehnert, Investigation on the influence of channel geometries on PEMFC performance, J. Power Sources. 155 (2006) 66–71.

[28] S. Shimpalee, J.W. Van Zee, Numerical studies on rib & channel dimension of flow-field on PEMFC performance, Int. J. Hydrogen Energy. 32 (2007) 842–856.

[29] X. Zhu, Q. Liao, P.C. Sui, N. Djilali, Numerical investigation of water droplet dynamics in a low-temperature fuel cell microchannel: Effect of channel geometry, J. Power Sources. 195 (2010) 801–812.

[30] T. Metz, N. Paust, C. Mfiller, R. Zengerle, P. Koltay, Passive water removal in fuel cells by capillary droplet actuation, Sensors and Actuators a-Physical. 143 (2008) 49–57.

[31] J.P. Owejan, T.A. Trabold, D.L. Jacobson, M. Arif, S.G. Kandlikar, Effects of flow field and diffusion layer properties on water accumulation in a PEM fuel cell, Int. J. Hydrogen Energy. 32 (2007) 4489–4502.

[32] M. Cheah, I.G. Kevrekidis, J.B. Benziger, Water slug formation and motion in gas flow channels: the effects of geometry, surface wettability, and gravity, Langmuir. 29 (2013) 9918–9934.

[33] N. Djilali, P.C. Sui, Transport phenomena in fuel cells: from microscale to macroscale, Int. J. Comut. Fluid Dyn. 22 (2008) 115–133.

[34] C. Fang, C. Hidrovo, F. Wang, J. Eaton, K. Goodson, 3-D numerical simulation of contact angle hysteresis for microscale two phase flow, Int. J. Multiph. Flow. 34 (2008) 690–705.

[35] K. Tüber, D. Pócza, C. Hebling, Visualization of water buildup in the cathode of a transparent PEM fuel cell, J. Power Sources. 124 (2003) 403–414.

[36] X. Zhu, P.C. Sui, N. Djilali, Three-dimensional numerical simulations of water droplet dynamics in a PEMFC gas channel, J. Power Sources. 181 (2008) 101–115.

[37] A.D. Le, B. Zhou, A general model of proton exchange membrane fuel cell, J. Power Sources. 182 (2008) 197–222.

[38] Y. Tabe, Y. Lee, T. Chikahisa, M. Kozakai, Numerical simulation of liquid water and gas flow in a channel and a simplified gas diffusion layer model of polymer electrolyte membrane fuel cells using the lattice Boltzmann method, J. Power Sources. 193 (2009) 24–31.

[39] Y. Ding, H.T. Bi, D.P. Wilkinson, Three-dimensional numerical simulation of water droplet emerging from a gas diffusion layer surface in micro-channels, J. Power Sources. 195 (2010) 7278–7288.

[40] S.G. Mukherjee, A; Kandlikar, A Numerical Analysis of Growing Water Droplet inside an Air Supply Channel of a PEM Fuel Cell, in: 2006.

[41] J. Choi, G. Son, Numerical study of droplet dynamics in a PEMFC gas channel with multiple pores, J. Mech. Sci. Technol. 23 (2009) 1765–1772.

[42] T.D. Blake, The physics of moving wetting lines., J. Colloid Interface Sci. 299 (2006) 1–13.

[43] S. Sikalo, H.-D.D. Wilhelm, I. V. Roisman, S. Jakirlic, C. Tropea, S. Šikalo, et al., Dynamic contact angle of spreading droplets: Experiments and simulations, Phys. Fluids. 17 (2005) 062103.

[44] F.Y. Zhang, X.G. Yang, C.Y. Wang, Liquid Water Removal from a Polymer Electrolyte Fuel Cell, J. Electrochem. Soc. 153 (2006) A225.

[45] C.H. Schillberg, S.G. Kandlikar, A Review of Models for Water Droplet Detachment From the Gas Diffusion Layer-Gas Flow Channel Interface in PEMFCs, ASME Conf. Proc. 2007 (2007) 299–310.

[46] E.B. Dussan V., R.T.-P. Chow, On the ability of drops or bubbles to stick to non-horizontal surfaces of solids, J. Fluid Mech. 137 (1983) 1–29.

[47] E.B. Dussan V., On the ability of drops or bubbles to stick to non-horizontal surfaces of solids. Part 2. Small drops or bubbles having contact angles of arbitrary size, J. Fluid Mech. 151 (1985) 1–20.

[48] E.B. Dussan V., On the ability of drops to stick to surfaces of solids. Part 3. The influences of the motion of the surrounding fluid on dislodging drops, J. Fluid Mech. 174 (1987) 381–397.

[49] P. Dimitrakopoulos, J.J.L. Higdon, Displacement of fluid droplets from solid surfaces in low-Reynolds-number shear flows, J. Fluid Mech. 377 (1997) 351–378.

[50] P. Dimitrakopoulos, J.J.L. Higdon, On the displacement of three-dimensional fluid droplets from solid surfaces in low-Reynolds-number shear flows, J. Fluid Mech. 377 (1998) 189–222.

[51] C. Miller, Liquid Water Dynamics in a Model Polymer Electrolyte Fuel Cell Flow Channel, Dept. Mech. Eng. MASc (2010).

[52] C.W. Hirt, B.D. Nichols, Volume of fluid (VOF) method for the dynamics of free boundaries, J. Comput. Phys. 39 (1981) 201–225.

[53] P. Quan, B. Zhou, A. Sobiesiak, Z.S. Liu, Water behavior in serpentine micro-channel for proton exchange membrane fuel cell cathode, J. Power Sources. 152 (2005) 131–145.

[54] Y.H. Cai, J. Hu, H.P. Ma, B.L. Yi, H.M. Zhang, Effects of hydrophilic/hydrophobic properties on the water behavior in the micro-channels of a proton exchange membrane fuel cell, J. Power Sources. 161 (2006) 843–848.

[55] X. Zhu, P.C. Sui, N. Djilali, Dynamic behaviour of liquid water emerging from a GDL pore into a PEMFC gas flow channel, J. Power Sources. 172 (2007) 287–295.

[56] X. Zhu, P.C. Sui, N. Djilali, Numerical simulation of emergence of a water droplet from a pore into a microchannel gas stream, Microfluid. Nanofluidics. 4 (2008) 543–555.

[57] K.S. Chen, Modeling Water-Droplet Detachment From GDL/Channel Interface in PEM Fuel Cells, ASME Conf. Proc. 2008 (2008) 797–803.

[58] Y. Ding, H.T. Bi, D.P. Wilkinson, Three dimensional numerical simulation of gas-liquid two-phase flow patterns in a polymer-electrolyte membrane fuel cells gas flow channel, J. Power Sources. 196 (2011) 6284–6292.

[59] B. Sundén, Transport phenomena in fuel cells, WIT Press, Boston, 2005.

[60] J.A. Sethian, Level set methods and fast marching methods : evolving interfaces in computational geometry, fluid mechanics, computer vision, and materials sciences, Cambridge Univ. Press, Cambridge [u.a.], 2006.

[61] M. Sussman, P. Smereka, S. Osher, A Level Set Approach for Computing Solutions to Incompressible Two-Phase Flow, J. Comput. Phys. 114 (1994) 146–159.

[62] M. Sussman, A.S. Almgren, J.B. Bell, P. Colella, L.H. Howell, M.L. Welcome, An Adaptive Level Set Approach for Incompressible Two-Phase Flows, J. Comput. Phys. 148 (1999) 81–124.

[63] S. Chen, G.D. Doolen, Lattice Boltzmann method for fluid flows, Annu. Rev. Fluid Mech. 30 (1998) 329–364.

[64] X.W. Shan, H.D. Chen, Lattice Boltzmann model for simulating flows with multiple phases and components, Phys. Rev. E. 47 (1993) 1815–1819.

[65] K. Fei, C.W. Hong, All-angle removal of CO2 bubbles from the anode microchannels of a micro fuel cell by lattice-Boltzmann simulation, Microfluid. Nanofluidics. 3 (2007) 77–88.

[66] J. Park, X. Li, Multi-phase micro-scale flow simulation in the electrodes of a PEM fuel cell by lattice Boltzmann method, J. Power Sources. 178 (2008) 248–257.

[67] L. Hao, P. Cheng, Lattice Boltzmann simulations of liquid droplet dynamic behavior on a hydrophobic surface of a gas flow channel, J. Power Sources. 190 (2009) 435–446.

[68] A.K. Gunstensen, D.H. Rothman, S. Zaleski, G. Zanetti, Lattice Boltzmann model of immiscible fluids, Phys. Rev. A. 43 (1991) 4320–4327.

[69] M.R. Swift, E. Orlandini, W.R. Osborn, J.M. Yeomans, Lattice Boltzmann simulations of liquid-gas and binary fluid systems, Phys. Rev. E. 54 (1996) 5041–5052.

[70] X. He, G.D. Doolen, Thermodynamic Foundations of Kinetic Theory and Lattice Boltzmann Models for Multiphase Flows, J. Stat. Phys. 107 (2002) 309–328.

[71] Y.Y. Yan, Y.Q. Zu, A lattice Boltzmann method for incompressible two-phase flows on partial wetting surface with large density ratio, J. Comput. Phys. 227 (2007) 763–775.

[72] T. Inamuro, T. Ogata, S. Tajima, N. Konishi, A lattice Boltzmann method for incompressible two-phase flows with large density differences, J. Comput. Phys. 198 (2004) 628–644.

[73] A.J. Briant, A.J. Wagner, J.M. Yeomans, Lattice Boltzmann simulations of contact line motion. I. Liquid-gas systems, Phys. Rev. E. 69 (2004) 31602.

[74] X.D. Niu, T. Munekata, S.A. Hyodo, K. Suga, An investigation of water-gas transport processes in the gas-diffusion-layer of a PEM fuel cell by a multiphase multiple-relaxation-time lattice Boltzmann model, J. Power Sources. 172 (2007) 542–552.

[75] I. V Roisman, L. Opfer, C. Tropea, M. Raessi, J. Mostaghimi, S. Chandra, Drop impact onto a dry surface: Role of the dynamic contact angle, Colloids Surfaces A Physicochem. Eng. Asp. 322 (2008) 183–191.

[76] Y.D. Shikhmurzaev, The moving contact line on a smooth solid surface, Int. J. Multiph. Flow. 19 (1993) 589–610.

[77] T.D. Blake, Y.D. Shikhmurzaev, Dynamic wetting by liquids of different viscosity, J. Colloid Interface Sci. 253 (2002) 196–202.

[78] C. Huh, S.G. Mason, The steady movement of a liquid meniscus in a capillary tube, J. Fluid Mech. Digit. Arch. 81 (1977) 401–419.

[79] P.A. Durbin, Considerations on the moving contact-line singularity, with application to frictional drag on a slender drop, J. Fluid Mech. Digit. Arch. 197 (1988) 157–169.

[80] C. Baiocci, V. V Pukhnachev, Problems with one-sided constraints for Navier-Stokes equations and the dynamic contact angle, J. Appl. Mech. Tech. Phys. 31 (1990) 185–197.

[81] S. Šikalo, H.-D.D. Wilhelm, I. V. Roisman, S. Jakirlić, C. Tropea, S. Sikalo, et al., Dynamic contact angle of spreading droplets: Experiments and simulations, Phys. Fluids. 17 (2005) 062103.

[82] R.G. Cox, Inertial and viscous effects on dynamic contact angles, J. Fluid Mech. 357 (1998) 249–278.

[83] S. Mukherjee, J. Abraham, Investigations of drop impact on dry walls with a lattice-Boltzmann model, J. Colloid Interface Sci. 312 (2007) 341–354.

[84] M. Sussman, M. Ohta, A stable and efficient method for treating surface tension in incompressible two-phase flow, Siam J. Sci. Comput. 31 (2009) 2447–2471.

[85] T.C. Wu, N. Djilali, Qualitative and quantitative analysis of moving droplets in a modelled PEMFC cathode gas microchannel, in: 20th Int. Symp. Transp. Phenom., Victoria, BC, Canada, 2009.

[86] E. Kimball, T. Whitaker, Y.G. Kevrekidis, J.B. Benziger, Drops , Slugs , and Flooding in Polymer Electrolyte Membrane Fuel Cells, Aiche J. 54 (2008) 1313–1332.

[87] A. Bazylak, D. Sinton, N. Djilali, Dynamic water transport and droplet emergence in PEMFC gas diffusion layers, J. Power Sources. 176 (2008) 240–246.

[88] N.T. Nguyen, S.H. Chan, Micromachined polymer electrolyte membrane and direct methanol fuel cells - a review, J. Micromechanics Microengineering. 16 (2006) R1–R12.

[89] S. Litster, D. Sinton, N. Djilali, Ex situ visualization of liquid water transport in PEM fuel cell gas diffusion layers, J. Power Sources. 154 (2006) 95–105.

[90] M.K. Akbar, D.A. Plummer, S.M. Ghiaasiaan, On gas-liquid two-phase flow regimes in microchannels, Int. J. Multiph. Flow. 29 (2003) 855–865.

[91] ANSYS FLUENT V14.0 Theory Guide, 15317 (2011).

[92] J.U. Brackbill, D.B. Kothe, C. Zemach, A continuum method for modeling surface tension, J. Comput. Phys. 100 (1992) 335–354.

[93] D.L. Youngs, Time-dependent multi-material flow with large fluid distortion, Numer. Methods Fluid Dyn. 24 (1982) 273–285.

[94] CFD-ACE+ v2010.0 Modules Manual, Part 2, (2010).

[95] B. He, N.A. Patankar, J. Lee, Multiple equilibrium droplet shapes and design criterion for rough hydrophobic surfaces, Langmuir. 19 (2003) 4999–5003.

[96] S. Sikalo, E.N. Ganic, Phenomena of droplet-surface interactions, Exp. Therm. Fluid Sci. 31 (2006) 97–110.

[97] V. Mehdi-Nejad, J. Mostaghimi, S. Chandra, Air bubble entrapment under an impacting droplet, Phys. Fluids. 15 (2003) 173.

[98] S.T. Thoroddsen, T.G. Etoh, K. Takehara, N. Ootsuka, Y. Hatsuki, The air bubble entrapped under a drop impacting on a solid surface, J. Fluid Mech. 545 (2005) 203.

[99] S. Sikalo, M. Marengo, C. Tropea, E.N. Ganic, Analysis of impact of droplets on horizontal surfaces, Exp. Therm. 25 (2002) 503–510.

[100] A. Mata, A.J. Fleischman, S. Roy, Fabrication of multi-layer SU-8 microstructures, J. Micromechanics Microengineering. 16 (2006) 276–284.

[101] Y.N. Xia, G.M. Whitesides, Soft lithography, Annu. Rev. Mater. Sci. 28 (1998) 153–184.

8 Appendix A – Microfluidic chip fabrication

Chips incorporating the microchannels were fabricated on a 3″ silicon wafer by a sequential multi-layer SU-8 (MicroChem Corp.) fabrication process [100]. Two different high resolution laser photo-plotted masks were prepared for the water and air delivery networks. A 25 µm layer of SU-8 25 was first spin coated, baked, exposed and developed to form the water delivery path. This process was repeated for a second 125 µm SU-8 100 layer to form the air delivery path. The finished multi-layer SU-8 structure served as the molding master for soft lithography techniques [101]. Two different mixture ratios of PDMS, 15:1 (with excess vinyl groups) and 5:1 (with excess Si-H groups), were cast separately on the multi-layer molding master and thermally cured on a hotplate at 80 ℃ for 40 minutes. The cured PDMS polymer was peeled off from the master mold, punched for fluidic access for water and air, diced, ethanol cleaned and finally air dried. The molding master was treated with a few drops of Repel-Silane ES (General Electric PlusOne) liquid for 5 minutes before each use for casting to prevent adhesion of the PDMS on the SU-8. Two symmetric elastomers with different mixture ratios of PDMS were carefully aligned to each other by predefined alignment marks under a stereo microscope providing ±5 µm precision. The aligned chip was thermal bonded on a hotplate at 80 ℃ for 2 hours or overnight to increase the strong interfacial bonding between the two pieces. The secure bonding between the two pieces is important to prevent any leakage in the air stream at pressures up to 3 atmospheres. After bonding, a complete chip consists of a 50 µm square water pore and a 250 µm square air channel as shown in Figure 3.1a.

9 Appendix B – MATLAB source code

Correlation coefficient and droplet frequency

E:\Miro4\cavideo.m

```
%% Prepare video for contact angle measurements in SCA20 software
clc, clear;
% Read AVI file and show file information
[FileNameIn,PathNameIn] = uigetfile('*.avi','Select the AVI file');
obj = mmreader(FileNameIn);
disp(['Video Filename: ',obj.Name]);
disp(['Number of Frames: ',num2str(obj.NumberOfFrames)]);
disp(['Width of Frame: ',num2str(obj.Width)]);
disp(['Height of Frame: ',num2str(obj.Height)]);

%% View frames

for I = 404:821  %Change to suitable frame
    ImgI = read(obj,I);
    J = ImgI(10:61,5:115);
    J1 = imresize(J,4.0);
    figure(1), imshow(J1), title(['Image: #',num2str(I)]);
end

%% Output video file for contact angle measurement

CaStart = 404;
CaEnd = 821;           %Selecting amount of frames to output
fig = figure;
[FileNameOut,PathNameOut] = uiputfile('*.avi','Save new AVI file as...');
aviobj = avifile(FileNameOut,'compression','none');

for n = CaStart:CaEnd
    CaFrame = read(obj,n);
    Ca = CaFrame(10:61,5:115);
    K = imresize(Ca,4.0);         %Scale up 4x large for SCA20 software
    imshow(K);
    F = getframe(fig);
    aviobj = addframe(aviobj,F);
end

close(fig)
aviobj = close(aviobj);
```

```
%% Calculate 2D correlation coefficient from images piles.
% Te-Chun Wu, University of Victoria
% Jan 10, 2010.
clc, clear;

%% Timer start for program code
%tic;

%% AVI file information
[FileNameIn,PathNameIn] = uigetfile('*.avi','Select the AVI file');

info = aviinfo(FileNameIn);
disp(['AVI Filename: ',info.Filename]);
disp(['Number of Frames: ',num2str(info.NumFrames)]);
disp(['Width of Frame: ',num2str(info.Width)]);
disp(['Height of Frame: ',num2str(info.Height)]);

%% Set register image A
ImgA = 4800;                          %Change to suitable frame
RegImgA = aviread(FileNameIn,ImgA);
A = RegImgA.cdata(9:61,1:50);        %Field of interest
figure(1), subplot(2,2,1), imshow(A), title(['Image A: #',num2str(ImgA)]);

%% 2D Correlation Coefficient
startimg = 4800;                       %Set starting image for process
endimg = 15000;                       %Set ending image for process
nImg = endimg - startimg + 1;       %Number of images for process

y = zeros(nImg,1);

for n = startimg:endimg             %Image B that to be compared with A
    RegImgB = aviread(FileNameIn,n);
    B = RegImgB.cdata(9:61,1:50); % Field of interest, set to the same as image A

    %figure(1), subplot(2,2,3), imshow(B), title(['Image B: #',num2str(n)]);

    y(n) = corr2(A,B);
    if (y(n) < 0.5)                 %Filter to remove noise
        y(n) = 0.1;
    end

end

figure(1), subplot(2,2,[2 4]), plot(y(1:n));
title('Droplets emergence signal')
xlabel('Frame No.')
ylabel('corr2')

%% Pre-processing the time vector
F = 6006;                       %Camera frame rate, check carefully
T = 1/F;                        %Interval time
L = nImg;                       %Number of processed frames
t = (0:L-1)*T;                  %Time vector

figure(2), subplot(2,1,1), plot(t,y(startimg:endimg));
title('Droplets emergence signal')
xlabel('time (microseconds)')
ylabel('corr2')

%% FFT Algorithm
```

```
nfft = 2^(nextpow2(length(y)));   % Find next power of 2
ffty = fft(y,nfft);

NumUniquePts = ceil((nfft+1)/2);
ffty = ffty(1:NumUniquePts);
mx = abs(ffty);

mx = mx/length(y);
mx = mx.^2;
if rem(nfft,2)                    % Odd nfft excludes Nyquist
  mx(2:end) = mx(2:end)*2;
else
  mx(2:end -1) = mx(2:end -1)*2;
end

f = (0:NumUniquePts-1)*F/nfft;

figure(2), subplot(2,1,2), plot(f(1:100),mx(1:100));
title('Single sided amplitude spectrum of signal')
xlabel('Frequency (Hz)');
ylabel('Power');

%% Timer stop for program code
%toc;
```

10 Appendix C – FLUENT UDF source code for DCA

```
#include "udf.h"
#include "sg_mphase.h"
#include "sg_vof.h"
#include "sg.h"
#include "mem.h"

#define VISCOSITY 0.001
#define SURF_TENS 0.0728
#define MYTRUE 1
#define MYFALSE 0
#define Hoff(x) acos(1-(2.0*tanh(5.16*(pow((x/(1+(1.31*pow(x,0.99)))),0.706)))))
#define static_Con_Ang 110.
#define index_source 3

/* This Code computes the normals of the VOF function using in FLUENT UDF */

DEFINE_ADJUST(store_gradient, domain)
{
   Thread *t;
   Thread **pt;
   cell_t c;
   int phase_domain_index = 1;     /* Secondary Domain */
   Domain *pDomain = DOMAIN_SUB_DOMAIN(domain,phase_domain_index);
   void calc_source();

   Alloc_Storage_Vars(pDomain,SV_VOF_RG,SV_VOF_G,SV_NULL);
   Scalar_Reconstruction(pDomain,SV_VOF,-1,SV_VOF_RG,NULL);
   Scalar_Derivatives(pDomain,SV_VOF,-1,SV_VOF_G,SV_VOF_RG,Vof_Deriv_Accumulate);

   mp_thread_loop_c (t,domain,pt)
   if (FLUID_THREAD_P(t))
   {
     Thread *ppt = pt[phase_domain_index];

     begin_c_loop (c,t)
     {
       calc_source(c,t);
     }
     end_c_loop (c,t)
   }

   Free_Storage_Vars(pDomain,SV_VOF_RG,SV_VOF_G,SV_NULL);
}

void calc_source(cell_t cell, Thread *thread)
{
   real VOF_Val[3], VOF_Mag, source, VOF_Norm[3];
   Thread *phaset;
   phaset= THREAD_SUB_THREAD(thread,1);

   if (C_VOF(cell,phaset)!=0.0 && N_TIME > 1)
   {
```

```
53        /* The gradients of the VOF function are found in the x,y and z dir. */
54       if (NULLP(THREAD_STORAGE(phaset, SV_VOF_G)))
55       {
56         Message0("N_TIME = %d, ....show-grad:Gradient of VOF is not available \n ",
           N_TIME);
57         Error("0");
58       }
59         VOF_Val[0]=-C_VOF_G(cell,phaset)[0];
60         VOF_Val[1]=-C_VOF_G(cell,phaset)[1];
61         VOF_Val[2]=-C_VOF_G(cell,phaset)[2];
62
63         /* The magnitude of the VOF gradients is found so it can be normalized */
64         VOF_Mag=NV_MAG(VOF_Val);
65         if(VOF_Mag!=0.0)
66         {
67            VOF_Mag=NV_MAG(VOF_Val);
68            VOF_Norm[0]=VOF_Val[0]/VOF_Mag;
69            VOF_Norm[1]=VOF_Val[1]/VOF_Mag;
70            VOF_Norm[2]=VOF_Val[2]/VOF_Mag;
71         }
72         else
73         {
74            /* This is to avoid the divide by zero function*/
75            VOF_Norm[0]=0.0;
76            VOF_Norm[1]=0.0;
77            VOF_Norm[2]=0.0;
78         }
79
80         C_UDMI(cell,thread,0)=VOF_Norm[0];
81         C_UDMI(cell,thread,1)=VOF_Norm[1];
82         C_UDMI(cell,thread,2)=VOF_Norm[2];
83     }
84     source = 0.0;
85     C_UDMI(cell, thread, index_source) = source;
86  }
87
88  DEFINE_SOURCE(VOF_Norms, cell, thread, dS, eqn)
89  {
90    real source;
91    source = C_UDMI(cell, thread, index_source);
92    return source;
93  }
94
95  /* This Define_profile code is designed to provide a dynamic contact angle for the
    VOF function */
96  DEFINE_PROFILE(con_ang, t, pos)
97  {
98       /* First the various pointer variables are created */
99       face_t f;
100      cell_t c;
101      real feta_d,vel_Val[3],cont_Line_Vel,VOF_Normal[3],cap_Num,static_Con_Rad,
         x_Bottom,x_Top, x_Bisect,hoff_Old,hoff_Cur,hoff_New,finish_Cond,inv_Hoff=0.0;
```

```
102       int notConverged,itNum;
103       Thread *t0,*pt;
104
105   /* This code is designed to find the zero for the inverted Hoffman function by
      finding the zero */
106   /* of the function at which the Hoffman function results in the static contact
      angle */
107
108       /* First the variables are assigned */
109       notConverged=MYTRUE;
110       x_Bottom=0.001;
111       x_Top=2.0;
112       itNum=0;
113       static_Con_Rad=((static_Con_Ang*M_PI)/180.);
114
115       /* A while loop performs the bisection method, a simple but very stable zero
          finder */
116       while(notConverged)
117       {
118         /* The variables used in the bisection method are assigned and the Hoffman */
119         /* functions are evaluated */
120         itNum++;
121         hoff_Old=(Hoff(x_Bottom)- static_Con_Rad);
122         hoff_Cur=(Hoff(x_Top)- static_Con_Rad);
123         x_Bisect=(x_Bottom+x_Top)/2.0;
124         hoff_New=(Hoff(x_Bisect)- static_Con_Rad);
125         finish_Cond=fabs(1-(x_Bisect/x_Top));
126
127         /* The loop ends when the relative error is less than 1e-8 and the inverse */
128         /* Hoffman value is stored for use later */
129         if(finish_Cond<0.00000001 || itNum>10000000)
130         {
131           inv_Hoff=x_Bisect;
132           notConverged=MYFALSE;
133         }
134
135         /* Conditions for the bisection method */
136         if((hoff_Old*hoff_New)<0.0)
137         {
138           x_Top=x_Bisect;
139         }
140
141         if((hoff_Cur*hoff_New)<=0.0)
142         {
143           x_Bottom=x_Bisect;
144         }
145
146       }
147
148   /* Now the main loop goes through all the faces in the boundary */
149       begin_f_loop(f,t)
150       {
```

```
151           /* The cell and phase threads are isolated */
152         c=F_C0(f,t);
153         t0=THREAD_T0(t);
154         pt= THREAD_SUB_THREAD(t0,1);
155
156         /* The main formulation is only applied if the VOF is >0 */
157         if(C_VOF(c,pt)!=0.0)
158         {
159            /* The velocities are recorded in each direction */
160            vel_Val[0]=C_U(c,t0);
161            vel_Val[1]=C_V(c,t0);
162            vel_Val[2]=C_W(c,t0);
163
164            /* The VOF normals are brought in */
165            VOF_Normal[0]=C_UDMI(c,t0,0);
166            VOF_Normal[1]=C_UDMI(c,t0,1);
167            VOF_Normal[2]=C_UDMI(c,t0,2);
168
169            /* The contact line vel. is calc from the dot product of VOF and Vel */
170            cont_Line_Vel=NV_DOT(vel_Val,VOF_Normal);
171
172            /* The capillary number is found based on cont line vel. */
173            cap_Num=fabs((VISCOSITY*cont_Line_Vel)/SURF_TENS);
174
175            /* The dynamic contact angle is defined then stored in the profile */
176            if(cap_Num+inv_Hoff<0.0)
177            {
178              cap_Num=inv_Hoff;
179            }
180
181            feta_d=((Hoff(cap_Num+inv_Hoff))*180)/M_PI;
182            F_PROFILE(f,t,pos)=feta_d;
183         }
184
185         else
186         {
187           F_PROFILE(f,t,pos)=static_Con_Ang;
188         }
189       }
190
191       end_f_loop(f,t)
192
193   }
194
```

11 Appendix D – FLUENT UDF source code for droplet impact

```
/* Droplet initialization code for normal impacting on horizontal surface */
#include "udf.h"
DEFINE_INIT(Drop_Init,mixture_domain)  /* This DEFINE_INIT code makes a droplet at the origin */
{
 #if !RP_HOST
  /* First the various pointer variables are created */
  int phase_domain_index;
  cell_t cell;
  Thread *t;
  Domain *subdomain;
  real position[ND_ND], distance, dropCen[3], dropRad;
  /* The cells are all looped through */
  dropRad=0.00135;  /* droplet diameter is 2.7 mm, however only half axisymmetric domain was simulated  */
  dropCen[0]=-1.0*dropRad;
  dropCen[1]=0.0;
  sub_domain_loop(subdomain, mixture_domain, phase_domain_index)
  {
   if (DOMAIN_ID(subdomain) == 3)
     thread_loop_c(t,subdomain)
     {
        begin_c_loop_all(cell,t)
        {
         C_CENTROID(position,cell,t);
         distance=sqrt((pow(position[0]-dropCen[0],2.0)+pow(position[1]- dropCen[1],2.0)));
         /* distance from any point to the droplet center */
         if(distance <= dropRad) /* This means the cell is inside the droplet */
         {
           C_VOF(cell,t)=1.0;
           C_U(cell,t)=1.566815184; /* impact velocity, derived from Webber number */
         }
         else
           C_VOF(cell,t)=0.0;
        }
        end_c_loop_all(cell,t)
     }
  }
 #endif
}
```

12 Appendix E – Pressure drop measurement data

Table 12.1. Pressure drop measurement of Plastic-0A using dual water injection.

Plastic-0A dual injection, ΔP_{0128}							
Case	Qw	Qa	Re_A	Dry (ΔP_g)	Wet ($\Delta P_{2\phi}$)	Wet-Dry ($\Delta P_{2\phi} - \Delta P_g$)	Wet/Dry ($\phi_g{}^2$)
#11	0.075	407	891	9,686	10,491	805	1.083
#12		306	670	7,253	7,947	694	1.096
#13		204	447	4,818	5,308	490	1.102
#14		61	134	1,447	1,714	267	1.185
#21	0.056	407	891	9,707	10,262	555	1.057
#22		306	670	7,268	7,809	541	1.074
#23		204	447	4,818	5,201	383	1.079
#24		61	134	1,443	1,702	259	1.179
#31	0.037	407	891	9,715	10,116	401	1.041
#32		306	670	7,272	7,636	364	1.050
#33		204	447	4,827	5,134	307	1.064
#34		61	134	1,439	1,641	202	1.140
#41	0.011	407	891	9,790	10,084	294	1.030
#42		306	670	7,281	7,419	138	1.019
#43		204	447	4,824	4,987	163	1.034
#44		61	134	1,416	1,826	410	1.290

Table 12.2. Pressure drop measurement of Plastic-02 using single water injection.

Plastic-02 single injection, ΔP_{0128}							
Case	**Qw**	**Qa**	**Re_A**	**Dry (ΔP_g)**	**Wet ($\Delta P_{2\phi}$)**	**Wet-Dry ($\Delta P_{2\phi} - \Delta P_g$)**	**Wet/Dry ($\phi_g{}^2$)**
#11	0.075	407	953	23,517	25,091	1,574	1.067
#12		306	716	17,902	20,534	2,632	1.096
#13		204	478	11,999	14,265	2,266	1.102
#14		61	143	3,550	6,140	2,590	1.185
#21	0.056	407	953	23,450	25,514	2,064	1.057
#22		306	716	17,866	19,817	1,951	1.074
#23		204	478	11,904	13,621	1,717	1.079
#24		61	143	3,562	5,202	1,640	1.179
#31	0.037	407	953	23,513	24,894	1,381	1.041
#32		306	716	17,807	18,968	1,161	1.050
#33		204	478	11,971	13,326	1,355	1.064
#34		61	143	3,602	4,704	1,102	1.140
#41	0.011	407	953	23,687	24,235	548	1.030
#42		306	716	17,995	18,601	606	1.019
#43		204	478	12,053	12,466	413	1.034
#44		61	143	3,590	4,214	624	1.290

Table 12.3 Pressure drop measurement of CFP-010A using single water injection.

CFP-010A single injection, ΔP_{0128}							
Case	**Qw**	**Qa**	**Re_A**	**Dry (ΔP_g)**	**Wet ($\Delta P_{2\phi}$)**	**Wet-Dry ($\Delta P_{2\phi} - \Delta P_g$)**	**Wet/Dry ($\phi_g{}^2$)**
#11	0.075	407	617	2,986	3,380	394	1.132
#12		306	464	2,246	2,493	247	1.110
#13		204	309	1,485	1,698	213	1.144
#14		61	92	447	568	121	1.271
#21	0.056	407	617	2,995	3,231	236	1.079
#22		306	464	2,259	2,475	216	1.096
#23		204	309	1,463	1,640	177	1.121
#24		61	92	444	598	154	1.348
#31	0.037	407	617	2,968	3,152	184	1.062
#32		306	464	2,219	2,375	156	1.070
#33		204	309	1,470	1,603	133	1.091
#34		61	92	444	526	82	1.185
#41	0.011	407	617	2,971	3,068	97	1.033
#42		306	464	2,223	2,296	72	1.033
#43		204	309	1,473	1,542	68	1.046
#44		61	92	448	483	35	1.078

Table 12.4 Pressure drop measurement of CFP-0D using single water injection.

CFP-0D single injection, ΔP_{0128}							
Case	**Qw**	**Qa**	**Re_A**	**Dry (ΔP_g)**	**Wet ($\Delta P_{2\phi}$)**	**Wet-Dry ($\Delta P_{2\phi} - \Delta P_g$)**	**Wet/Dry ($\phi_g{}^2$)**
#11	0.075	407	684	6,543	6,850	307	1.047
#12		306	514	4,911	5,192	281	1.057
#13		204	343	3,266	3,507	241	1.074
#14		61	103	981	1,186	205	1.209
#21	0.056	407	684	6,586	6,862	276	1.042
#22		306	514	4,939	5,174	235	1.048
#23		204	343	3,275	3,481	206	1.063
#24		61	103	981	1,139	158	1.161
#31	0.037	407	684	6,527	6,756	229	1.035
#32		306	514	4,891	5,092	201	1.041
#33		204	343	3,261	3,428	167	1.051
#34		61	103	981	1,106	125	1.128
#41	0.011	407	684	6,528	6,672	145	1.022
#42		306	514	4,884	5,010	126	1.026
#43		204	343	3,250	3,361	112	1.034
#44		61	103	976	1,072	96	1.098